



Virginia Commonwealth University
VCU Scholars Compass

Theses and Dissertations

Graduate School

2022

Analysis of Microdroplets and Microorganisms by Single Entity Electrochemistry

Junaid U. Ahmed

Follow this and additional works at: <https://scholarscompass.vcu.edu/etd>

 Part of the [Analytical Chemistry Commons](#)

© The Author

Downloaded from

<https://scholarscompass.vcu.edu/etd/6965>

This Dissertation is brought to you for free and open access by the Graduate School at VCU Scholars Compass. It has been accepted for inclusion in Theses and Dissertations by an authorized administrator of VCU Scholars Compass. For more information, please contact libcompass@vcu.edu.

Virginia Commonwealth University

Doctoral Dissertation

Analysis of Microdroplets and Microorganisms

by Single Entity Electrochemistry

Author: *Junaid U. Ahmed*

Advisor: *Julio C. Alvarez*

A dissertation submitted in fulfillment of the requirements

for the degree of

Doctor of Philosophy

in the chemistry department

April 25, 2022



Dedicated to
My lovely mother

Analysis of Microdroplets and Microorganisms by Single Entity Electrochemistry

Junaid U. Ahmed

Virginia Commonwealth University, Richmond, VA

2022

Abstract

Single Entity Electrochemistry (SEE) is an emerging electrochemical technique that has been used to characterize discrete entities by measuring the change in current or potential during individual stochastic events (collision or adsorption) of an entity with an ultramicroelectrode (UME) of similar dimensions. The shape and magnitude of the SEE signal depend on the underlying mechanism of interaction with the UME surface. There is a critical need for quantitative models that correlate the SEE signal with properties of the entity-UME system, including effects of acquisition instrumentation, to prevent misinterpretation of data.

This research focused on integrated experiments and simulations to quantify the effects of the interaction dynamics (collision and adsorption) of the microparticle and UME to deduce the properties of liquid droplets (diameter, contact radius, droplet redox mechanism) and bacteria (size, landing orientation, arrival pace). Chapter 1 introduces the SEE technique and the signals that appeared in the current vs. time graphs relevant to this dissertation. Chapter 2 compares the signal efficiency of adsorption versus bouncing collisions of emulsified ferrocene-trapped toluene droplets ($\sim 1 \mu\text{m}$) with a disk UME of $\sim 5 \mu\text{m}$ in diameter. The average droplet diameter ($\sim 0.7 \mu\text{m}$) determined from peak area integration was close to Dynamic Light Scattering measurements ($\sim 1 \mu\text{m}$), suggesting droplet adsorption on the UME. Simulation results indicated that about ~ 5 million short-lived collisions ($0.11 \mu\text{s}$) from a single droplet occurring over ~ 1.25 hours produce the same

signal as a single droplet being adsorbed for ~ 0.6 s. These results point to a heightened sensitivity and speed when relying on adsorption instead of collisions. Chapter 3 describes the size determination and adsorption orientation for three bacilli of variable length (~ 1 , ~ 2 and ~ 5 μm). In this study, the stochastic blocking approach was utilized, whereby ferrocyanide is oxidized to ferricyanide at the UME, and the bacillus blocks the flux of ferrocyanide and its reaction in proportion to the bacillus' size. The bacilli's size and orientation was inferred from COMSOL simulations of the current change during blocking events. We also found that the bacilli approach to the UME causes increasing perturbations of redox flux until it reaches its maximum value on the UME surface, encoding the signature of traveled distance in the current change. It pointed to a threshold distance from the electrode area, which depends on the bacilli size and can be used to estimate the bacilli arrival pace by correlating the current step time. This study illustrates the utility of SEE to determine cytometric properties of live microorganisms, which could be a source of analytical selectivity for detecting pathogens based on size, landing orientation, and approach speed.

Acknowledgements

First, I want to thank my research advisor Julio C. Alvarez, for his care and relentless support during my Ph.D. journey. He has been an incredible mentor who inspired me to expand my thought process and connect the dots for broader application of the research outcomes. He recognized my passion for chemistry and showed me how to focus that passion towards research goals. I am grateful for his guidance in strengthening my writing and presentation skills, which were lacking at the start of my Ph.D. journey as an international student. He also encouraged me to focus on collaboration and networking, and providing research training to the young, such as high school students and chemistry undergraduates. My time in his research group will always be memorable to me. I hope to continue working with him beyond my graduate career.

I am also grateful to my committee members: Dr. Maryanne Collinson, Dr. Vladimir Sidorov, and Dr. Dexian Ye. Their advice, friendship, and scientific knowledge pushed me to think creatively and deeply about science. I am thankful to Dr. Hani El-Kaderi, Dr. Katharine Tibbetts, Dr. Indika U. Arachchige, and Dr. Maryanne Collinson for allowing me to perform collaborative research in pursuit of interdisciplinary innovations.

My best friend at VCU, John A. Lutkenhaus, and I had a lot of fun performing research together. His friendship, care, and encouragement helped me grow as a scientist. Moreover, he always assisted me in adopting American culture, and ensured I never felt alone in the VCU community. I am sure we shall do more outstanding research together in the future. I am also thankful to Ashley Tubbs, who encouraged me to step outside of the research domain and into the networking frontier, such as the Virginia and Eastern US Younger Chemists Committee sections. I want to name my friend Abdullah Al Macktuf, with whom I frequently discussed my research. His feedback and insights from a different setback helped me grow in this field. I am grateful to my friends Jayani

Christopher and Ashish Nag for supporting me with the bacteria cell cultures and recording the SEM images of the bacteria needed for my research. I also appreciate Sabbir Alam and Ivan Marshall for teaching me MATLAB simulations. I am also thankful to Abdullah Al Macktuf, Asis Nag, Shafiul Islam, Rajib Sarkar, and Ahmed Alzharani for allowing me to integrate my electrochemical expertise into their research to pursue exciting innovations. These collaborative endeavors taught me the value of multidisciplinary sciences and how a combination of efforts may readily answer scientific questions.

Over the last five years, my paths have been crossed with many individuals at VCU who inspired me to do science. One person that must be mentioned is John Arnold, VCU Chemistry building manager. My studies were quite sensitive to noise and temperature, so he dived right into resolving the difficulties that were causing the issues. I also feel so fortunate to have a support system of friends here in Richmond.

Lastly, I greatly appreciate the support and love from my wife Shanjida Akter and my son Taskin A. Rehan during my Ph.D. journey. Without having them in my life, none of the work would have been possible to accomplish. Moreover, my wife's strength, kindness, and compassion motivate me to work hard through difficult times. I appreciate my parents' efforts and sacrifices in allowing me to complete my Bachelor's and Master's degree while also inspiring me to pursue a Ph.D. and improve myself. Finally, I would like to thank the Petroleum Research Fund, Altria Graduate Research Fellowship, and Catalyst Award of VCU for funding my research.

Table of Contents

Symbols	xi
Standard Abbreviations	xiii
List of Figures	xiv
List of Tables	xvi
List of Schemes	xvii
Chapter 1: Introduction to Single Entity Electrochemistry and Signals of Microdroplet and Bacteria	
1.1 Abstract	1
1.2 Overview	1
1.3 Types of Signal	3
1.4 Seminal work and birth of a new field	4
1.5 Motivations of this dissertation	10
1.6 Single droplet spike signal	11
1.7 Single bacteria step signal	13
1.8 Transport mechanism of particles	15
1.9 Summary remarks	16
Chapter 2: Dynamics of Collisions and Adsorption in the Stochastic Electro-chemistry of Emulsion Microdroplets	
2.1 Abstract	18
2.2 Overview	18
2.3 Background	20
2.4 Novelty and Significance	20
2.5 Experimental Section	
2.5.1 Reagents	23

2.5.2 Emulsion preparation	23
2.5.3 Ultramicroelectrode construction	24
2.5.4 Instrumentation	25
2.6 Results and Discussion	
2.6.1 Droplet diameter and extent of Fc-oxidation	25
2.6.2 Droplet transport, arrival frequency and adsorption	28
2.6.3 Random walk simulation	30
2.6.4 Droplet Electrolysis	35
2.6.5 Modeling of acquisition parameters	38
2.6.6 Butler-Volmer (BV) Analysis	43
2.7 Conclusions	44
Chapter 3: Distinguishing Bacillus Size, Arrival Velocity, and Landing Orientation from Off-Surface Perturbations of Diffusional Flux in Single-Cell Blocking Electrochemistry	
3.1 Abstract	46
3.2 Overview	46
3.3 Background	47
3.4 Novelty and Significance	48
3.5 Experimental Section	
3.5.1 Reagents	49
3.5.2 Cell culturing	50
3.5.3 Bacterial cell solutions	50
3.5.4 Scanning electron microscopy	50
3.5.5 Sessile water droplet on electrode	51
3.5.6 Electrochemical and ζ -potential Instrumentation	51
3.5.7 Numerical simulations	51

3.6 Results and Discussion	
3.6.1 Bacillus blocking in a sessile droplet of water	52
3.6.2 Simulation of Δi , Δt and T_d	57
3.6.3 Transport mode of the bacteria	67
3.7 Conclusions	69
Chapter 4: Concluding Remarks and Future Direction	71
Appendix A	
A1. Cyclic voltammograms for 1 mM ferrocenemethanol for determining UME radius	74
A2. CV of 20 mM ferrocene and 400 mM trihexyltetradecylphosphonium bis(trifluoromethylsulfonyl)amide (ILPA) in toluene	75
A3. Expanded i-t curves for 50 pM of toluene droplets in water at different oxidation potentials	76
A4. Droplet distribution and random walk at the hemispherical simulation domain	77
A4.1 Simulated coordinates for 1.0 μm droplet random walk and travelled distance	78
A5. Droplet diameter vs. effective contact radius, r_{eff} , of the droplet	83
A6. Droplet adsorption from random walk and Fc electrolysis and corresponding $i - t$ curve	84
A7. Experimental current peaks of the droplet producing ~ 11 pA peak current.	85
A8. Simulated Steady-state current of 100 mM ferrocyanide solution	86
A9. Simulated ferrocyanide flux at the electrode surface	87
A10. Electron microscopy images of the bacteria	88
A11. Simulated ferrocyanide concentration perturbation by the BS at various separation distances electrode	89

Appendix B	
B1. Calculation of UME radius	90
B2. Calculation of Droplet Concentration	90
B3. Calculation of Theoretical charge for 1.0 μm droplet	91
B4. Calculation of Time required for complete electrolysis of Fc per droplet collision.	92
B5. Concentration and charge change in droplet per collision (data shown for 50 collisions).	94
B6. Calculation of Current density for 1 nm and 10 nm effective contact radius	97
B7. Determination of Bacteria cell concentration	98
B7.1 Concentration of the bacteria	98
B8. No. of steps in every 60 seconds in the experimental $i - t$ curve	99
B9. Required number of bacteria for monolayer electrode surface coverage	99
B10. Zeta potential of the bacteria at 0.01 M potassium ferrocyanide solution	100
Appendix C COMSOL report	101
References	126

Symbols

Symbol	Meaning	Units.
M	Molarity	mol/L
r_{NP}	Radius of nanoparticle	m
d_{NP}	Diameter of nanoparticle	m
Q	Charge	C
F	Faraday constant	C/mol
V_{NP}	Volume of nanoparticle	m ³
d_d	Droplet diameter	m
r_d	Droplet radius	m
C	Concentration	mol/L
R	Electroactive reduced species	
O	Electroactive oxidized species	
i	Current	A
m_0	Mass-transfer coefficient	cm/s
i_p	Peak current	A
n	Number of electrons transferred per mole	
I_l	Diffusion-limited current	A
A	Area of electrode	m ²
j_d	Redox flux	molcm ⁻² s ⁻¹
D	Diffusion coefficient	cm ² /s
f	Frequency	Hz
f_{exp}	Experimental frequency	Hz
f_{dif}	Diffusional frequency	Hz

N_A	Avogadro number	particles/mol
k_B	Boltzmann constant	$\text{m}^2\text{Kgs}^{-2}\text{K}^{-1}$
T	Temperature	K
η	Solution viscosity	Pa s
r_p	Radius of the particle	m
C_{Fc}	Concentration of ferrocene	mol/L
t_{sim}	Simulation run time	s
ζ	Zeta potential	V
v	Random walk velocity	cm/s
v_{rms}	Root mean square velocity	cm/s
δ	Step length	m
τ	Step time	s
r_{eff}	Effective contact radius	M
Δ	Change or difference	
J_{BV}	Butler-Volmer current density	A/m^2
δ_l	Diffusion layer	m
T_d	Threshold distance	m
i_{ss}	Steady-state current	A
J	Flux of particle	$\text{molcm}^{-2}\text{s}^{-1}$
J_D	Diffusional flux	$\text{molcm}^{-2}\text{s}^{-1}$
J_M	Migrational flux	$\text{molcm}^{-2}\text{s}^{-1}$
J_C	Convectational flux	$\text{molcm}^{-2}\text{s}^{-1}$
μ	Electrophoretic mobility	$\text{cm}^2\text{V}^{-1}\text{s}^{-1}$

Standard Abbreviations

Abbreviations	Title
SEE	Single Entity Electrochemistry
$i - t$	Current vs. time
UME	Ultramicroelectrode
NPs	Nanoparticles
Pico	10^{-12}
Au-UME	Gold ultramicroelectrode
Pt-UME	Platinum ultramicroelectrode
C-UME	Carbon ultramicroelectrode
Fc	Ferrocene
DLS	Dynamic light scattering
ILPA	Trihexyltetradecylphosphonium bis(trifluoromethylsulfonyl)amide
ET	Electron transfer
Ag/AgCl	Silver/Silver Chloride reference electrode
Ag/AgNO ₃	Silver/Silver nitrate reference electrode
PDI	Polydispersity Index
CV	Cyclic Voltammogram
Bacilli	Rod-shaped bacteria
FCN	Ferrocyanide [$\text{Fe}(\text{CN})_6^{4-}$]

List of Figures

	Title	Page no.
1.1	Schematic diagram of ensemble and single entity electrochemistry	1
1.2	Simulated erratic trajectories of 1.0 μm toluene droplet resulting from a 5 s random walk in water	2
1.3	Schematic diagram of (A) Direct electron transfer. (B) Blocking of electrochemical reaction	3
1.4	Optical micrograph of fluorescence bead adsorptions on the disk UME edge	5
1.5	Schematic representation of the collisions of emulsion droplets containing ferrocene (Fc) with a Au-UME	9
1.6	Schematic representation of the collisions and adsorption of emulsion droplet containing redox species (R) with a UME	11
1.7	Schematic representation bacteria adsorption on UME at electrode blocking technique	13
2.1	Optical microscopic image of toluene in water emulsion system	23
2.2	Current vs time graphs of toluene droplets in water at different oxidation potentials	26
2.3	Droplet diameter distribution by DLS and electrochemistry	28
2.4	Current vs time ($i - t$) graphs of toluene droplet's adsorption at electrode blocking experiments	30
2.5	Random distribution of 200 droplet particles inside the simulation hemisphere domain	31
2.6	Simulated random-walk of 5 s for a droplet of 1 μm -diameter	33
2.7	Collision locations of the droplet on UME surface	34
2.8	Simulated $i - t$ collision data for a 1 μm -droplet with an electrode of 6 μm in diameter	37
2.9	Filtered simulated $i - t$ collision data	39
2.10	Random walk approach until contact with the electrode and ferrocene concentration change upon droplet adsorption	41

2.11	Simulated and experimental $i - t$ responses for an adsorbed 1 μm droplet	42
3.1	$i - t$ curves for bacilli adsorption at a sessile droplet of water	53
3.2	Sessile droplet CV of FCN on 10 μm platinum electrode	54
3.3	Δi -distribution for bacilli in sessile droplet of water	55
3.4	Simulation of blocking at the UME-edge due to bacteria adsorption	59
3.5	Simulated Δi for bacilli adsorption at different locations on a 10 μm -diameter UME	61
3.6	Simulated Δi -traces for bacilli blocking overlapped with experimental Δi	64
3.7	Simulated Δi -values for bacilli at various distances from the UME-edge along the z -axis.	66
A1	CV for 1 mM ferrocenemethanol for determining UME radius	74
A2	CV of 20 mM ferrocene and 400 mM trihexyltetradecylphosphonium bis(trifluoromethylsulfonyl)amide (ILPA) in toluene	75
A3	Expanded $i - t$ curves for 50 pM of toluene droplets in water at different oxidation potentials	76
A4	Droplet distribution and random walk at the hemispherical simulation domain	77
A5	Droplet diameter vs. effective contact radius, r_{eff} , of the droplet	83
A6	Droplet adsorption from random walk and Fc electrolysis and corresponding $i - t$ curve	84
A7	Experimental current peaks of the droplet producing ~ 11 pA peak current	85
A8	Simulated steady-state current of 100 mM ferrocyanide solution	86
A9	Simulated ferrocyanide flux at the electrode surface	87
A10	Microscopy images of the bacteria	88
A11	Simulated ferrocyanide concentration perturbation by the <i>B. subtilis</i> at various separation distances electrode	89

List of Tables

	Title	Page no.
2.1	Characterization of toluene in water emulsion by DLS and electrochemistry	27
3.1	Most frequent values of Δi for bacillus distributions	57
3.2	Diffusion coefficient and frequency values for Bacilli.	68
A4.1	Simulated coordinates for 1.0 μm droplet random walk and travelled distance	78
B5	Change of concentration and charge in 1.0 μm droplet per collision	94
B7.1	Concentration of the bacteria	98
B8	No. of steps in every 60 seconds in the experimental $i - t$ curve for bacilli adsorption	99
B9	Required number of bacteria for monolayer electrode surface coverage	99
B10	Zeta potential of the bacteria at 0.01 M potassium ferrocyanide solution	100

List of Schemes

	Title	Page no.
2.1	Binning and filtering of simulated $i - t$ collision data.	38
3.1	Threshold distance T_d where perturbations of J_d become detectable from baseline during <i>B. subtilis</i> arrival.	47
3.2	Sessile droplet and set up of the UME, counter, and reference electrode	52
3.3	Simulation of bacillus arrival in steps of increasing degree of blocking from a threshold distance T_d .	62

This page is intentionally left black

Chapter 1: Introduction to Single Entity Electrochemistry and Signals of Microdroplet and Bacteria

1.1 Abstract: Single Entity Electrochemistry (SEE) is an emerging electrochemical technique that has been used to characterize discrete entities by measuring the change in current during individual stochastic events (collision or adsorption) of an entity with an ultramicroelectrode of similar dimensions. The basic principle of SEE is presented in this chapter, along with the two types of signals that typically appear in the current vs. time graphs. Following this, seminal works in this field are highlighted with respect to the importance of particle collision and adsorption dynamics with UME. Later, the motivation for this dissertation, which is to investigate the collision and adsorption dynamics of microparticles, their related SEE signals, and their mass-transport mechanisms are described. Finally, the concluding remarks describe the findings of the dissertation along with prospective future applications that will promote the growth of SEE for microparticle analysis.

1.2 Overview: Electrochemistry is a powerful technique wherein current vs. potential or current vs. time graphs are usually recorded of a redox species reacting on an electrode surface. Analysis of these graphs can provide insight into the chemical and physical properties of the redox species such as kinetics, reaction mechanism, catalysis, sensing, and reversibility of the system.¹ Traditionally, electrochemical techniques are focused on ensemble average

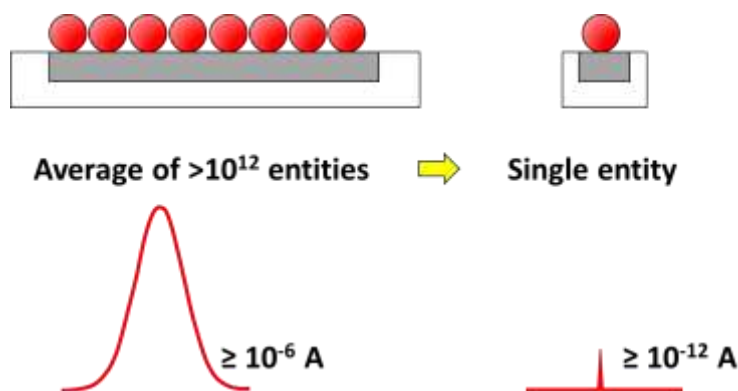


Figure 1.1: Schematic diagram of ensemble and single entity electrochemistry.

analysis (Fig. 1.1), in which micro (10^{-6} M) to millimolar (10^{-3} M) analyte concentrations are allowed to react on a millimeter dimensions (2-3 mm) of electrode (macro electrode). Thus, on average 10^{-6} A to 10^{-3} A current passes through the circuit resulting from $\geq 10^{12}$ analytes reacting on the macro electrode surface. It masks the heterogeneity of the systems, which can provide a deeper understanding of the underlying chemistry and analyte dynamics. In contrast, single entity electrochemistry (SEE) offers an unprecedented opportunity to analyze individual analyte particles. Generally, SEE measurements are performed in the solution phase by recording current vs. time ($i - t$) graphs. Spatial and/or temporal resolution of the individual signals are achieved by using ultralow analyte particle concentration (fM to pM) and employing a miniature electrode of 0.1 – 25 μm diameter termed ultramicroelectrode (UME). This UME provides an additional advantage in SEE experiments by reducing the double layer charging current and facilitating the pico-ampere (10^{-12}) level current resolution resulting from the individual analyte particle collision and/or adsorption.

SEE signals arise from the stochastic collisions of the particles with the UME surface, meaning the occurrence of individual signals is non-deterministic and governed by probabilities.² For instance, one cannot predict when a particular collision between the particle and UME will occur; however, a prediction can be made for a specified period of time. Therefore, the observed signals are time-dependent, having a quiet time between the signals that fluctuate randomly. This stochastic collision is a characteristic of Brownian motion

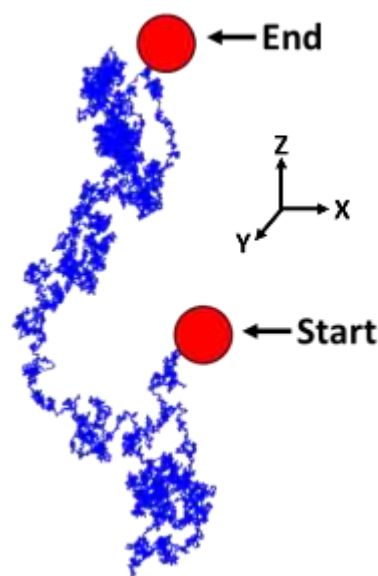


Figure 1.2: Simulated erratic trajectories (blue traces) of 1.0 μm toluene droplet (red circle) resulting from a 5 s random walk in water.

that generates from the particle's constant bombardment with solvent molecules causing erratic trajectories (Fig. 1.2). These trajectories are independent, and the average displacement is Gaussian-distributed.³ The probability of finding a particle at any position depends on its initial position with a displacement dependent on its diffusion coefficient and elapsed time.⁴

1.3 Types of signal: Typically, SEE signals appear as spikes (Fig. 1.3A) or steps (Fig. 1.3B) in the $i - t$ graphs. Spike signals arise from direct electron transfer (Fig. 1.3A) between the analyte particle and the UME.⁵⁻¹⁴ In contrast, step signals arise from

blocking a parallel electron transfer reaction occurring at the UME when an insulating particle adsorbs (Fig. 1.3B).¹⁵⁻³⁰ Details of these signals relevant to this dissertation are discussed later in this chapter. This technique was first applied to characterize polymeric beads about 18 years ago.¹⁵ In later years, metal nanoparticles (NPs) were extensively characterized using this technique. The current signals resulting from these experiments were analyzed to infer their size distributions, catalytic activities, and charge-transfer kinetics.^{5-13, 31-41}

However, recent simulations indicate that current signals (Fig. 1.3A) previously thought to arise from individual metal NP collisions are comprised of multiple nanosecond impacts that are not resolvable by present-day instrumentation.⁴²⁻⁴⁴ Meanwhile, SEE has prompted fundamental research of analytes from single

molecules to living cells⁴⁵ due to its robustness in analyzing individual entities coupled with low-

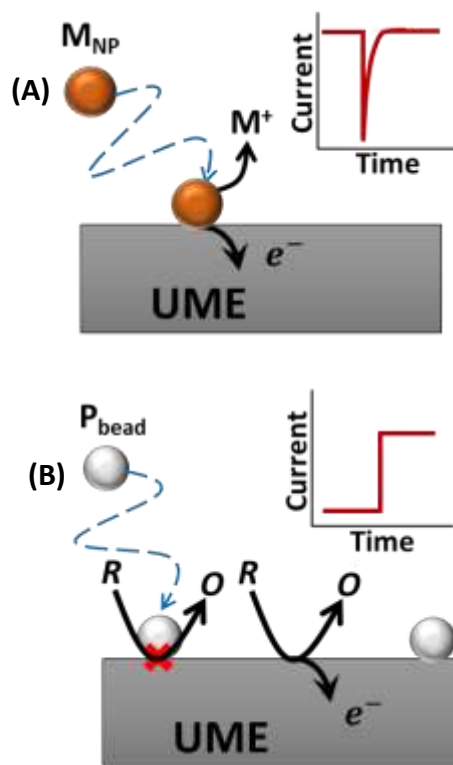


Figure 1.3: Schematic diagram of (A) Direct electron transfer. (B) Blocking of electrochemical reaction. M_{NP} = Metal nanoparticle, P_{bead} = Polymeric bead, UME = Ultramicroelectrode

cost experimental design. Particularly, analysis of microparticles such as emulsion droplets,⁴⁶⁻⁵⁷ vesicles,⁵⁸ blood,⁵⁹⁻⁶⁰ and bacterial cells⁶¹⁻⁶³ using SEE technique has gained significant interest. In most of the cases, the fundamental findings were limited to counting the particles and estimating their sizes.⁶⁴

1.4 Seminal work and birth of a new field: The core principle of this dissertation is an expansion of the recently developed SEE technique that relies on the individual collisions of particles with a UME. The motion of the particles is stochastic, and the electrochemical signal arises due to an electrochemical reaction coupled with the collision. The first quantitative application of this technique was demonstrated by Lemay *et al.* at his landmark work in 2004 by detecting individual insulating polystyrene beads (150 nm) on a 2.5- μm gold (Au) UME.¹⁵ The experimental design was simple, where diffusion-limited ferrocenemethanol oxidation was carried out on an Au-UME surface. After introducing the polystyrene beads to the solution, individual adsorption of the beads on UME blocked the ferrocenemethanol oxidation. Each adsorption event appeared as a step-like current decrease in the $i - t$ graphs (Fig. 1.3B), which is now widely known as electrode blocking experiment.¹⁵ Later, in 2013, Bard *et al.* expanded upon this technique with experiments and simulations using COMSOL Multiphysics to correlate the current step height resulting from blocking events with the size of silica spheres (310 nm) on a 2- μm platinum (Pt) UME.¹⁶ Additionally, their simulation revealed that inhomogeneous redox flux around the disk shaped UME might result in dissimilar current steps for the same sphere adsorbing at different locations on UME. Radial diffusional flux of the redox reporter dominates on the electrode edge, meaning insulating spheres adsorbing on the UME edge produce larger current steps than those adsorbing towards the center of the UME. This phenomenon has been termed the edge effect.⁶⁴ In 2013, Crooks *et al.* tracked the movements and adsorption of individual carboxyl-modified fluorescent

polystyrene beads on a 10- μm Pt-UME and quantified the edge effect.¹⁷ The optically-tracked beads produced step-like current signals in the $i-t$ graphs by blocking the 1,1'-

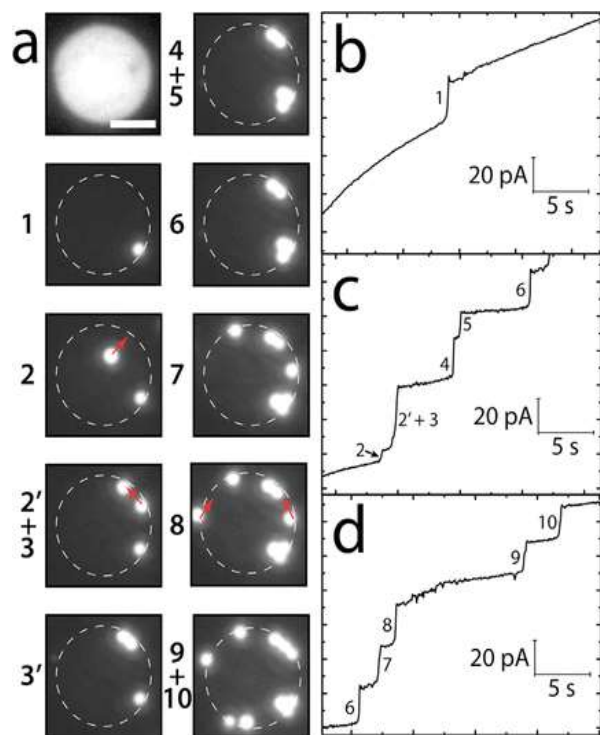


Figure 1.4: (A) Optical micrograph of fluorescence bead adsorptions on the disk UME edge and (b), (c), (d) are respective current signals. Taken from reference 17

ferrocenedimethanol flux upon adsorption on the UME surface. The experimental step height was correlated to the tracked landing positions of the beads using COMSOL Multiphysics simulation. The simulations and optical tracking revealed that maximal current step height was observed for beads adsorbing on the edge of the disk UME due to maximum blocking of 1,1'-ferrocenedimethanol flux. Additionally, optical tracking showed that the beads prefer to adsorb on the electrode edge where the redox flux is highest on the UME (Fig. 1.4).¹⁷ In a recent 2020 report, Lemay *et al.* introduced the influence of particle dimensionality on current steps observed

in electrode blocking experiments.⁶⁵ Using COMSOL simulations, they demonstrated that a 3D sphere could yield a higher current step than a 2D sheet of similar projected area adsorbed on the same location on the UME surface. This is because the former can block direct electron transfer and redox flux to the electrode surface, while the latter only blocks the direct electron transfer. Meanwhile, in 2016, Park *et al.* first reported the detection of *E. coli* bacteria by electrode blocking experiments.⁶¹ They also performed simulation with COMSOL Multiphysics, which showed that the simulated current step height was similar in magnitude to the measured experimental value.

Later in 2018, Thorgaard *et al.* optically tracked bacteria movements near the UME surface while recording the ferrocenemethanol oxidation current. In their experimental conditions, *E. coli* produced permanent current step upon adsorption on UME. In contrast, *B. subtilis* produced permanent and transient current steps by adsorbing and bouncing back off the UME surface, respectively.⁶² The optical tracking revealed that the *B. subtilis* permanently adsorbs if it collides on the UME center while bouncing back from the UME edge. However, with their limited optical and experimental data, quantitative reasoning for this observation was not attainable. In subsequent work, using COMSOL simulations, they demonstrated that the low ionic strength solution (2 mM ferrocenemethanol, 0.1 mM KCl) results in a high electroosmotic flow ($\geq 50 \mu\text{m/s}$) of the solvents from the UME edge to the surrounding glass surface. Thus, the bacteria colliding on the UME edge may experience this high electroosmotic flow and appear as a bouncing event due to being carried away by the solvents. Yet, the different behavior of the *E. coli* and *B. subtilis* in same low ionic strength electrochemical solution indicates that more studies are required on bacteria dynamics to deconvolute such complex behavior. In the meantime, Mirkin *et al.* reported the detection of *S. maltophilia* and *E. coli* using 100 mM $\text{Fe}(\text{CN})_6^{4-}$ on a 25- μm Pt-UME.⁶³ Additionally, they demonstrated that bacteria adsorption on edge produced largest current steps compared to the bacteria adsorbed on the electrode center.⁶³ These studies highlighted the significance of particle movements near and on the electrode surface. Thus, emphasis on particle dynamics is essential to correlate the respective physicochemical behavior with step-like signals.

In the case of the spike response, Bard *et al.* were the first to report a corresponding example of 2-nm platinum nanoparticle colliding on a carbon (C) UME of 8- μm in diameter. The large catalytic reactivity of the Pt NPs towards the reduction of protons to produce H_2 , manifested as a spike response upon contact with the C-UME that was inert to the same reaction.⁶⁶ This study

sparked a series of reports aimed at understanding the transition from spike to staircase (step-like) response due to adsorption,³⁹ gas bubbling,^{41, 67} and other effects.^{32, 34} However, the most relevant studies to reveal collision dynamics came out of the Compton lab, who reported the oxidation of Ag NPs, 20-50 nm in diameter colliding with a 22- μ m diameter C-UME. The reaction $Ag (NP) \rightarrow Ag^+ + e^-$, was proposed to occur during collisions that appeared as spikes in the $i - t$ graphs when the potential was positive enough to oxidize Ag (Fig. 1.3A).⁷ Each spike that lasted for 1-10 ms was attributed to individual collisions comprising the total oxidation of an Ag NP. The diameter of the NP, d_{NP} , was calculated by first integrating the current over the collision time (spike width) to determine the charge, Q , as indicated by Eq. 1.1, where n is the number of electrons for the reaction, N is the number of moles and F is the Faraday constant. Eq. 1.2 relates Q with the volume of the spherical NP, V_{NP} , the density of Ag, ρ_{NP} , the relative atomic mass, A_r , and the NP-radius, r_{NP} .

$$\int idt = Q = nNF \quad 1.1$$

$$Q = \frac{nF\rho_{NP}V_{NP}}{A_r} = \frac{nF\rho_{NP}}{A_r} \times \frac{4}{3}\pi r_{NP}^3 \quad 1.2$$

Rearranging Eq. 1.2 yield:

$$r_{NP} = \sqrt[3]{\frac{3A_r Q}{4nF\pi\rho_{NP}}} \quad 1.3$$

$$d_{NP} = 2 \times r_{NP} = 2 \sqrt[3]{\frac{3A_r Q}{4nF\pi\rho_{NP}}} \quad 1.4$$

Thus Eq. 1.3 allows the determination of the r_{NP} from the charge transfer during the impact, which is used in Eq. 1.4 to determine the d_{NP} . Assuming the complete electrolysis from the single collision of colliding NPs, this approach was applied to determine the size of organic and other metal NPs by the Compton group.^{7, 12-13, 37} However, at the time, the mechanism of silver NP oxidation (Fig. 1A) was not properly understood. Using a 3D-random walk model, Bard *et al.* revealed that transient peaks from individual collisions of NPs with UMEs were in the nanosecond domain.⁴² Revisiting their experimental work, Compton *et al.*, studied Brownian motion theoretically and concluded the previously reported millisecond response could be a cluster of current peaks of shorter collision time (Fig. 1.3A).⁶⁸ White *et al.* and Unwin *et al.* experimentally detected this multippeak behavior of the Ag NP using a current amplifier and by increasing the solution viscosity.^{43, 69-70} Additionally, random walk simulations continue to show that collisions for the size and mass of these silver NPs are of nanosecond duration, so the experimental peaks should be attributed to partial instead of complete electrolysis (Ag-NP oxidation) of the particle.^{43, 69, 71-72}

In 2014, spike responses from micrometer-sized particles were demonstrated by Bard *et al.* resulting from the electrolysis of ferrocene (Fc) trapped inside toluene droplets dispersed in water.⁴⁶ An ionic liquid, trihexyltetradecylphosphonium bis(trifluoromethylsulfonyl)amide (ILPA), was used as an electrolyte to enhance toluene conductivity and to help emulsification of the droplets. These droplets showed a zeta potential of -15.8 mV with a diameter distribution ranging from 0.4 μm to 2.0 μm . Under an oxidation potential, the Fc inside the droplet was oxidized during collisions with the $10\text{-}\mu\text{m}$ Au-UME and produced a spike response in the $i - t$ graph. As the electrode potential was high enough to attain the diffusional limit of the reaction, the redox content inside the droplet was assumed to electrolyze completely following the bulk

electrolysis model.^{46, 49-50} In these conditions, the current is expected to follow an exponential decay if the reaction is performed at a constant potential.¹ After measuring Q , the droplet size, d_d , was determined from Faraday's law expressed in Eq. 1.5 for a spherical particle.⁴⁶

$$d_d = 2 \times r_d = 2 \sqrt[3]{\frac{3Q}{4\pi n F C_{redox}}} \quad 1.5$$

where n is the number of electron transfers, r_d is the radius of the droplet, and C_{redox} is the concentration of Fc inside the droplet. The droplet size distribution obtained by this method matched with the values from dynamic light scattering (DLS) data. In a subsequent work, Bard *et al.*, studied the electrolysis of tetracyanoquinodimethane (TCNQ) in nitrobenzene droplets dispersed in water. Given that nitrobenzene is oxidized at a higher potential than TCNQ, the exponential decay of current peaks for both

nitrobenzene and TCNQ was interpreted as indicative of a constant droplet volume during electrolysis. This study was performed on a 10- μm C-UME, and also confirmed the agreement of diameter distribution determined by electrolysis (Eq. 1.5) and DLS.⁴⁹ Other experiments with benzene and cyclohexane emulsion droplets to study the oxidation of ferrocene, decamethyl-ferrocene, and zinc metalloporphyrin (ZnTPP) (Fig. 1.5), showed that ion transfer across the

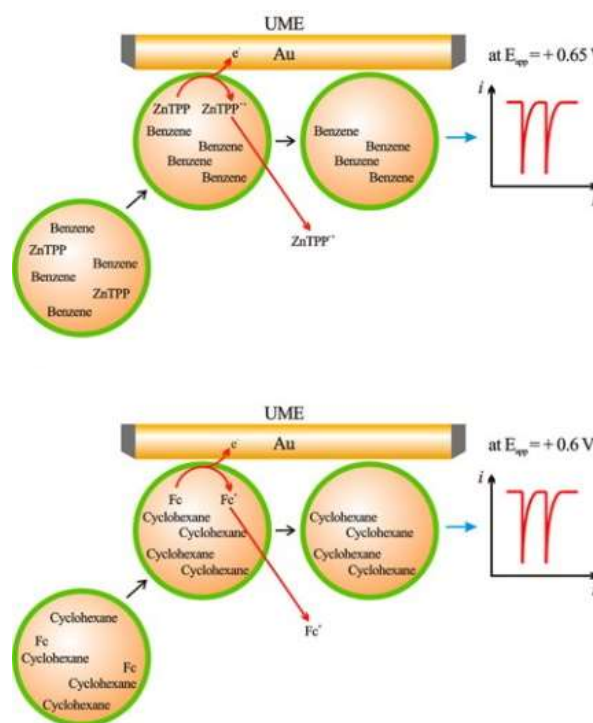


Figure 1.5: Schematic representation of the collisions of emulsion droplets containing ferrocene (Fc) with a gold UME. Taken from reference 50.

oil/water interface was required to maintain charge neutrality and observe current spikes.⁵⁰ This was further corroborated for the oxidation of rubrene (both oxidation states are hydrophobic), whose peaks were not observed unless an interfacial exchangeable ion (cation or anion) was added to the system. In contrast, spikes were observed for the oxidation of decamethyl-ferrocene, thus indicating that decamethyl-ferrocenium transfers from the toluene droplet to the aqueous phase once oxidation occurs (Fig. 1.5).⁵⁴ The electrolysis time of these emulsion droplets loaded with redox molecules lasted two orders of magnitude higher than the electrochemical oxidation of silver NPs^{46, 49-51, 54} which was an early indication of droplet adsorption on the UME as suggested by Bard *et al.* when reporting droplet blocking experiments.⁴⁶

1.5 Motivations of this dissertation: In 2014, Bard *et al.* reported the SEE of emulsion droplets with both spike and step-like responses, attributing the former to complete electrolysis of the droplet redox content and the latter to droplet adsorption.⁴⁶ This was followed by experimental investigations into the exchange of ions across the droplet interface, but interaction dynamics of these microdroplets with the electrode were not addressed.^{48-51, 54} Meanwhile, analysis of microparticles such as vesicles,⁵⁸ blood,⁵⁹⁻⁶⁰ and bacterial cells⁶¹⁻⁶³ using SEE technique gained interest. In most cases, the fundamental findings were limited to counting the particles and estimating their sizes.⁶⁴ At present, simulations of collision dynamics that mimic the spike response in Fig. 3A have been performed with non-adsorbing silver NPs,⁴³ while modeling of the blocking response has been done with polymer beads,^{16-17, 73} and more recently with bacteria and red blood cells.^{60, 63, 74} However, the correlation of collision and adsorption dynamics of these microparticles on the UME to the resulting current signals remained unexplored. This is particularly crucial if SEE is to be used for probing the physiological state of living cells, which have shown to adsorb on UME surfaces upon collision and whose sizes make them fall in the

microparticle range (1 to 8 μm). Thus, the physicochemical processes relevant to the SEE current signals, with a better understanding of instrumental acquisitions, are essential for analyzing the data to obtain significant insights into the microparticle system. Additionally, models that enable the inference of properties like microparticle count, charge, size, collision and adsorption dynamics, viscosity or surface tension, from the SEE-signal are still lacking. The objective of this dissertation is an integrated approach of experiments and simulations to quantify the effects of interaction dynamics (collision and adsorption) of microparticles and UMEs, to deduce properties of liquid droplets (diameter, droplet-UME contact radius, droplet redox mechanism), and bacteria (size, adsorption orientation, arrival pace). Emulsion microdroplets are utilized as a model system to correlate the collision and adsorption dynamics of microparticles on UMEs to respective SEE signals. Later, the shape effects on adsorption dynamics and the accompanying SEE signals are evaluated using three sizes of rod-shaped bacteria.

1.6 Single droplet spike signal: Emulsion droplets can be made electroactive by trapping redox species that undergoes direct electron-transfer ($R - ne \rightarrow O$) reaction. When such an electroactive droplet collides stochastically with the UME electrified at the diffusion-limited redox potential, a spike-like current signal appears in the $i - t$ graph resulting from

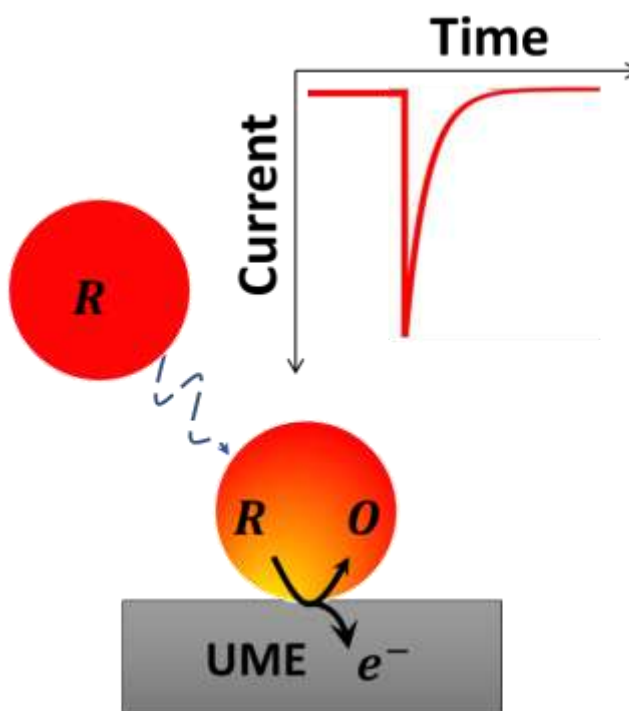


Figure 1.6: Schematic representation of the collisions and adsorption of emulsion droplet containing redox species (R) with a UME. The spike signal in the $i - t$ graph is resulted from the electrolysis of R to O .

the droplet redox reactions (Fig. 1.6). This spike current signal was first demonstrated by Bard *et al.* and was generated from the electrolysis of Fc trapped inside toluene droplets dispersed in water.⁴⁶ The redox content inside the droplet was assumed to electrolyze completely following the bulk electrolysis model, as the electrode potential was high enough to attain the diffusional limit of the reaction.^{46, 49-50} In these conditions, the current is expected to follow an exponential decay if the reaction is performed at a constant potential following the Eq. 1.16:¹

$$i(t) = i_0 e^{-\frac{m_0 A}{V} t} \quad 1.6$$

where $i(t)$ is the current as a function of time, V is the droplet volume, m_0 is the mass-transfer coefficient, t is the time, and A is the droplet-UME circular contact area. This circular contact area can be attributed as a tiny disk UME having an effective contact radius, r_{eff} , hence the mass-transfer coefficient, m_0 for this geometry becomes:¹

$$m_0 = \frac{4D}{\pi r_{eff}} \quad 1.7$$

Substituting Eq. 1.7 into Eq. 1.6 yield:

$$i(t) = i_0 e^{-\frac{4D\pi r_{eff}^2}{\pi r_{eff} V} t} = i_0 e^{-\frac{4Dr_{eff}}{V} t} \quad 1.8$$

According to Eq. 1.8, at $t = 0$,

$$i(t) = i_0 = i_p \quad 1.9$$

where the time-dependent current, $i(t)$, becomes i_0 , which is the maximum peak current, i_p , observed in the spike signal, which can be estimated by the diffusion-limited current equation:

$$i_p = 4nFDCr \quad 1.10$$

where n is the number of electrons transferred per mole, F is the faraday constant, D is the diffusion coefficient of the droplet redox species, and C is the initial droplet redox concentration. Precise analysis of this current spike signal can provide valuable information about the colliding and adsorbing microdroplets on the UME. For instance, by monitoring the charge under the spike area, Chapter 2 explores the collision and adsorption dynamics of a $1.0\ \mu\text{m}$ diameter toluene droplet on a $5.0\ \mu\text{m}$ diameter UME. The charge provides evidence of irreversible droplet adsorption on the UME surface and points to a universal principle of chemical sensing: adsorption far surpasses the efficiency of collisions. Additionally, this chapter demonstrates the importance of instrumental acquisition frequency for proper interpretation of the spike signals and the utility of spike frequency for inferring droplet transport mechanisms to the UME surface.

1.7 Single bacteria step signal:

Insulating particles such as bacteria can be detected using electrode blocking SEE experiments.¹⁵ Typically, a diffusion-limited redox reaction is continuously happening on the UME

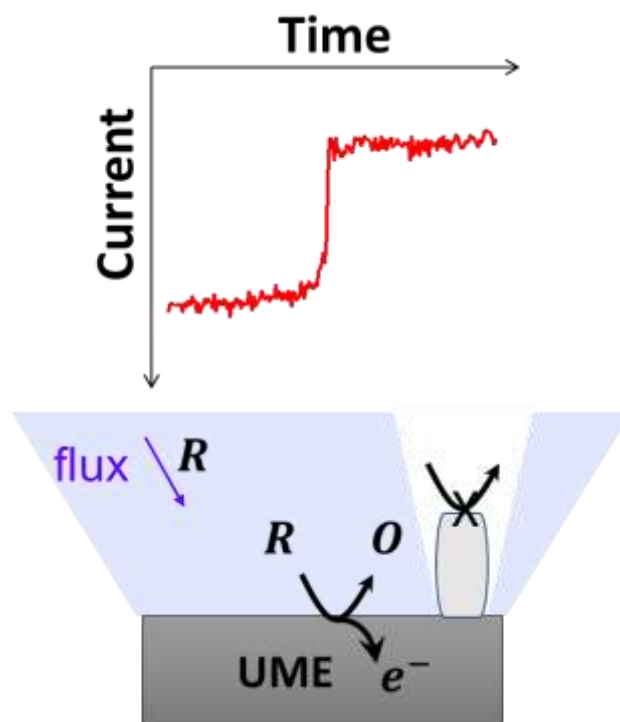


Figure 1.7: Schematic representation bacteria adsorption on UME at electrode blocking technique. The step signal in the $i - t$ graph is resulted from the blocking of electrolysis R to O.

surface, while the adsorbing bacteria blocks the redox flux and appears as a step on the $i - t$ graphs (Fig. 1.7). To understand the origin of the step-like response, we need to emphasize the redox flux

and faradaic reactions happening on the UME surface. The diffusion-limited current of a redox species R on a disk UME is calculated as:¹

$$I_l = nFj_dA \quad 1.11$$

where n is the number of electrons transferred per mole, F is the faraday constant, j_d is the redox flux, and A is the area of the electrode. The redox flux of the disk-shaped UME depends on the diffusion coefficient of the redox species, D , and the mass-transfer coefficient, m_0 , according to the equation:

$$j_d = m_0C = \frac{4DC}{\pi r} \quad 1.12$$

Substituting Eq. 1.12 into Eq. 1.11 we get,

$$I_l = nFA \frac{4DC}{\pi r} = 4nF \frac{\pi r^2 DC}{\pi r} = 4nFDCr \quad 1.13$$

According to this Eq. 1.13, the diffusion-limited current, I_l , depends on the electrode radius, r , concentration of the redox species, C , and diffusion coefficient of the redox species, D . In the electrode blocking experiment, an adsorbed insulating particle blocks a certain portion of the direct electron transfer reaction on the electrode surface. As a result, the electroactive surface area reduces, which in turn reduces the diffusion-limited current and manifests a step-like signal in the current vs. time graphs. Additionally, Eq. 1.13 indicates that concentration fluctuations near the UME can also result in the reduction of I_l . This concentration or flux perturbation depends on the size and shape of the insulating particles. As a result, information about the insulating particles' structural features, dynamics, and transport mechanisms are encoded in the current steps. However, faster instrumental acquisitions and/or slow-moving particles are necessary to document these features in the current steps. In chapter 3, we have demonstrated that step responses can be

correlated to the bacterial size, adsorption orientation, and arrival pace to the UME surface by analyzing the flux perturbation using slow-moving bacteria and 50 ms sampling acquisitions.

1.8 Transport mechanism of particles:

In electrochemical measurements, diffusion, migration, and convection contribute to the particle arrivals to the UME surface. Usually, SEE experiments are performed in a quiescent solution with an excess of supporting electrolytes; thus, the contribution from convection and migration becomes negligible. The arrival frequency of the particle by diffusion is related to its concentration, C , mass transfer coefficient, m_0 , Avogadro number, N_A , and the area of the electrode, A , by the following equation:

$$f = Am_0CN_A \quad 1.14$$

This is simply a solution of Fick's diffusion law which predicts the collisional frequency of diffusing particles with an electrode having an area of A .¹ The mass transfer coefficient of the particle, m_0 , in Eq. 1.14 depends on the electrode geometry. For a disk UME m_0 is expressed by:¹

$$m_0 = \frac{4D}{\pi r} \quad 1.15$$

Substituting Eq. 1.15 into Eq. 1.14 we get,

$$f = ACN_A \times \frac{4D}{\pi r} = \pi r^2 CN_A \times \frac{4D}{\pi r} = 4DCrN_A \quad 1.16$$

Thus, according to Eq. 1.16, the diffusional arrival frequency can be estimated if the diffusion coefficient of the particle is known. For a spherical particle, like emulsion droplet, the diffusion coefficient, D , is always calculated using the Stokes-Einstein equation:

$$D = \frac{k_B T}{6\pi r_p \eta} \quad 1.17$$

where k_B is the Boltzmann constant, T is the absolute temperature, η is the solution viscosity, and r_p is the radius of the particle. However, in Chapter 3, we use the diffusion coefficient formula developed by Tirado and Garcia de la Torre for cylinders to estimate the diffusion coefficient of rod-shaped bacteria having length (a) and width (b):⁷⁵⁻⁷⁷

$$D = \frac{k_B T}{3\pi\eta a} \left[\ln\left(\frac{a}{b}\right) + w \right] \quad 1.18$$

$$w = 0.312 + 0.565 \frac{b}{a} - 0.1 \frac{b^2}{a^2} \quad 1.19$$

In a quiescent solution, one can estimate the mode of particle transport to the electrode surface by comparing the value predicted by Eq. 1.16 with the experimental frequency. A good agreement between these two indicates that particles arrive at the electrode surface by diffusion (See droplet arrival section in Chapter 2). In contrast, a higher experimental frequency (usually one or two orders of magnitude) than the predicted frequency by Eq 1.16 strongly suggests that the particles arrive at the electrode surface by migration. (See bacteria transport mode section in Chapter 3).

1.9 Summary remarks: SEE has risen to the forefront of chemical measurement and analysis as a distinct field of study.⁴⁵ This field provides an unprecedented opportunity to electrochemically investigate individual analyte particles ranging from single molecules to living cells. This holds a great promise, especially for studying biological cells, which are challenging to study in bulk due to their complicated electrochemical behaviors. Yet selective and specific detection remains a challenge for this growing field. To address this, the correlation of collision and adsorption dynamics to the SEE signals is crucial. Such studies are mostly developed for nanoparticles which aided in advancing this discipline in terms of selective detection, kinetics, and catalytic investigations of NPs.⁶⁴ Except for our recent contribution in this field, no dynamic model for the

collision and adsorption of droplets of micrometer size is available.⁷⁸ Furthermore, this work demonstrates that universal principles, such as the greater efficiency of adsorption over collision, could be hypothesized from the individual SEE response. While such progress is made in Chapter 2, Chapter 3 illustrates the impacts of shape effects using three different rod-shaped bacteria on their adsorption dynamics and respective SEE signals in electrode blocking experiments. Based on this technique, this is one of the few reports that demonstrate an in-depth analytical study on single bacteria's size, shape, velocity, and adsorption dynamics. This also demonstrates the utility of SEE to determine cytometric properties of live microorganisms, which could be a source of analytical selectivity for detecting pathogens based on size, landing orientation, and approach speed. Additionally, the fundamental insights obtained by the emulsion droplets and the adsorption dynamics of single bacteria will advance the field to design selective and specific sensors for relevant microparticles such as red blood cells, cancer cells, and sickle cells. Furthermore, these findings will facilitate the studies of ion-transfer kinetics across the interface, drug-partitioning for drug delivery applications, and fundamental studies such as merging SEE signals to bulk signals.

Chapter 2: Dynamics of Collisions and Adsorption in the Stochastic Electro-chemistry of Emulsion Microdroplets

2.1 Abstract: Current-time recordings of emulsified toluene microdroplets containing 20 mM Ferrocene (Fc), show electrochemical oxidation peaks from individual adsorption events on disk UME (5 μm diameter). The average droplet diameter ($\sim 0.7 \mu\text{m}$) determined from peak area integration was close to Dynamic Light Scattering measurements ($\sim 1 \mu\text{m}$). Random walk simulations were performed deriving equations for droplet electrolysis using the diffusion and thermal velocity expressions from Einstein. The simulations show that multiple droplet-electrode collisions, lasting $\sim 0.11 \mu\text{s}$ each, occur before a droplet wanders away. Updating the Fc-concentration at every collision shows that a droplet only oxidizes $\sim 0.58 \%$ of its content in one collisional journey. In fact, it would take $\sim 5.45 \times 10^6$ collisions and $\sim 1.26 \text{ h}$ to electrolyze the Fc in one droplet with the collision frequency derived from the thermal velocity ($\sim 0.52 \text{ cm/s}$) of a $1\text{-}\mu\text{m}$ droplet. To simulate adsorption, the droplet was immobilized at first contact with the electrode while electrolysis current was computed. This approach along with modeling of instrumental filtering, produced the best match of experimental peaks, which were attributed to electrolysis from single adsorption events instead of multiple consecutive collisions. These results point to a heightened sensitivity and speed when relying on adsorption instead of collisions. The electrochemical current for the former is limited by the probability of adsorption per collision, whereas for the latter, the current depends on the collision frequency and the probability of electron transfer per collision (JACS, 2017, 139, 16923-16931).

2.2 Overview: This chapter reports a comprehensive investigation combining experiments with an electrochemical random walk simulation to elucidate the electrochemical response of single emulsion droplets on UMEs. The new important result is the illustration that for electrolysis of

individual droplets, irreversible adsorption is far more effective than non-adsorptive collisions. For instance, during one adsorption event, a 1 μm -droplet transfers 99% of charge during ~ 0.6 s, while 6680 collisions only deliver 0.58% in ~ 0.7 s. This observation ratifies another aspect of reactivity for stochastic electrochemistry, whereby the current signal of redox active entities that attach irreversibly to an electrode, is not limited by the electrode collision frequency but rather the probability of adsorption per collision. This stands in contrast to non-adsorptive nanoparticles (NPs)⁷⁹ and molecules⁸⁰ for which their electrochemical response is limited by their electrode collision frequency and the probability of electron transfer (ET) per collision.⁷⁹⁻⁸⁰ We reached this insight by combining a random walk model of emulsion droplets with their adsorption and electrolysis, including instrumental filtering to quantitatively reproduce the electrochemical response. The latter comprises the magnitude, shape and frequency of current peaks reflecting single droplet events.

Our results are highly relevant to the present quest for bio-electrochemical sensing of single cells,^{22-23, 81-83} which happen to be of micrometer dimensions (1-15 μm) and adsorb spontaneously on surfaces. For example, cancer cells,⁸¹ blood cells,⁸² bacteria,²²⁻²³ alga cells,⁸³ and even abiotic suspensions of microparticles,⁸⁴⁻⁸⁵ fall in this size range and have also been shown to adsorb by stochastic electrochemistry.

The unique insight of the results presented here lies on three points: first, random walks to predict electrochemical parameters informed by the dynamics of the random walk are rare,^{79-80, 86} so this work introduces a new example for the electrolysis of a redox species confined in a droplet. Second, we demonstrate that signals from individual adsorption events are amplifications of multiple short collisions that lead to the high sensitivity of adsorptive sensors. Finally, such sensing

principle is anticipated to be universal because all microscopic entities, from blood cells to molecules, follow Einstein laws of diffusion but with different collision timescale.⁸⁷

2.3 Background: Previously, electrochemical random walk simulations have been performed for redox molecules with different diffusional constraints.^{80, 86, 88} The electrochemical response of redox active NPs with diameters ranging from 10 to 70 nm has also been simulated by random walk.^{79, 89-91} The general approach has consisted of deriving quantitative relations between the ET current and the root mean square velocity, $v_{rms} = (3k_B T/m)^{1/2}$,⁷⁹⁻⁸⁰ which Einstein applied to diffusing particles.⁸⁷ Here k_B is the Boltzmann constant, T is the absolute temperature and m is the mass of the particle. For instance, $\sim 1 \times 10^4$ and ~ 4.5 cm/s are estimates of v_{rms} for a molecule^{80, 92} and a 70 nm-Ag-NP,⁷⁹ respectively. These are instantaneous mass-dependent velocities induced by thermal energy, that upon random collisions with the medium and the electrode, render the values of diffusion coefficient and electrode collision frequency that we measure (see below). Despite v_{rms} being 3-orders of magnitude apart, the electrochemical current for both the molecule and the Ag-NP, turns out to be limited by the electrode collision frequency and the probability of ET upon collision.⁷⁹⁻⁸⁰ As noted by White and coworkers, for molecules this is only true in the “kinetic control regime”,⁸⁰ and with the caveat that the molecular collisional model underestimates ET-rates by ignoring activation from inner and solvent-reactant vibrations as well as tunneling.⁹³ Nevertheless, it is insightful to use the electrode collision frequency to compare the scaling effect of mass for the three systems: molecules, NPs and microdroplets, because for the latter two, single entity events are easier to detect.

2.4 Novelty and Significance: Our simulations show that the v_{rms} for a 1 μ m-toluene droplet loaded with 20 mM of Fc is ~ 0.52 cm/s, and the particle goes through periods of electrode collisions before wandering away from the electrode. These periods typically carry on for 300 to

600 ms and comprise multiple collisions (~ 100 to ~ 6680) each lasting ~ 0.11 μs . Similar pattern was observed in the simulations of diffusing molecules and metal NPs, but with shorter timescales.^{79-80, 89} To replicate the experimental peaks with our simulation, we had to adsorb the droplet on the electrode surface to allow full oxidation of Fc because even when updating the Fc-concentration at every collision, only $\sim 0.58\%$ of Fc was oxidized. In fact, our estimations reveal that with the collision frequency derived from v_{rms} , it would take $\sim 5.45 \times 10^6$ collisions and ~ 1.26 h to electrolyze the Fc in one droplet. The nanometer-circular area of contact between droplet and electrode assumed for this calculation yielded comparable current densities computed with the Butler-Volmer equation. Additionally, the droplet size (~ 0.7 μm) determined by time integration of the current in experimental peaks, matched closely with the one measured by Dynamic Light Scattering (~ 1 μm). We corroborated adsorption by observing step-like perturbations on the electrochemical current of aqueous mediators as the droplets blocked the electrode surface in accord with previous studies.¹⁹ Therefore, our results indicate that adsorption is more efficient than a multitude of short-time collisions and that for adsorptive particles, the electrochemical current is limited by the probability of adsorption per collision instead of the collision frequency. Why is this result important? Because despite our oversimplified adsorption model, we can now expound the analytical efficiency of stochastic electrochemistry between two opposite limits of particle-surface interaction, one in which the probability of adsorption is zero (*i.e.* 70 nm-Ag-NP on gold)⁷⁹ and the other in which the probability is 1 (*i.e.* adsorption of 1 μm -toluene droplet on a carbon electrode, this work).⁷⁸ And in doing so, we confirm the intuitive result that “adsorption-based sensing” is expected to be more sensitive and faster than “collisional sensing” because the former is amplification of the latter. One irreversible adsorption event is a collision of infinite duration. The heightened sensitivity of techniques like Stripping Voltammetry, Surface Plasmon Resonance,

and others, is rooted in adsorption. Incidentally, this principle was applied in stochastic electrochemistry using an external magnet to increase arrival frequency of magnetic particles thus boosting sensitivity.⁹⁴

The motivation of this work also stems from our previous report illustrating that stochastic electrochemistry is a method sensitive enough for studying hydrogen bonding across the organic-water interface in emulsions.⁹⁵ Nevertheless, Bard *et al.*,¹⁹ were the first to demonstrate that this method could be used to determine the diameter of emulsion microdroplets (toluene, benzene, cyclohexane, nitrobenzene) loaded with various hydrophobic redox molecules including Fc.⁹⁶⁻⁹⁸ Their detailed studies showed the blocking of electrode area by droplet adsorption as well as the good fit between the current-time decay of droplet peaks and the exponential model of bulk electrolysis.¹⁹ It was also assumed that each droplet electrolyzes its contents through a nanometer-circular area of contact with the electrode. This parameter can be estimated experimentally.⁹⁶⁻⁹⁸ We followed the same approach but now coupling a random walk with electrolysis during collisions and updating the concentration of Fc at every electrode contact. To simulate adsorption, we immobilized the droplet at first collision with the electrode, and the electrolysis continued to be quantified iteratively until the end of the simulation. Guided by the work from White and coworkers,⁹⁹ we also incorporated the experimental acquisition parameters (sampling time and low-pass filtering) into the simulation. Also relevant to this work is the research on stochastic electrochemistry of water emulsion droplets in oil, for which the principles described here also apply.¹⁰⁰⁻¹⁰⁴

2.5 Experimental Section

2.5.1 Reagents: All chemicals were used reagent grade and used without further purification. Millipore water (18.2 MW cm) was used for all experiments. Toluene, Ionic Liquid trihexyltetradecylphosphonium bis(trifluoromethylsulfonyl)amide (ILPA), Ferrocene (Fc), ferrocenemethanol, Potassium ferrocyanide, Hexaammineruthenium(III) chloride, and Potassium chloride (KCl) were purchased from Sigma-Aldrich (St. Louis, MO, USA). Carbon (C) fiber was purchased from Goodfellow (Coraopolis, PA, USA). Platinum (Pt) wire was purchased from Advent Research Materials (Eynsham, UK).

2.5.2 Emulsion preparation: The emulsions were prepared using toluene and water following a reported procedure with slight modification.^{19,95} The hydrophobic ionic liquid, ILPA, was used as a supporting electrolyte and emulsifying agent. An aliquot of 100 μL of toluene containing 400 mM ILPA was added to 5 mL of degassed Millipore water in a glass vial (Fisherbrand™). This

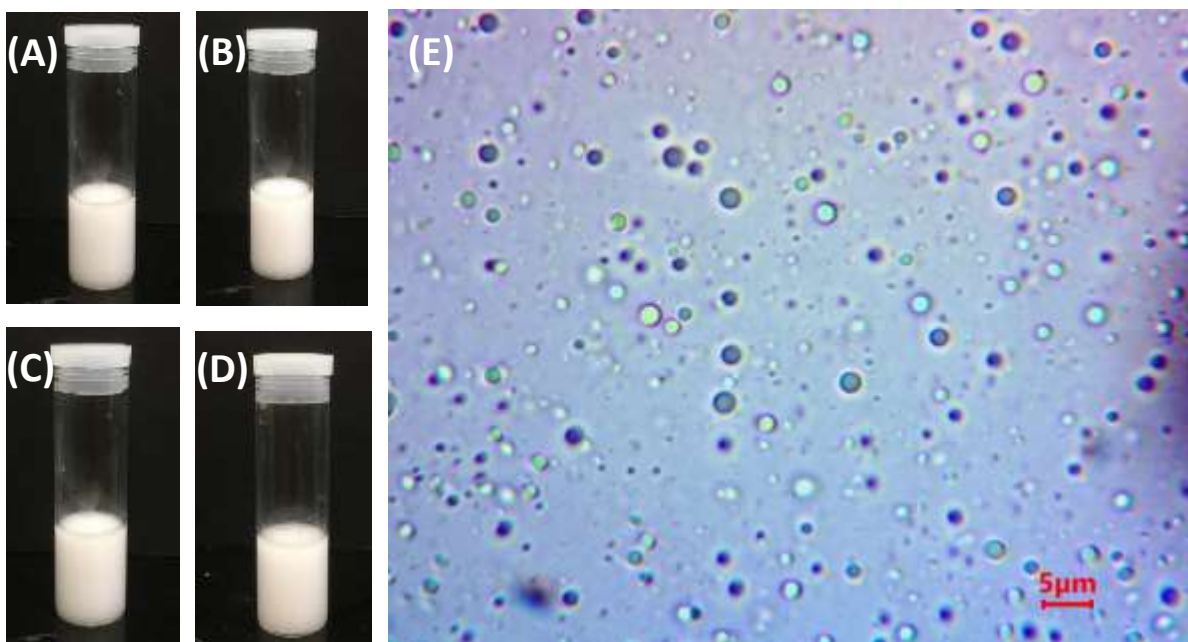


Figure 2.1: Toluene-in-water emulsion. (A) Emulsion after 5 minutes. (B) Emulsion after 1 hour. (C) Emulsion after 2 hours. (D) Emulsion after 5 hours. (E) Microscopic image of the 50 pM emulsion droplets.

mixture was vortexed for 20 seconds at maximum speed and immediately sonicated for 5 minutes. Emulsions were stable for ~5 hours (Fig. 2.1), enough for a typical 30 minute-experiment. Microscopic imaging showed that majority of droplets are below 2.0 μm and do not aggregate during the duration of the experiments. Fc-loaded emulsions had 20 mM of Fc and 400 mM ILPA, while blank emulsions only contained ILPA. The volume of the droplet was calculated using the density of toluene (0.867 g/cm^3) for an average diameter of 1.0 μm . The mole number of the droplets was computed dividing the toluene volume (0.1 mL) by the droplet volume. Finally, the molar concentration of the emulsion droplets was determined by dividing the obtained mole number of the droplets by the total volume (5.1 mL) of the emulsion (see the appendix B2 for the calculation).¹⁹

2.5.3 Ultramicroelectrode construction: The disk C-fiber and Pt- UMEs were prepared following previous literature.¹⁰⁵ Initially, a glass capillary was cleaned by sonication for 30 minutes in ethanol followed by water and oven-dried at 120°C for 2 hours. 1 cm long C-fiber/ Pt-wire was cut and cleaned with 2-propanol and finally connected with the copper wire through a conductive Ag-epoxy (epo-teck H20E, parts A and parts B). This was cured at 100°C overnight in the oven. 15% (w/w) m-phenylenediamine hardener was mixed with EponTM resin 820 and heated up to 45°C to make a clear solution. The copper wire was inserted into the clean capillary and dipped into this clear solution about 30-60 seconds and dried in the oven overnight at 120°C. The other part of the electrode capillary was sealed with Torr Seal epoxy (1:2 ratio) and dried in an oven for another 10 minutes. After successful sealing, the electrode was gently wet polished 10 to 30 seconds on 600 grit sandpaper and followed by mirror polishing with 0.05 μm alumina with DI water on micro cloth pads. The diameter of the electrodes was determined from the steady state voltammogram of 1 mM ferrocenemethanol (FcMeOH) in 0.1 M KCl aqueous solution at a scan

rate of 10 mV/s (Fig. A1, Appendix A). The calculated *diameter* of C- and Pt- UMEs are 5.0 μm and 11.4 μm , respectively (see the Appendix B1 for calculation). The diffusion coefficient used for FcMeOH was $7.80 \times 10^{-6} \text{ cm}^2/\text{s}$.¹⁰⁵

2.5.4 Instrumentation: Fisher brand Vortex Genie 2 and Branson 1510 sonicator were used to prepare the emulsions. Dynamic light scattering (DLS) measurements were done with a Zetasizer Nano ZS (Malvern, Westborough, MA) to measure droplet size and zeta potential (ζ). All electrochemical experiments were performed with a CHI 660C instrument (CH Instruments, Austin, TX) in a standard three electrode system. Ag/AgCl (3M KCl) was used as a reference electrode and a 0.5 mm Platinum wire was used as counter electrode. Sampling interval for amperometric $i - t$ curve experiments was 80 ms and low pass filter of 150 Hz. All experiments were performed at least 3 times. The “Signal Counter” program (Center for Marine and Environmental Research, Zagreb, Croatia) was used for spike identification and integration. The peak-to-peak noise (N) was estimated to be $\leq 0.2 \text{ pA}$ and the minimum current counted as signal was $\geq 4 \times N \approx 0.8 \text{ pA}$. Random walk simulations including modeling of experimental acquisition parameters were performed with MATLAB 2019b.

2.6 Results and Discussion

2.6.1 Droplet diameter and extent of Fc-oxidation: We first recorded a cyclic voltammogram (CV) in toluene with the same intra-droplet electrolyte conditions of 400 mM ILPA (emulsifier and conductivity enhancer) and 20 mM Fc using a C- UME of 5 μm in diameter. The CV obtained at 20 mV/s has a sigmoidal shape with an onset of diffusion-limited current at $\sim +0.55 \text{ V}$ vs Ag/AgCl. (Fig. A1, Appendix A). Therefore, we recorded current-time ($i - t$) curves at +0.6 V to capture the diffusion-limited oxidation of Fc, and at +0.4 V to determine the effect of oxidizing Fc

at a slower rate than its diffusion (Fig. 2.2). The response of droplets without Fc is added to show that the spikes come from Fc-electrolysis in individual droplets.

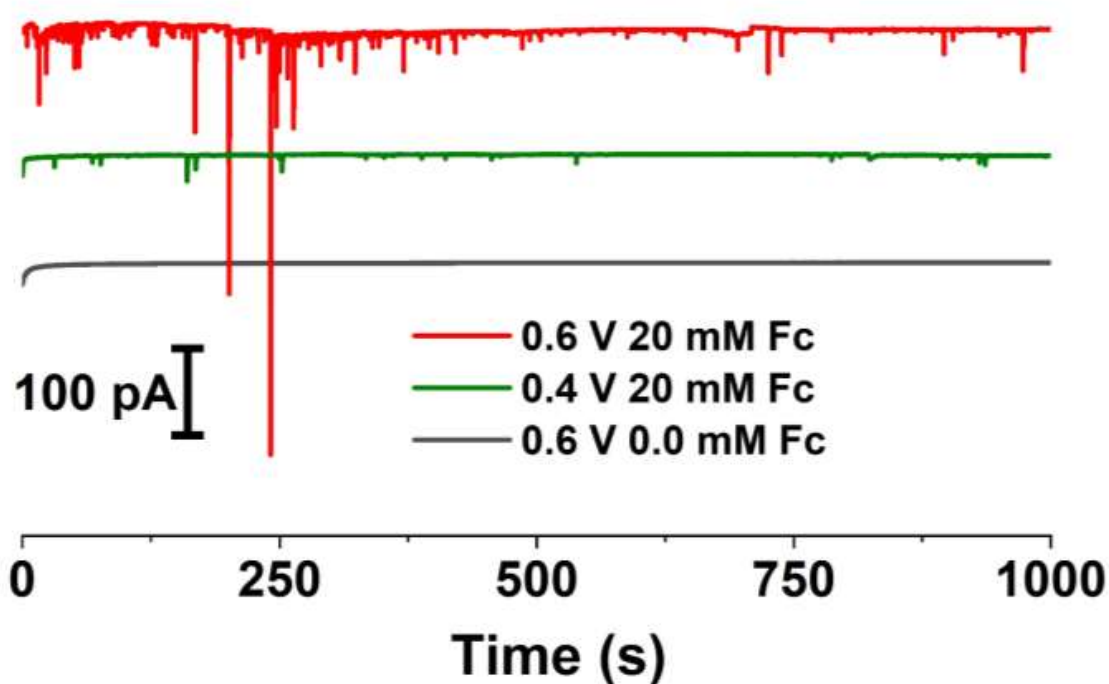


Figure 2.2: $i - t$ curves for 50 pM of toluene droplets in water at different oxidation potentials and Fc-concentration; C-UME of 5 μm -diameter.

If the droplet undergoes complete electrolysis and transfers all of its charge, the droplet diameter can be derived from the area of the electrochemical spikes (d_d) using Eq. 2.1:¹⁹

$$d_d = 2 \sqrt[3]{\frac{3Q}{4\pi nFC_{Fc}}} \quad 2.1$$

where, Q is the charge, n is the number of electrons transferred per mol of Fc, F is the faraday constant, and C_{Fc} is the concentration of Fc. This equation relates the stoichiometry of charge transfer from Faraday's law to the volume of a sphere, so that the theoretical transferrable charge for a 1 μm -droplet containing 20 mM of Fc is 1.01 pC (see Appendix B3 for calculations). Table 2.1 shows values of d_d averaged over all peaks of a $i - t$ trace recorded by triplicate (Fig. 2.2).

The diameter from dynamic light scattering (DLS), d_{DLS} , the zeta potential, ζ , and the experimental arrival frequency, f_{exp} , are also shown.

Table 2.1: Characterization by DLS and electrochemistry

Ferrocene concentration Fc/mM	Electrochemical droplet diameter, $d_d/\mu\text{m}$	DLS droplet diameter, $d_{DLS}/\mu\text{m}$	Zeta potential, ζ/mV	Experimental frequency, f_{exp}/Hz
20@0.6V	0.7±0.1	1.0±0.2	-6.8 ± 0.3	0.13±0.04
20@0.4V	0.8±0.1			0.10±0.01
0.0@0.6V	--	0.9±0.1	-5.2 ± 0.6	--

Closer inspection of Fig. 2.2 indicates that the electrochemical peaks at 0.6 V are much higher in current and have shorter time intervals than the ones at 0.4 V (Fig. A3, Appendix A). However, their corresponding values of d_d in Table 2.1 are almost identical and reasonably close to the $\sim 1.0 \mu\text{m}$ -diameter obtained by DLS (Fig. 2.3). The fact that both potentials produce the same electrolyzed charge and calculated diameter (Eq. 2.1), demonstrates that both conditions, 0.4 and 0.6 V, render total oxidation of the Fc, even though the diffusion limited oxidation is only attained at 0.6 V. Therefore, the peak duration in the $i - t$ curves of Fig. 2.2 reflect the speed of Fc-oxidation rather than length of collisions. We interpret this result as indicative of droplet adsorption.

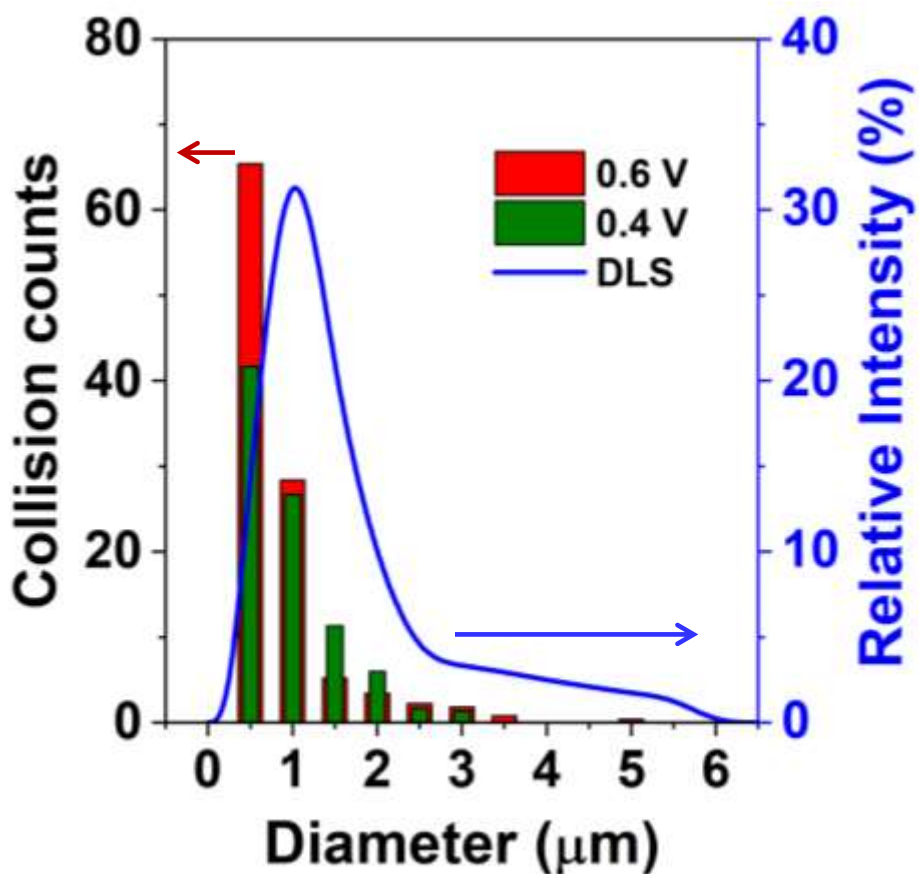


Figure 2.3: Droplet diameter distribution by DLS (blue) and electrochemistry (red and green bars).

2.6.2 Droplet transport, arrival frequency and adsorption: In quiescent solutions, the transport of particles under concentration gradients (*i.e.* due to adsorption) can be dominated by diffusion, or if the particles are charged and electric fields are present, an additional contribution from migration may take place.¹ If the particle collision is driven purely by diffusion, the arrival frequency by diffusion, f_{dif} , is approximated by Eq. 2.2:¹⁹

$$f_{dif} = 4D_d C_d r_e N_A \quad 2.2$$

where D_d is the diffusion coefficient of the droplet, C_d is the droplet concentration, r_e is the radius of the electrode, and N_A is the Avogadro's number. Eq. 2.2 is an analytical solution of Fick's laws applied to hemispherical diffusion on a microdisk electrode.¹ Using $C_d = 50$ pM and the value of

D_d estimated with the Stokes-Einstein equation (see below), the theoretical arrival frequency from Eq. 2.2 was 0.15 Hz, which is close to the experimental values of 0.13 and 0.10 Hz obtained from Fig. 2.2 and shown in Table 2.1. These results are consistent with a prevalence of diffusion over migration as hinted by the rather low values of ζ , -5.2 to -6.8 mV measured by DLS (Table 2.1). Note that agreement between f_{exp} and f_{dif} does not preclude adsorption because the latter is subsequent to collisions.

To confirm the absence of migration in droplet transport and further corroborate the occurrence of droplet adsorption, we performed electrode blocking experiments with emulsions of droplets free of Fc. These experiments consist of recording $i - t$ curves at a potential that reduces or oxidizes a redox species exclusively dissolved in the aqueous phase outside the droplets.¹⁹ Adsorption events appear as current steps, induced by electrode blockages from the adsorbed particles that disrupt the incoming flux of redox species in discrete steps.^{19, 106-108} Fig. 2.4 shows the $i - t$ curves recorded with 40 mM of two different redox species in 100 mM of KCl at potential values that render diffusion limited conditions. Due to S/N, detecting steps for concentrations lower than 40 mM with either species in Fig. 2.4 were unsuccessful. Ultramicroelectrode made of Pt metal instead of C as electrode material because the latter promoted deposition of Prussian blue when using $\text{Fe}(\text{CN})_6^{4-}$. The latter was oxidized at +0.4 V while $\text{Ru}(\text{NH}_3)_6^{3+}$ was reduced at -0.4 V on a Pt- UME of 11.4 mm in diameter. The experimental step frequency for the positive trace was 0.04 ± 0.01 Hz, and 0.03 ± 0.01 Hz for the negative one. The closeness of these values to the f_{dif} calculated with Eq. 2.2 (0.01 Hz) and using $C_d = 1.5$ pM employed in Fig 2.4, confirms that diffusion dominates droplet transport in the conditions of Figures 2.2 and 2.4. This comparison is valid despite using different electrode materials because droplets, with and without Fc, display values of ζ almost identical: -6.8 and -5.2 mV, respectively. Moreover, the low values of ζ , further

demonstrates the absence of migration as the arrival frequency is insensitive to the negative and positive polarity of the potentials employed in Fig. 2.4.

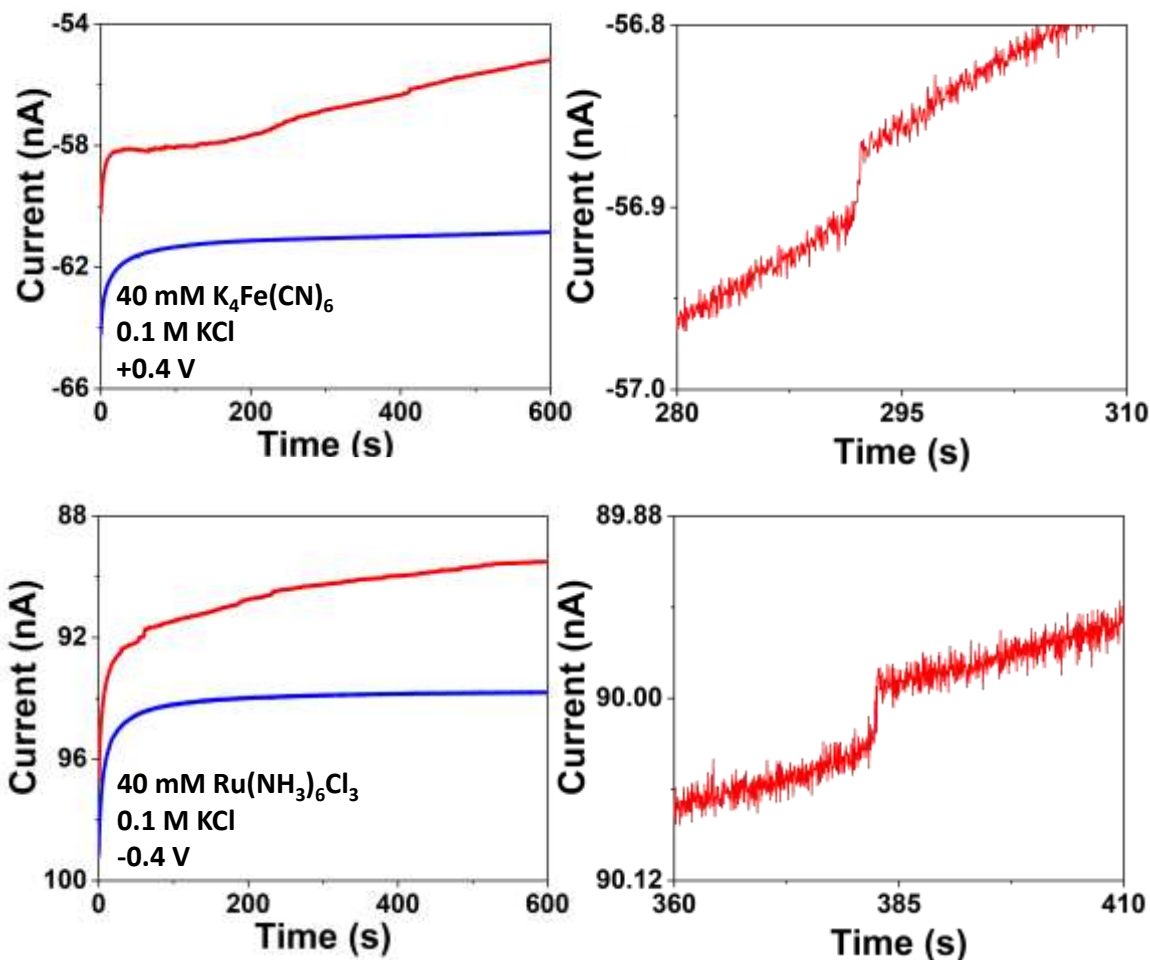


Figure 2.4: $i - t$ curves for 0.0 (blue) and 1.5 pM (red) of blank toluene droplets with aqueous redox reporters reacting at a Pt- UME of 11.4 mm-diameter. The right panel is a blow out of the red trace on the left.

2.6.3 Random walk simulation: The general approach consisted of placing a disk ultramicroelectrode with a diameter of $6.0 \mu\text{m}$ at the bottom of a hemispherical volume wherein 200 droplets of $1.0 \mu\text{m}$ in diameter were generated in random locations. The droplets were regarded as points in the simulation domain. The droplet concentration was set at 50 pM by adjusting the hemispherical volume to $6.63 \times 10^3 \mu\text{m}^3$ (Fig. 2.5). We optimized the simulation time to be 5 s so

that the diffusion layer ($\sim\sqrt{6D_d t_{sim}}$) would not outgrow the simulation volume.⁸⁹ Every simulation was performed 500 times while 200 droplets were run sequentially in every simulation.

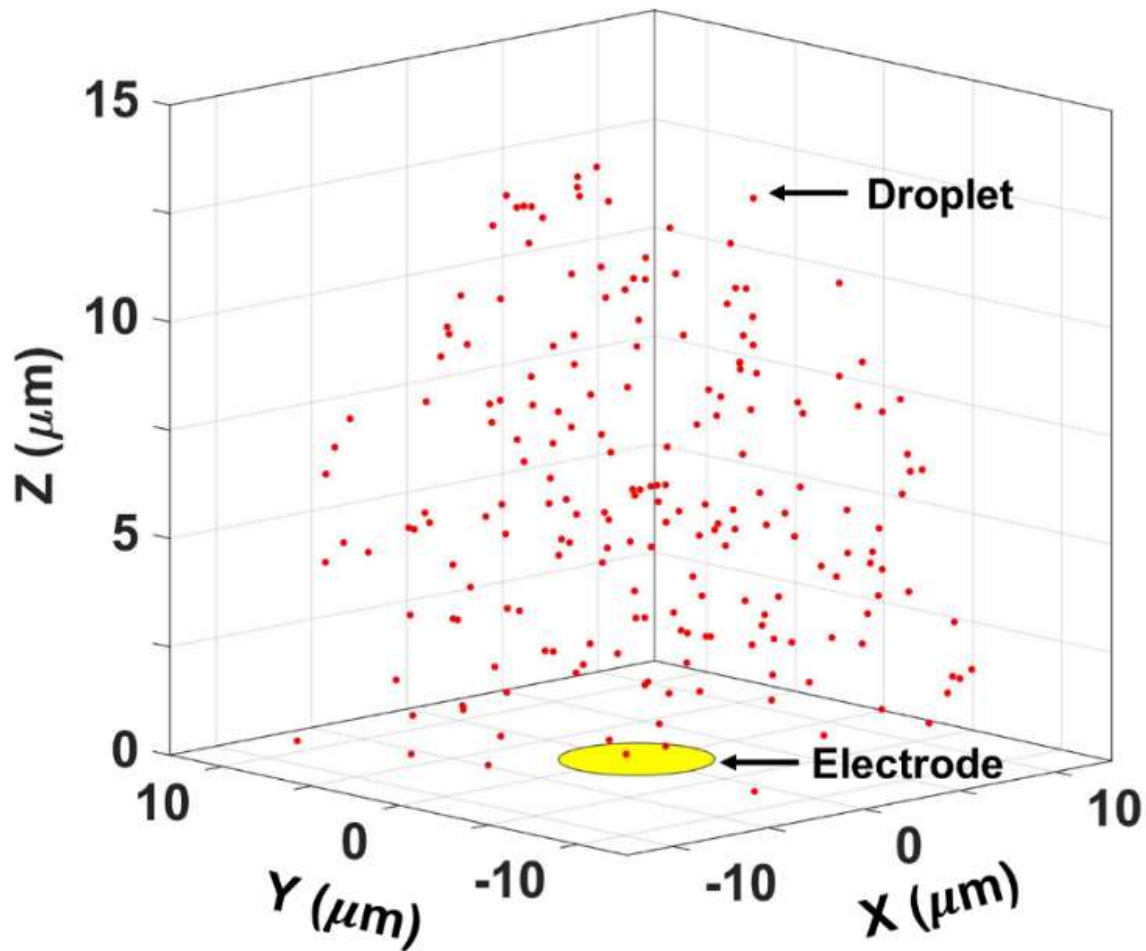


Figure 2.5: Random distribution of 200 droplet particles inside the simulation hemisphere domain (radius $14.69 \mu\text{m}$).

This amounts to a total of 10^5 droplets simulated. A collision was counted whenever the center of the droplet approached the electrode at a distance equal to or lower than the droplet radius. Upon which the droplet was reverted to its previous position to continue the random walk. The same was done when the droplet hit the outer volume boundary. We simulated the droplets moving randomly

in any direction with a predefined step length d and step period t to render a random walk velocity given by:⁸⁹

$$v = \frac{\delta}{\tau} \quad 2.3$$

To determine the values of d and t , we equalized Eq. 2.3 to v_{rms} , also known as the thermal velocity,⁸⁹ which Einstein demonstrated can be estimated with Eq. 2.4 as done for an ideal gas molecule:⁸⁷

$$v_{rms} = \sqrt{\frac{3k_B T}{m_d}} \quad 2.4$$

Irrespective of the medium, the magnitude of v_{rms} is a function of the temperature and the droplet mass (m_d). We determined m_d to be 4.54×10^{-13} g, using the density of toluene, 0.867 g/cm^3 at 298.15 K and the spherical volume of $5.24 \times 10^{-13} \text{ cm}^3$, so that the calculated value of v_{rms} for a 1 μm -toluene droplet is 0.52 cm/s. To fully represent the droplet's random motion in water, v_{rms} has to yield the droplet's diffusion coefficient (D_d) and reflect the latter's dependency on medium viscosity and droplet size. The Stokes-Einstein relationship combines the thermal velocity of the droplet with the Stokes drag coefficient to produce:⁸⁷

$$D_d = \frac{k_B T}{6\pi\eta r_d} \quad 2.5$$

Where η is the viscosity and r_d is the droplet radius. Using the viscosity of water, $8.94 \times 10^{-4} \text{ Pa s}$, at 298.17 K, we calculated D_d to be $4.9 \times 10^{-9} \text{ cm}^2/\text{s}$. Because in 3D-random walks, D_d is also defined as:^{87, 89}

$$D_d = \frac{\delta^2}{6\tau} \quad 2.6$$

By reorganizing Eq. 2.3-2.6 to express d and t in terms of v_{rms} and D_d ,⁸⁹ one gets:

$$\delta = \frac{6D_d}{v_{rms}} \quad 2.7$$

$$\tau = \frac{6D_d}{v_{rms}^2} \quad 2.8$$

Using Eq 2.7-2.8 we obtained $d = 0.57$ nm and $t = 0.11$ μ s directly from properties of the droplet and the medium. In the simulation, t is segmented in a series of steps j , each equal to t seconds, so that $t_{j+t} = t_j + t$. When these steps occur near the electrode they lead to collisions of the same duration (see below). Therefore, a droplet moves 0.57 nm every 0.11 μ s (Fig. A4, Appendix A).

Fig. 2.6 shows the 3D-simulation for a droplet of 1 μ m in diameter with an electrode of 6 μ m. During this journey of 5 s, the droplet completed a total of 4.6×10^7 steps, which include 6680 elastic collisions with the electrode that occurred in several stints. For instance, after wandering freely for 2 s, the droplet collided with the electrode 3076 times for ~ 200 ms, then retreated about 0.7 μ m along the Z axis and came back to collide 764 times for ~ 100 ms. The droplet moved away ~ 0.3 μ m and then collided 2840

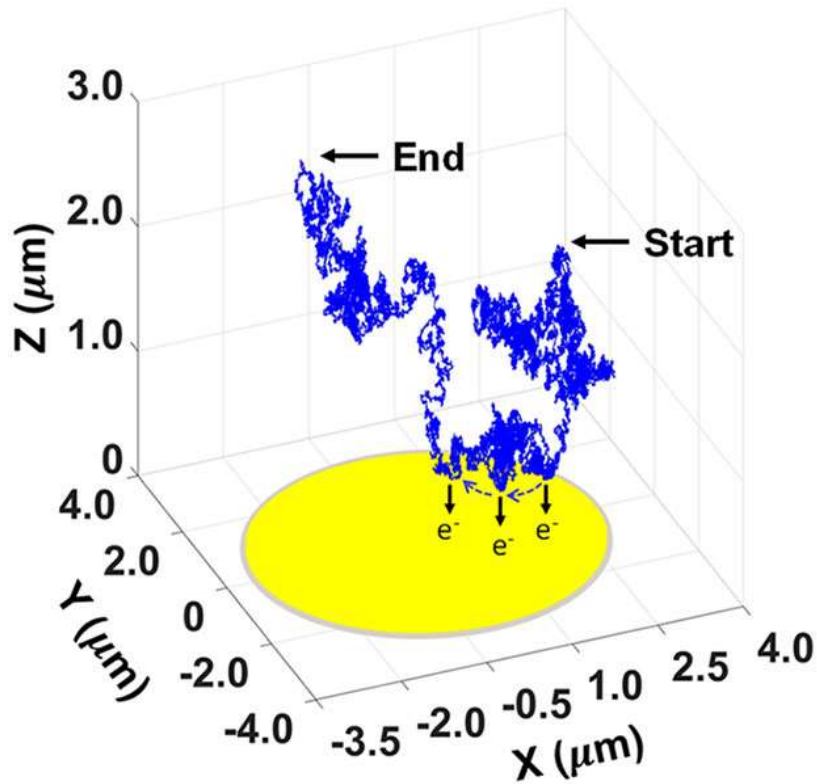


Figure 2.6: Simulated random-walk of 5 s for a droplet of 1 μ m-diameter. The blue trace outlines a trajectory of 4×10^7 steps comprising 3 collisional periods of electron transfer with an UME of 6 μ m in diameter (yellow).

times one last time for ~250 ms before going into the bulk for the remaining of the walk. Fig. 2.7 shows the collision locations on the electrode surface for this droplet.

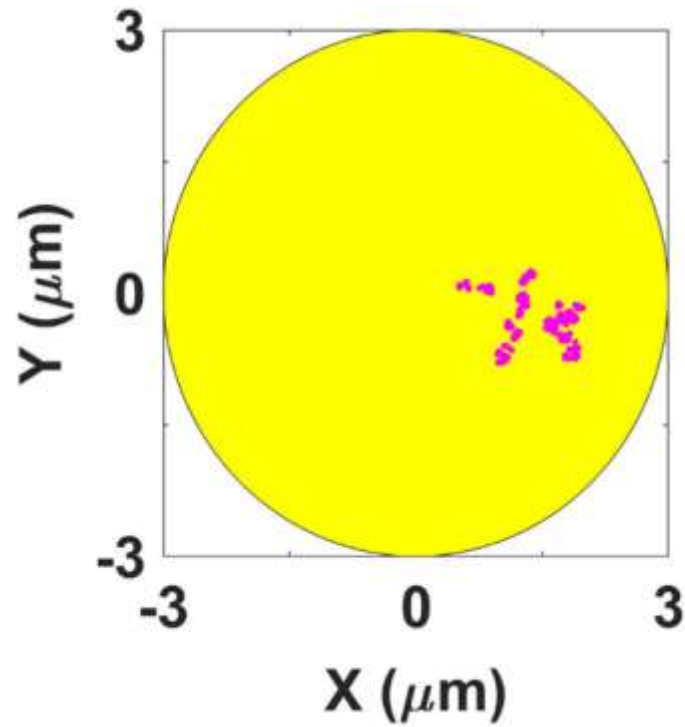


Figure 2.7: Collision locations of the droplet (magenta dots) on the electrode surface (yellow).

2.6.4 Droplet Electrolysis: To simulate droplet electrolysis, we assumed that ET occurs only through a droplet-electrode contact that is formed during t seconds and follows a bulk electrolysis model.⁹⁶⁻⁹⁸ To maintain electroneutrality during oxidation of Fc to Fc⁺, the latter is transferred from the droplet to the aqueous phase, or a counterion enters the droplet.^{19, 98} The area of contact is taken as a circle with an effective radius, r_{eff} ,⁹⁶⁻⁹⁸ which is estimated using the equation for current $i(t)$ at a UME of radius r_{eff} .^{1, 96-98}

$$r_{eff} = \frac{i(t)}{4nFD_{Fc}C_{Fc}(t)} \quad 2.9$$

In this case $i(t)$ is replaced by the current value of peaks selected from $i - t$ traces in Fig. 2.5. To correct for polydispersity, we fitted a plot of calculated values of r_{eff} and droplet diameters d_d from Eq. 2.1 to an exponential equation (Fig. A5, Appendix A). We employed the fitted expression (Eq. 2.10) to compute the average $\langle r_{eff} \rangle$, which for a droplet of $d_d = 1 \mu\text{m}$, turned out to be 1 nm.

$$\langle r_{eff} \rangle = 0.0378 e^{0.0033 d_d} \quad 2.10$$

The $i - t$ bulk electrolysis model for Fc oxidizing under diffusion control inside a droplet during a collision j that lasts t seconds is given by:^{1, 96-98}

$$i(t_j) = i_p e^{-\left(\frac{4D_{Fc}r_{eff}}{V_d}\right)t} \quad 2.11$$

where $i(t_j)$ is the current at any time during collision j , i_p is the peak current at the beginning of collision j ($t_j = 0$), D_{Fc} is the diffusion coefficient of Fc in toluene, $r_{eff} = \langle r_{eff} \rangle \approx 1 \text{ nm}$, and V_d is the droplet volume. Because a collision will oxidize Fc in proportion to t , the value of i_p in Eq. 2.11 must be corrected after every collision using an updated concentration. The time profile for concentration in the bulk electrolysis model¹ applied to these droplets is:

$$C_{Fc}(t_j) = C_{Fc}(0)e^{-\left(\frac{4D_{Fc}r_{eff}}{v_d}\right)\tau} \quad 2.12$$

where $C_{Fc}(0)$ is the concentration of Fc in the droplet at the beginning of collision j . The decrease in peak current Δi_p between two consecutive collisions is proportional to ΔC_{Fc} (decrease in C_{Fc}):

$$\Delta i_p = 4nFr_{eff} D_{Fc} \Delta C_{Fc} e^{-\left(\frac{4D_{Fc}r_{eff}}{v_d}\right)\tau} \quad 2.13$$

where we have plugged Eq. 2.12 into Eq. 2.9 to express i_p as $i(t)$ for a UME that has an effective circular area of radius = r_{eff} . To update the peak current of a droplet undergoing j successive collisions with the electrode, Eq. 2.14 was used:

$$i_p(t_j) = i_p(t_{j+\tau}) + \Delta i_p \quad 2.14$$

For every simulation, Eq. 2.11 and 2.12 were used to calculate the concentration and current for the first collision, while Eq. 2.13 and 2.14 were used for subsequent ones. Fig. 2.8A shows the collisional spikes simulated with Eq. 2.11-2.14 for the 5 s-random-walk of a 1 μ m-droplet containing 20 mM of Fc, portrayed in Fig. 2.6. For clarity, only the interval encompassing the collisional periods from 2.0 to 3.2 s are shown. Likewise, the vertical current scale only shows the upper section of the spikes to make conspicuous the gradual exponential decay of the current as collisions proceed. Because the collision time is constant and equal to τ , the current per collision, Q_j/τ , decreases due to consumption of charge (Q) by electrolysis of Fc. Fig. 2.8B illustrates the decline in Fc-concentration simulated with Eq. 2.12 and ΔC_{Fc} as a function of collisions. The graph also overlays in blue, the droplet's trajectory along the z-axis for the full length of the simulation. After 6680 collisions that took place over ~1200 ms, the Fc-concentration decreased from 20.0 to ~19.9 mM. This depletion corresponds to 0.006 pC, which is ~0.58 % of the ~1.01 pC available in the droplet. In fact, our estimation indicates that it would

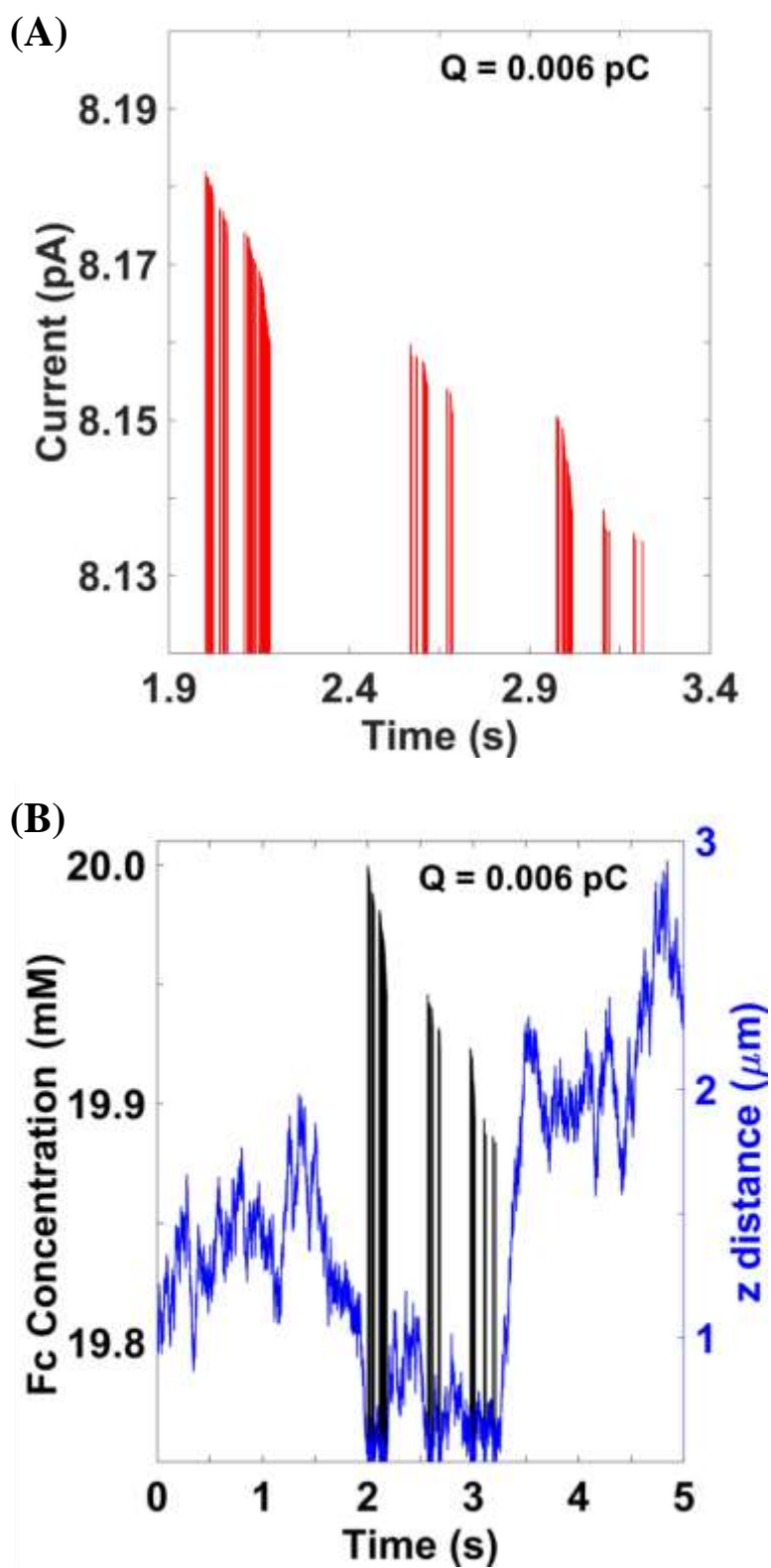
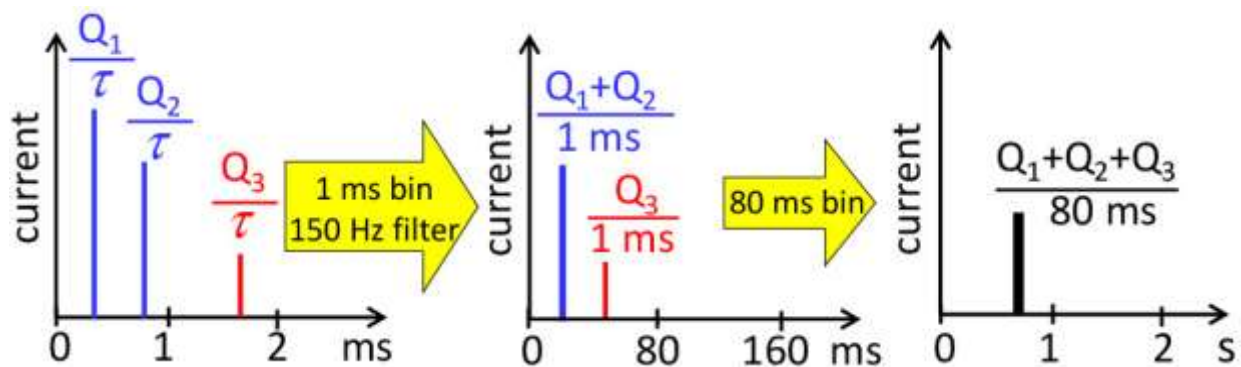


Figure 2.8: A) Simulated $i - t$ collision data for a $1 \mu\text{m}$ -droplet with an electrode of $6 \mu\text{m}$ in diameter. B) Intra-droplet concentration of Fc (black) and droplet distance from electrode (blue).

take $\sim 5.45 \times 10^6$ collisions and ~ 1.26 h to fully electrolyze the Fc in such a droplet (see Appendix B). Though this is raw “unfiltered” data that have not been corrected for acquisition effects (see below), the result stands in opposition to the experimental data in Fig. 2.2, which indicates that most $1 \mu\text{m}$ -droplets loaded with 20 mM Fc, transfer their 1.01 pC, over ~ 400 to 600 ms. This observation is validated by the match between the diameter calculated from electrolysis data (Eq. 2.1) and the one measured with DLS.

2.6.5 Modeling of acquisition parameters: Considering the substantial effect that instrumental filters have on the appearance of electrochemical collision data for NPs,^{99, 109} we simulated the filtering parameters of the potentiostat used in our experiments.⁸⁹ These filters comprise a 2nd-order Bessel low pass filter of 150 Hz and the acquisition frequency of 12.5 Hz (80 ms-sampling interval). Scheme 2.1 illustrates qualitatively the procedure we followed, which begins with a



Scheme 2.1: Binning and filtering of simulated $i - t$ collision data.

series of simulated collisions j , after being converted to current spikes of magnitude Q_j/τ , where $\tau = 0.11 \mu\text{s}$. These spikes were “binned” (grouped) in time segments of 1 ms, while their charge was added to express it as a current value ascribed to a single “bin” of 1 ms. Simultaneously, we applied the 150 Hz-2nd-order Bessel low pass filter available from the simulation software. In experiments, such a filter improves S/N by blocking collateral AC-“signals” from shot, thermal and flicker noise

that have frequencies higher than 150 Hz.¹¹⁰ Finally, we grouped the 1 ms-current bins into larger “bins” of 80 ms to simulate the corresponding 12.5 Hz-acquisition frequency of our potentiostat.

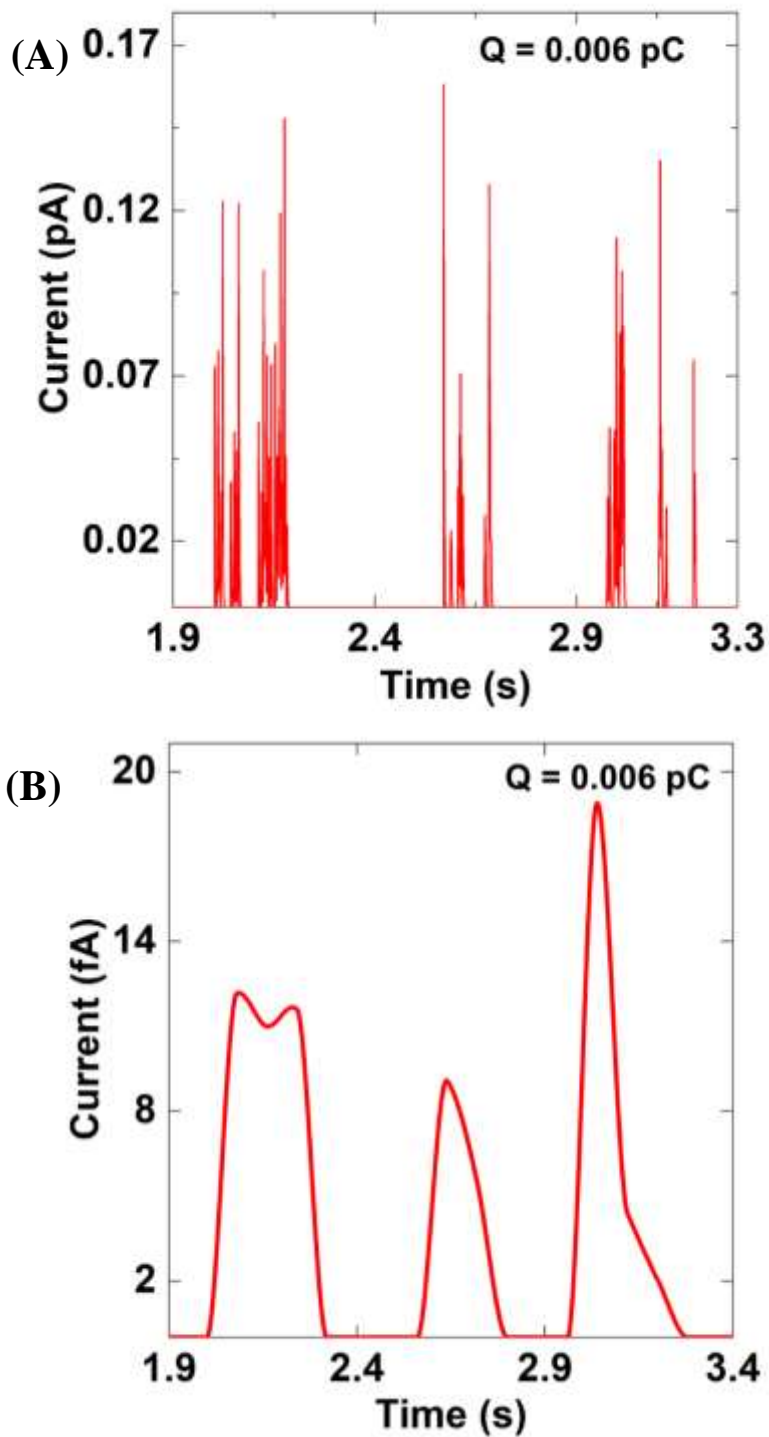


Figure 2.9: Simulated $i - t$ data after filtering A) 1 ms-bin with a 150 Hz-low pass filter followed by B) 80 ms-acquisition sampling intervals.

Fig. 2.9A illustrates the effect of applying a 1 ms bin in tandem with the 150 Hz-low pass filter to the $i - t$ data of Fig. 2.2. The number of spikes drops while the upper bound of current decreases significantly, ~ 8.18 pA when unfiltered (Fig. 2.8A) to ~ 0.16 pA after filtering (Fig. 2.9A). Such an effect is the result of displaying the same charge counted over 1 ms instead of the original interval of $0.11 \mu\text{s}$ (τ). The effect is more dramatic once the bin of 80 ms is introduced (Fig. 2.9B). This causes all spikes to merge into 3 broad peaked signals with duration of ~ 300 to 400 ms and current in the femtoampere level (~ 8 to 20 fA). Though the time intervals match the values observed for the electrolysis of $1\text{-}\mu\text{m}$ droplets observed in Fig 2.2, the currents are one order of magnitude below the peak-to-peak noise (~ 0.2 pA) estimated experimentally. Additionally, the peaks appear distorted (Fig. 2.9B) because the “bins” do not contain enough datapoints from the exponential decay function that makes the current signal.

Given that simulating the oxidation of Fc from droplets colliding elastically did not reproduce the magnitude of currents observed experimentally, even after introducing effects from instrumental filtering, we decided to simulate electrolysis from droplets that adsorb irreversibly on the electrode. To this end, we modified the simulation code to trigger a change in δ , from 0.57 nm to 0 , upon first contact of the droplet with the electrode. While the droplet remained sessile, the simulation continued in successive steps j of the same duration ($\tau = 0.11 \mu\text{s}$) as before adsorption, and until the end of the simulation at 5 s. As done previously, every simulation was run 500 times while 200 droplets were simulated in every run. The droplet adsorption occurred at different times for various runs, but the magnitude and decay function of the current was reproduced every time. Fig. 2.10 shows in blue, the random trajectory of the droplet until first contact with the electrode at ~ 3.3 seconds in the simulation. The concentration of Fc is plotted in black as it is iteratively calculated with Eq. 2.12 for every τ after contact of the droplet with the electrode. The vertical

change of Fc concentration from 0 (no contact) to 20 mM (in contact) in the plot, captures the abrupt nature of the adsorption event. Within ~600 ms of the droplet adsorbing, 99 % of the Fc is oxidized following an exponential decay approaching 0 to transfer ~1.01 pC, which is the charge equivalent to the 10.47 attomol present in the droplet. When this data was converted to current

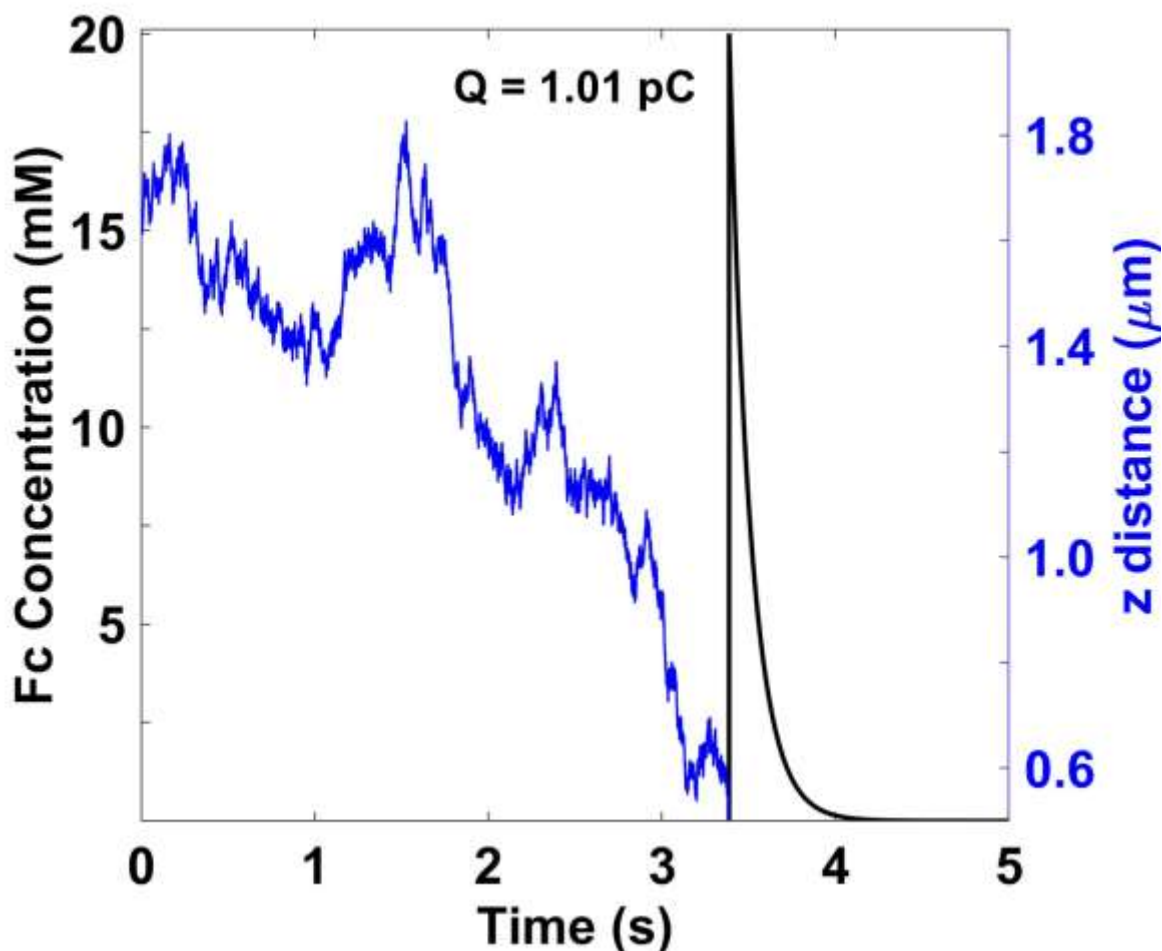


Figure 2.10: Random walk approach until contact with the electrode (blue); change in Fc-concentration (black) upon adsorption.

using Eq. 2.14 and 2.13, a multitude of spikes, each one of duration t (0.11 μ s), and together encompassing ~600 ms, was obtained. The highest spike in the group was 8.2 pA but collectively they decayed exponentially tracking the black trace in Fig. 2.10. Upon applying the 150 Hz-2nd

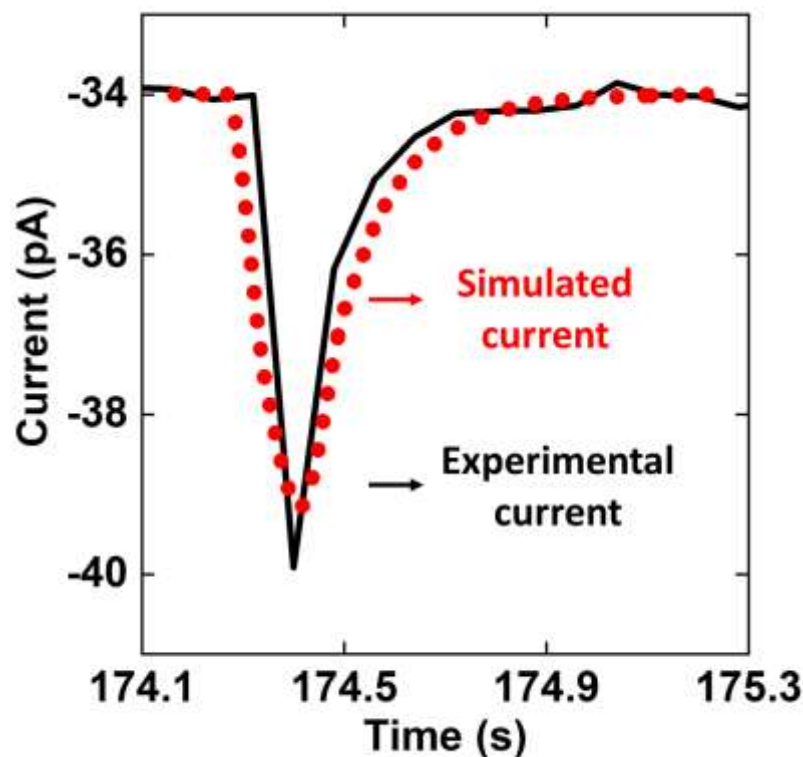


Figure 2.11: Simulated and experimental $i - t$ responses for an adsorbed droplet of $1 \mu\text{m}$ in diameter.

order Bessel low-pass filter and the 80 ms bin described in Scheme 2.1, this multi-spike signal transformed into a peak of $\sim 5.1 \text{ pA}$ and $\sim 600 \text{ ms}$. This is shown in Fig. 2.11 overlaying an experimental peak from Fig. 2.2 that corresponds to a $1 \mu\text{m}$ -droplet. Additionally, when performing simulations using a contact radius of 10 nm instead of 1 nm, the value of current obtained were commensurate to a droplet of $1.3 \mu\text{m}$ instead of $1 \mu\text{m}$ (see Fig. A6 in appendix A), however the time interval and charge did not match (Fig. A7 in Appendix A).

The most consequential insight from this section comes from comparing Fig. 2.8B and 2.11 to contrast the “sensing efficiency” between collisions and irreversible adsorption. Using diffusional collisions, it takes a droplet $\sim 1.2 \text{ s}$ to deliver only $\sim 0.58 \%$ of the available signal (Fig. 2.8B), besides having an extremely low probability (0 out of 10^5 droplets simulated) of ever returning to the electrode during the 5 s of the simulation. Although the droplet started to impact the electrode

at ~2 s, it only had 0.734 ms (6680 x 0.11 μ s) of contact with it, hence merely 0.006 pC of charge was transferred during ~1.2 s. On the contrary, the adsorbed droplet (Fig. 2.10) delivers 99% of the available signal, 1.01 pC, in ~600 ms, which is half the time needed by diffusional collisions. It would take ~1.26 h to deliver the same amount of signal by elastic collisions ($\sim 5.45 \times 10^6$). Therefore, adsorption is an amplification of elastic collisions because 1 adsorption episode can deliver the same number of ET events as ~5.5 million collisions. Moreover, the current from diffusional collisions at short times of $i - t$ recording becomes undetectable because current happens to be an integral of time. For instance, the collisional current from only 5 s of simulation in Fig. 2.9B is two orders of magnitude (~ 20 fA) below the noise level of ~ 0.2 pA!

2.6.6 Butler-Volmer (BV) Analysis: To further evaluate the droplet effective contact area with the electrode, we estimated the experimental current density J , dividing the current measured for a 1 μ m-droplet, by the area at r_{eff} equal to 1 and 10 nm. Then we compared these quantities with the value calculated using the BV expression (J_{BV}) for several reported rate constants¹¹¹⁻¹¹² (k^o) of Fc (Eq. 2.15). Notice that the area in Eq. 2.15 is already factored in, so that closeness to experimental J_{1nm} or J_{10nm} can be determined. Because the Fc-reaction is an oxidation, we only used the anodic side of the BV equation:

$$J_{BV} = Fk^o[-C_{Fc}(0,t)e^{(1-\alpha)f\eta}] \quad 2.15$$

where $F = 96485.33$ C/mol, $k^o = 3.7$ cm/s,¹¹² f is 38.92 V⁻¹ at room temperature, a is the transfer coefficient (0.5), C_{Fc} is 20 mM, and η is the overpotential (0.17 V). The latter was estimated from the potential used in Fig. 2.2 (0.6 V) and $E^o \approx E_{1/2} = 0.43$ V from Fig. A2 (appendix A). By using these experimental values, we incorporate the effect of the ion transfer potential which is required to maintain electroneutrality (see above). The obtained values are $J_{BV} = 195.2$ A/cm², $J_{1nm} = 260.4$ A/cm², and $J_{10nm} = 26.0$ A/cm². Even if using a low (1.9 cm/s) or high (10 cm/s) rate constant for

Fc,¹¹¹ the corresponding J_{BV} -values of 100.2 and 527.5 A/cm² are on the same order of magnitude as the experimental value for $r_{eff} = 1$ nm instead of 10 nm. This demonstrates that a tenfold variation in r_{eff} changes the experimental J by one order of magnitude due to its square relationship with the area, but the same 10-fold change in k^o keeps J within the same order of magnitude close to the value obtained for 1 nm. Therefore, despite the variation in reported values of k^o , the present BV-analysis justifies our assumption of $r_{eff} = 1$ nm.

2.7 Conclusions: Herein, we have investigated the electrochemical response from single toluene microdroplets emulsified in water. By combining experiments with an electrochemical random walk, we were able to extract several key mechanistic insights from single-droplet events. (1) Our model strongly suggests that the electrochemical current peaks observed in $i - t$ recordings at potentials to electrolyze droplet contents, come from single adsorption events instead of diffusional collisions. (2) Adsorption and collision are both driven by diffusion, but the former is an amplification of the latter (*i.e.* an adsorption event is a collision of infinite duration). Hence, the finding that for a 1 μ m-droplet, one adsorption event delivers the same amount of charge as ~5.5 million collisions. (3) Because current is a signal integrated over time, and the collision duration for a droplet is directly proportional to its mass and inversely proportional to its diffusion coefficient, there is a minimum of collisions (or $i - t$ recording time) needed to overcome the noise level. (4) In electrochemistry, diffusion, collision, adsorption, and ET, always occur sequentially but with different time scales and probabilities dependent on intrinsic properties of the particle or molecule. For instance, electrochemical random walks show that for a single ET event to occur, a molecule of Fc requires ~2000 collisions,⁸⁰ and the surface atom of a 1.5 nm-Ag NP needs about 1700 collisions.⁷⁹ We do not expect the inherent kinetics of Fc to change just because is confined in a 1 μ m-droplet, but because the collision frequency of the droplet is lower

than a molecular system, the overall occurrence of ET events will decrease. Consequently, adsorption of a droplet removes the effect of its own collision frequency, thus reverting the dependence of the electrochemical response to the intrinsic kinetics of the molecular system confined in the droplet.

All in all, adsorption is expected to always be advantageous against diffusional collisions, when the signal (*i.e.* sensing, heterogeneous catalysis, etc.) of the species of interest is limited by collisions.⁷⁹⁻⁸⁰ This principle is anticipated to be universal, because from a cancer cell, to a NP, a molecule, and even an electron in a semiconductor, they all follow the laws of diffusion established by Einstein,⁸⁷ albeit with different collision time scales. This investigation is anchored on those laws. Additionally, every microscopic chemical and physical reaction starts with collisions that may turn into adsorption.

Lastly, this study was possible despite droplet polydispersity and the oversimplified adsorption model presented, which ignores the forces involved and subsequent fate of the droplets. All of which, we intend to tackle in future work.

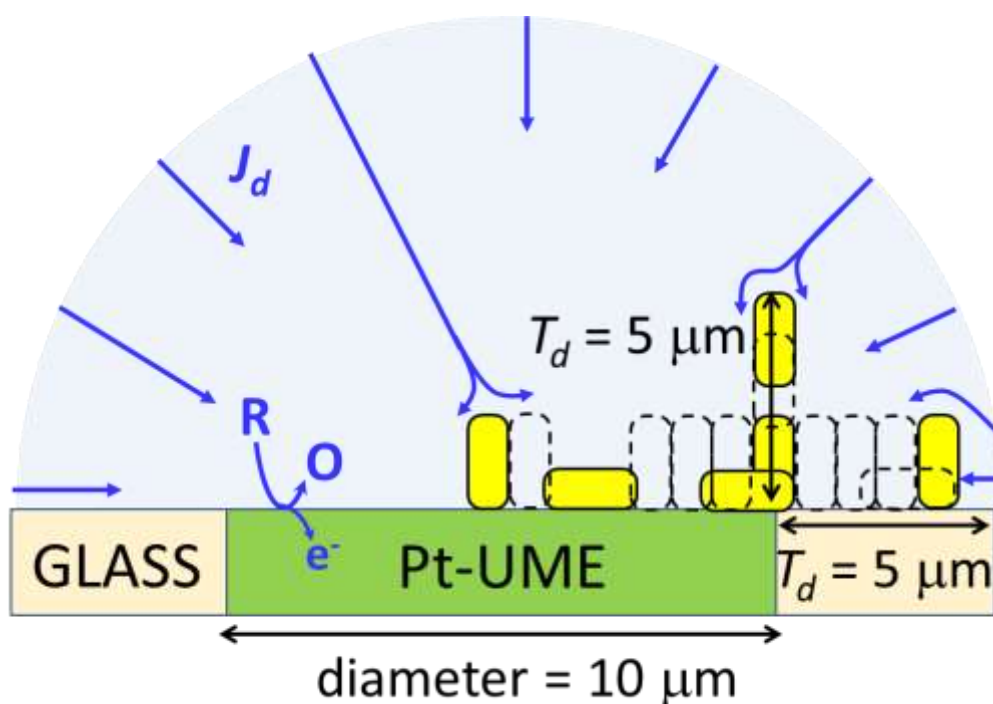
Chapter 3: Distinguishing Bacillus Size, Arrival Velocity, and Landing Orientation from Off-Surface Perturbations of Diffusional Flux in Single-Cell Blocking Electrochemistry

3.1 Abstract: Simulations and experiments of blocking electrochemistry on a Pt-disk ultramicroelectrode (UME) of 10 μm in diameter, reveal differences in size, arrival velocity and landing orientation for three rod-shaped bacteria (bacilli) of varying length. As the oxidation of R to O reaches a steady-state current, bacilli arrive and adsorb on the UME surface blocking both the electron transfer and the diffusional flux (J_d) of R . Adsorption events appear as step currents (Δi) with step-times (Δt) of 1.1 to 0.6 s in correlation to bacillus size and arrival velocity. Bacilli length and orientation were inferred from Δi of the most frequent events, which were assigned to the electrode edge where the electric field and J_d are highest. The simulated current for the pristine UME was subtracted from the current with bacilli located in various locations. The new important result is that when bacilli approach the UME, perturbations of J_d increasingly contribute to Δi until it reaches its maximum value on the UME surface. The threshold distance where these perturbations become detectable from baseline, correlates with bacillus size and encodes a Δt -signature related to arrival velocity. Analysis shows that *B. subtilis* and *E. coli* preferentially land vertically on the UME, while *A. erythreum* favors horizontal landing. Experiments were performed on a sessile droplet of water ($\sim 5 \mu\text{L}$) wetted on the UME surface and immersed in dichloroethane. Scanning electron microscopy corroborates the size determined electrochemically.

3.2 Overview: Single-cell blocking electroanalysis is a type of single-entity approach used to characterize molecular and particulate entities that collide and adsorb on the surface of an ultramicroelectrode (UME) as they partially block an electrochemical reaction (*i.e.* oxidation of R to O or vice versa).^{106-108, 113-115} When holding the potential constant over time (t) to oxidize R at its mass transport limit, the current (i) produced is proportional to the diffusional flux (J_d) of R

(Scheme 3.1) and single adsorption events appear as step currents (Δi) overlaid on the $i - t$ response.¹⁰⁶⁻¹⁰⁸ The frequency of those steps increases with the concentration of the blocking entity and the extent of diffusion, migration, and convection, by which it moves towards the UME surface.^{26, 28, 106-108, 116} In any case, because the electric field is stronger at the edge than at the center of the disk UME,¹⁰⁷ J_d , and arrival frequency are also highest at that location.¹⁰⁸ Consequently, the blocking entity also yields the highest values of Δi at the electrode edge.¹⁰⁶⁻¹⁰⁸ This behavior has been confirmed previously by experiments and simulations of various colliding and adsorbing entities.^{18-30, 106-108, 116-117}

3.3 Background: Ever since the seminal work from Quinn and Lemay,¹⁰⁶ a large variety of



Scheme 3.1: Scheme 1. Threshold distance T_d where perturbations of J_d become detectable from baseline during *B. subtilis* arrival.

microscopic entities have been detected by stochastic blocking electroanalysis, including polymer nanobeads,^{29, 106-108} metal nanoparticles,¹⁸ graphene nanoplatelets,^{27, 30} liquid microdroplets,¹⁹ vesicles,²⁰ and biological targets like viruses,²¹ DNA,¹¹⁷ proteins,¹¹⁷ bacteria,^{22-24, 26, 28} and red

blood cells.²⁵ Properties and effects studied so far include, size,²⁵ shape,²⁷ transport mechanisms,^{26, 106-107, 116} or shroud effects.^{30, 108}

3.4 Novelty and Significance: This chapter describes the investigation bacilli of variable length to reveal relative differences in size, arrival velocity and landing orientation. The novelty of this work stems from demonstrating that during bacillus approach to the UME, off-surface perturbation of J_d contributes to Δi as an observable step-time Δt , that correlates with bacillus size, orientation, and velocity.

Here the experiments and numerical simulations for the electrochemical oxidation of $K_4Fe(CN)_6$ (FCN) on a disk 10 mm-Pt-UME was described, while bacilli of lengths 5, 2 and 1 μm arrive and adsorb on the surface. To model Δi , we subtracted the simulated current at the pristine UME from the current with bacilli at various locations (Scheme 3.1). In addition to adsorption on the UME surface, and by contrast to previous work,¹⁰⁷⁻¹⁰⁸ we systematically simulated perturbations of J_d at increasingly farther distances from the UME edge perpendicularly and parallel to the surface (Scheme 3.1). In both directions, we found a threshold distance T_d , from the electrode edge, where Δi -values become detectable and gradually reach a maximum when the bacillus sits on the edge locus of the UME. The value of T_d shrinks as bacillus size decreases and was found to be $\sim 5 \mu m$ for *B. subtilis* (Scheme 3.1).

Two new important results emerge from this work. First, we were able to ascribe bacillus arrival velocity and size to the step-time Δt of the signal. In this case, Δt is defined as the time interval to reach the full value of Δi as the bacillus approaches the UME and perturbations of J_d increasingly contribute to it. In most previous work, this effect has not evaluated explicitly because the fast velocity of studied particles and the slow experimental sampling interval typically used (50 ms) guaranteed “vertical steps” (*i.e.* $\Delta t \approx 0$).^{107, 117} On the other hand, experiments with optical

tweezers have shown that UME-steady currents decrease with microparticles positioned in solution at distances lower than the UME radius.¹¹⁸ Additionally, the “sudden current drop” or vertical step-time, has been recently connected to size and drift velocity of blocking insulating particles.¹¹⁹ Here, and regardless of using 50 ms as sampling interval, we are able to distinguish differences in size and velocity from variation of Δt for bacteria of similar shape but different length. For instance, *B. subtilis* (~5 μm) yields a Δt of 1.1s, whereas for *A. erythreum* (~1 μm) Δt is just 0.6 s (see below).

The second important result is the inference of bacillus size and the preferential landing orientation by assigning the most frequent value of Δi in $i - t$ curves to adsorption events at UME-edge.¹⁰⁸ To guarantee maximum sensitivity we used high concentration of ferrocyanide (100 mM) as it was done in the size determination of horseradish peroxidase (~1.5 nm) by this same method.¹¹⁷ Independent characterization of bacillus size was done by scanning electron microscopy (SEM), but to estimate size and landing orientation electrochemically, we analyzed and simulated only adsorption events at the electrode edge. The matches that emerged from this analysis indicates that *B. subtilis* and *E. coli*, tend to land with their long axes perpendicular to the UME surface, while *A. erythreum*, prefers horizontal landing.

3.5 Experimental Section

3.5.1 Reagents: All chemicals were reagent grade and used without further purification. Millipore water (18.2 M Ω cm) was used for all electrochemical experiments. 1,2-Dichloroethane (DCE), Tetrabutyl ammonium perchlorate (TBAClO₄), Potassium hexacyanoferrate (II) (K₄Fe(CN)₆, (ferrocyanide or FCN), Sodium Chloride, Potassium Chloride, Sodium phosphate dibasic, Potassium phosphate monobasic were purchased from Sigma-Aldrich (St. Lou-is, MO, USA). Tryptone, Yeast extract were purchased from Fisher Scientific (Waltham, MA, USA). Platinum (Pt) wire was purchased from Advent Research Materials (Eynsham, UK).

3.5.2 Cell culturing: The Luria Bertani (LB) media was prepared by adding 10 grams of Tryptone, 5 grams of yeast extract, and 10 grams of NaCl to 1 L water. Once autoclaving was done for 45 minutes the culture was used to grow bacteria. 100 uL of 50% glycerol stock solution of *Aeromicrobium erythreum*, *Escherichia coli*, and *Bacillus subtilis* were added separately to 10 mL of LB media and grown at 37° C in a shaker. *E. coli* and *B. subtilis* grew overnight, whereas *A. erythreum* needed 3-4 days. Cell growth was monitored by measuring OD₆₀₀ and the stationary phase was used to perform all experiments.

3.5.3 Bacterial cell solutions: 1 mL of each cell culture was centrifuged for 5 minutes at 3000 rpm (*A. erythreum* and *E. coli*) and at 5000 rpm for *B. subtilis*. The growth fluid was removed after centrifugation, and 1 mL of 0.01 mM Phosphate buffer solution (PBS) was added to resuspend the cells. This operation was carried out three times to ensure no media remained. Then the cells were resuspended in 1 mL of 100 mM of FCN solution, that was used as stock and diluted with cell-free solution of FCN to perform the electrochemical experiments. As osmolarity might impact bacterial cell dimension, we ran all our studies within 30 minutes of making the stock solution; otherwise, a fresh stock solution was prepared. Cell concentration was computed from OD₆₀₀ values. These calculations are shown in Table B7.1, Appendix B.

3.5.4 Scanning electron microscopy: Bacterial cells were fixed by adding 1 mL of 3% glutaraldehyde after washing with PBS solution by centrifugation and resuspension. Upon refrigeration for 24 hours to preserve cell morphology, the cells were washed with PBS solution three times. Subsequently, dehydration was carried out by suspending the cells in a series of ethanol-water solutions from 30 to 100 % ethanol. The cells were then drop-casted on cleaned silicon wafers followed by critical point drying. The silicon wafers were then fixed on to conductive carbon tape and coated with gold for SEM imaging. SEM images were recorded with

a Hitachi SU-70 FE-SEM operating at 5kV. Critical point drying was performed in a Autosamdri-931 (Rockville, MD).

3.5.5 Sessile water droplet on electrode: A ~5 μL -droplet of aqueous solution with 100 mM of FCN and bacteria was placed on the electrode surface using a micro-pipette. Then the electrode with the wetted droplet was carefully inserted into a solution of DCE containing 100 mM of TBAClO_4 .

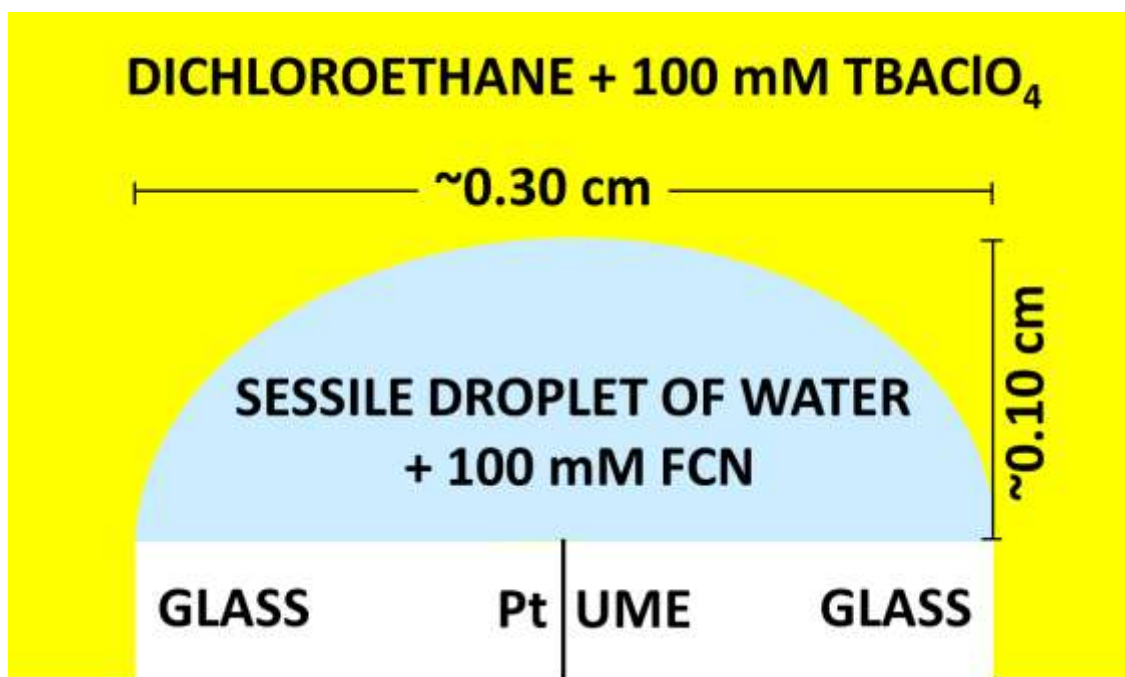
3.5.6 Electrochemical and ζ -potential Instrumentation: All electrochemical experiments were recorded using a CHI 660C instrument (CH Instruments, Austin, TX) in a three-electrode system. A non-aqueous Ag/AgNO_3 (Ag/Ag^+) electrode and a 0.5 mm Platinum wire were used as a reference and counter electrode. The reference and counter electrodes were placed in the DCE solution. All $i - t$ curves were recorded at 50 ms sampling interval and performed at least three times. The experimental noise was estimated to 0.02 nA and the minimum current change counted as step was 0.1 nA. Zeta potentials of the bacilli were recorded using the Zetasizer Nano ZS (Malvern, Westborough, MA) instrument in 0.01 M of FCN solution.

3.5.7 Numerical simulations: 3D-modeling was performed using the Electroanalysis interface (COMSOL, Multiphysics 5.6) by solving the Nernst-Planck equation in a hemispherical geometry under diffusional conditions. This hemispherical geometry consisted of an inner and outer domain with radius 200 and 500 μm respectively. The inner domain was configured with smaller mesh size than the outer domain. The 10 μm -diameter electrode was generated at the center of the hemispherical geometry. A no flux boundary condition was selected for simulating the insulating glass surface surrounding the electrode, and the bacillus volume. The potential was set to 0.4 V vs. reference potential. Oxidation of FCN at the electrode surface was selected using the electrode reaction node. The simulation was started with 100 mM of FCN through the whole domain. The

minimum mesh size for the electrode was 10 nm, and the growth rate was 1.1. A plane of symmetry was used to cut the total simulation domain into two halves to reduce run time. The ferrocyanide diffusion coefficient entered in the simulation was $6.7 \times 10^{-6} \text{ cm}^2/\text{s}$. The COMSOLTM report for the disk UME is in appendix C.

3.6 Results and Discussion

3.6.1 Bacillus blocking in a sessile droplet of water: We performed the experiments inside a water droplet ($\sim 5 \mu\text{L}$) carefully placed on the surface of the UME and then immersed it in a solution of DCE containing 100 mM of TBAClO₄. During the experiment, the water droplet with 100 mM of FCN was kept in place by spontaneous wetting and hydrophobic forces (Scheme 3.2). The motivation for employing this configuration was to use the DCE phase as delivery of chemical



Scheme 3.2: UME-set up with reference and counter electrodes in the dichloroethane (DCE) phase.

stimuli for bacteria to respond to and be detected electrochemically in the aqueous phase. However, this work focuses on characterizing this platform for detecting perturbations in the diffusional flux

of FCN (J_d) caused by bacillus arrival to the UME surface. Fig. 3.1 shows the $i - t$ traces recorded for *Aeromicrobium erythreum* (AE), *Escherichia coli* (EC), and *Bacillus subtilis* (BC), while the

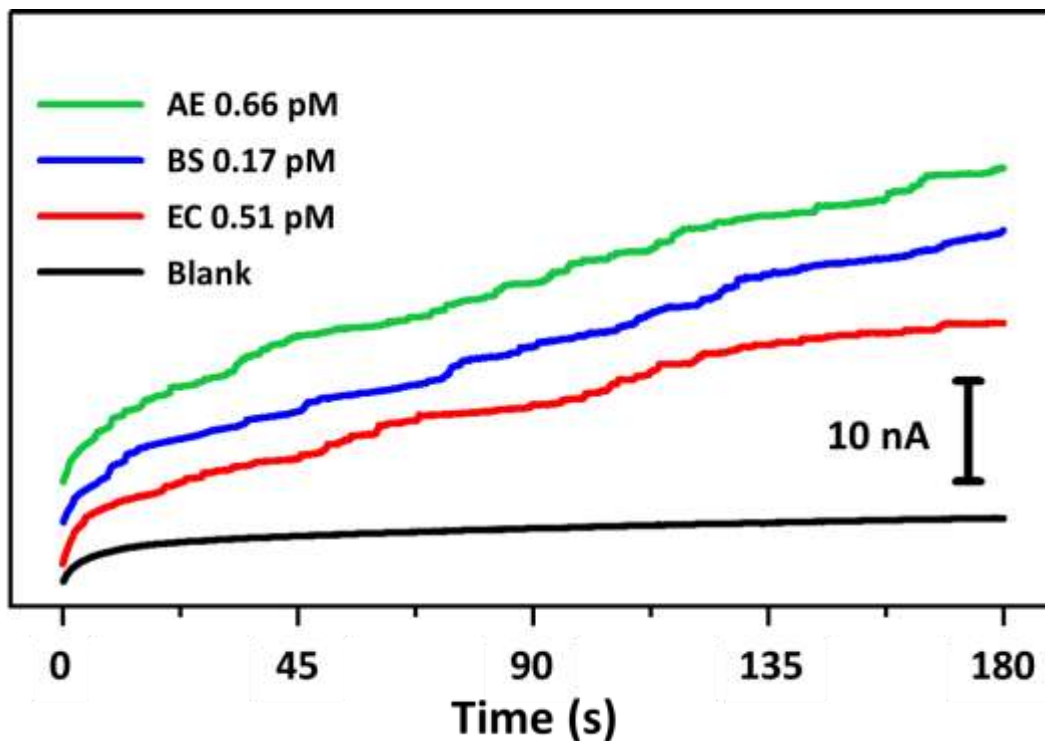


Figure 3.1: $i - t$ curves for bacilli adsorption at a sessile droplet of water with 100 mM FCN and 100 mM TBAClO₄ in the DCE phase; Pt-UME, 10 mm diameter, at 0.4 V vs. Ag/Ag⁺.

potential was kept at 0.4 V vs. Ag/Ag⁺ outside the droplet. In contrast to the blank trace without bacteria, the bacilli $i - t$ curves show single adsorption events as tiny steps of decreasing negative current, that reflect individual blockages of electron transfer for the oxidation of FCN.

Given that the sessile droplet of water does not contain supporting electrolyte, to assess the effect of FCN migration in the electrochemical response, we recorded the cyclic voltammogram (CV) for a sessile droplet without bacteria. The CV has a sigmoidal shape with a limiting current of ~134.4 nA and a current onset at about 0.05 V (Fig. 3.2). Despite the high concentration of redox species in the water droplet,¹²⁰ and TBAClO₄ transferring from the DCE phase, the transport of FCN within the sessile droplet appears to be dominated by diffusion with migration being

undetected. The diffusion coefficient, D_{FCN} , estimated from the CV in Fig. 3.1, is $6.94 \times 10^{-6} \text{ cm}^2/\text{s}$, which is pretty close to $7.26 \times 10^{-6} \text{ cm}^2/\text{s}$ determined with a micrometer-type thin layer cell,¹²¹ or $6.5 \times 10^{-6} \text{ cm}^2/\text{s}$ in bulk cell with 0.1 M of KCl.¹ A simulation of a step potential for 100 mM FCN with a UME of 10 μm in diameter, produced a steady state current of $\sim 137.8 \text{ nA}$ (Fig. A8,

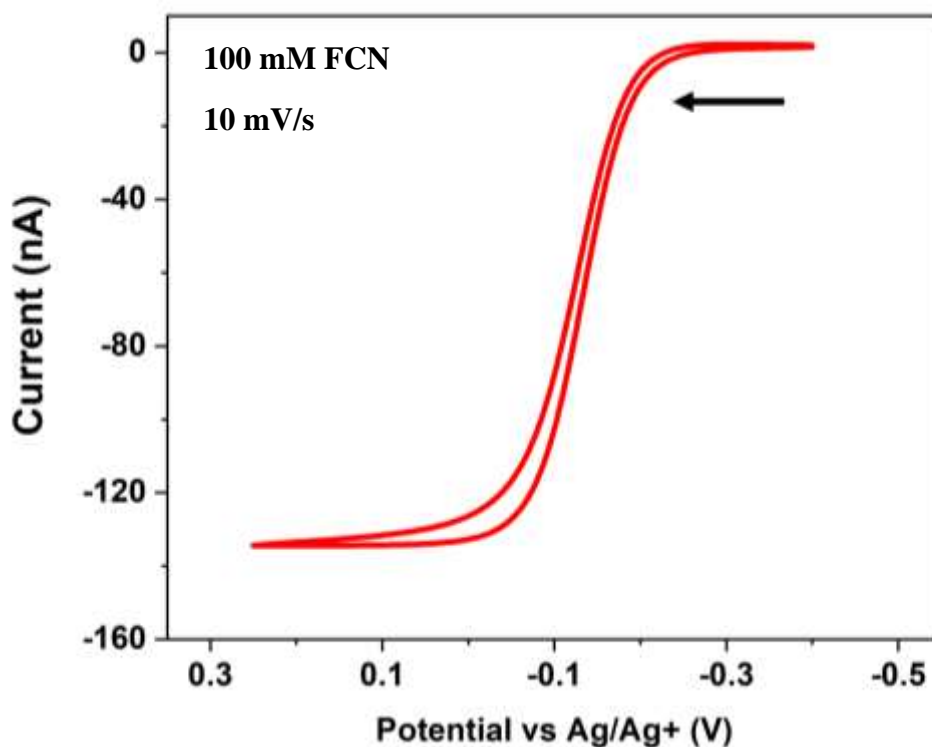


Figure 3.2: Sessile droplet CV of FCN on 10 μm Platinum electrode surrounded by 2 mL of 100 mM TBAClO₄ Dichloroethane solution. No supporting electrolyte was added inside the sessile droplet.

Appendix A). On the other hand, complete electrolysis of the FCN trapped in the aqueous droplet is not feasible because the diffusion layer, $\delta = (2Dt)^{0.5}$, grows $\sim 0.05 \text{ cm}$ during the 180 s of the experiment (Scheme 3.2).

To analyze the data in Fig. 3.1, we counted the steps in each $i - t$ trace and excluded any signal with value of Δi below 0.1 nA (5 times the noise average). Figure 3.3 shows histograms of Δi -values collected from each bacillus trace and expressed in percentage: AC (green), BS (blue), and EC (red). Every distribution in Fig. 3.3 has a maximum percentage of Δi -values that we attribute

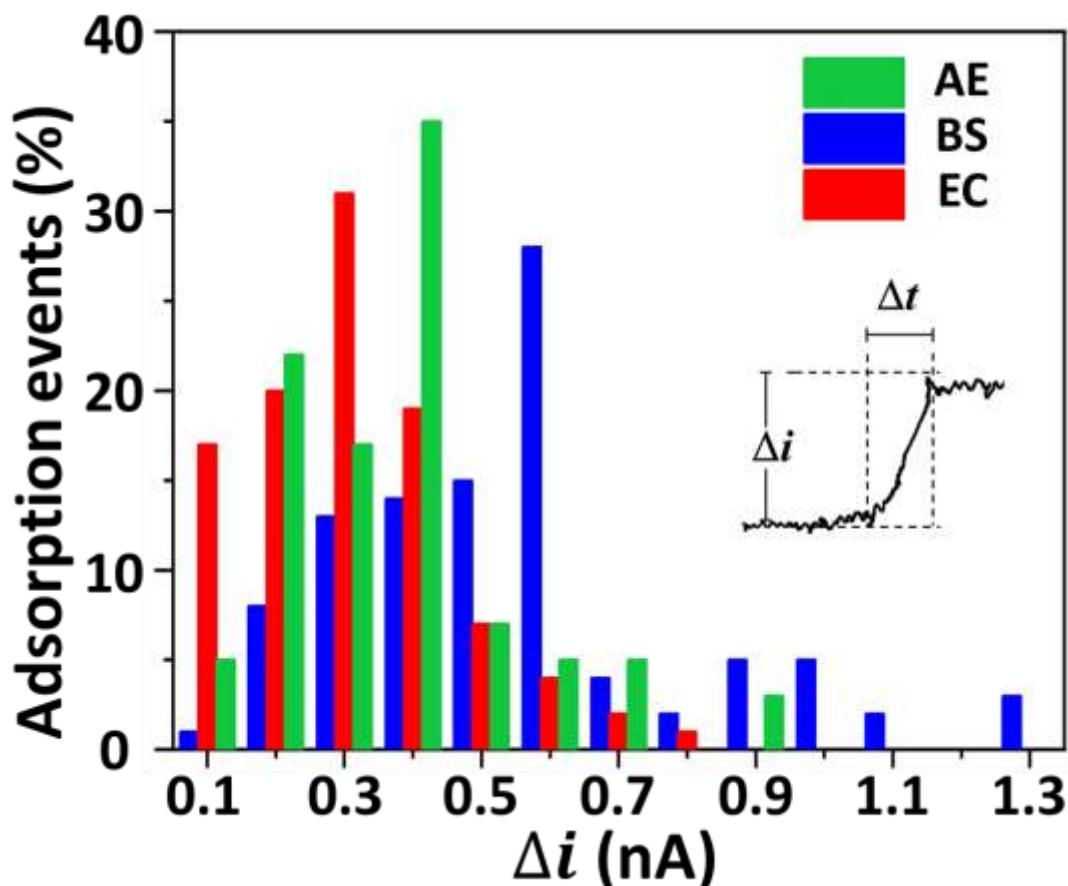


Figure 3.3: Δi -distribution for bacilli in sessile droplet of water 100 mM FCN immersed in DCE phase with 100 mM TBAClO₄. Inset: Δi and Δt measured for each step analyzed in Table 3.1.

to edge events. Such assignment is congruent with previous simulations and optical tracking experiments,¹⁰⁸ which demonstrated that the most frequent landings happen at the electrode edge,¹⁰⁸ as a result of the electric field being non-uniform,¹ and displaying a maximum at that location.¹⁰⁷ Consequently, the greatest migration pull and highest diffusional flux, J_d for FCN, also

occur at the electrode edge.¹⁰⁶⁻¹⁰⁸ Fig. A9 in Appendix A shows a simulation of J_d with the highest magnitude at the electrode edge and sharp decrease towards the center.¹⁰⁷⁻¹⁰⁸

The values of Δi above and below the maxima of the distributions in Fig. 3.3 (35% AE, 31% EC, 29% BS) embody the intrinsic polydispersity of the bacilli (see below) mixed with some contribution from events on the edge and likely on both sides of it. This conjecture is based on three observations: first, the frequency of bacillus impacts decreases by ~30-34% when comparing the first and last 60 s of each $i - t$ run. (Table B8, Appendix B). Reductions of ~50 % in collision frequency during runs of 600 s have been observed by fluorescence microscopy as particles start landing near the center and shroud, where impact frequency falls down.¹⁰⁸ Second, the average number of landings during our experiments (180 s) was lower than 50% of a full monolayer estimated for a 10 μm -UME, *i.e.* 14% for BS, 19% for EC, and 41% for AE, (Table B9, Appendix B). Third, polydispersity of bacillus length is typically broad and depends on factors like cell density, cell cycle and culture conditions.¹²² For instance, the reported length distribution for *E. coli*¹²³ overlaps significantly with *A. erythreum* because they are close in size.¹²⁴ Even the large *B. subtilis*, has a length distribution that extends over the distributions for *E. coli* and *A. erytherum*.¹²⁵ Fig. A10 (Appendix A) is the SEM image illustrating this size variability, which also includes the nominal length accepted for each bacterium, ~1 μm for AE,¹²⁴ ~ 2 μm for EC,¹²³ and ~5 μm for BS.¹²⁵ Therefore, it is reasonable to assign the majority of events in Fig. 3.2 to the UME-edge along with some landings near the center or on the shroud of the electrode,¹⁰⁸ so that the distributions in Fig. 3.3 actually reflect the broad range of lengths typically found in bacteria.¹²²

Table 3.1. Most frequent values of Δi for bacillus distributions in Fig. 3.1.

Cell	Nominal length (μm)	Δi (nA)*	Δt (s)	n
AE	~1 (ref. 124)	0.4	0.6 ± 0.3	19
EC	~2 (ref. 123)	0.3	0.6 ± 0.2	14
BS	~5 (ref.125)	0.6	1.1 ± 0.3	6

*The standard deviation was the average noise level recorded for a i - t curve without bacteria and was equal to 0.02 nA

Table 3.1 summarizes the number (n) of values Δi and Δt grouped in the most frequent bin of the distributions for each bacillus in Fig. 3.1. This Table 3.1 also lists values of Δt , which is defined as the time needed to reach the maximum magnitude of Δi and we propose to originate from perturbations of J_d during bacillus approach to the UME surface (see below). These perturbations have been detected in simulations of electrochemical blocking by nano¹⁰⁷ and microbeads¹⁰⁸ as well as experiments with optical tweezers.¹¹⁸ The latter show that the steady state currents of an UME decreases when an insulating microparticle is positioned in solution at distances lower than the UME radius.¹¹⁸ As shown in Table 3.1, the Δt increases with bacillus size, which means that when approaching the electrode, a large cell perturbs the diffusional flux earlier in time (or at a farther distance from the UME) than a small bacillus (see below). For instance, AE has a Δt of 0.6 s, whereas for BS, Δt is 1.1 s. In this way, Δt is the time that the bacillus takes to block the steady current and produce Δi (inset Fig. 3.3) as it approaches the UME. So, the distance traveled during Δt is a threshold distance, T_d , where the perturbation to J_d becomes detectable from the baseline of steady state current.

3.6.2 Simulation of Δi , Δt and T_d : The modeling was done in 3-D so that volume effects on the flux could be accounted for (see Experimental Section and Appendix C). The Nernst-Planck equation was solved in diffusional mode given that the conditions the redox flux in the sessile droplet is dominated by diffusion ($J = J_d$). The Δi was simulated in two stages: in the first one,

steady-state current i_{ss} was calculated and compared to the analytical expression (Eq. 3.1) for a disk UME of 10 μm in diameter:¹

$$i_{ss} = 4nFD_{FCN}C_{FCN}^*r_e \quad 3.1$$

where n is the number of electrons in the reaction, F is the Faraday constant, D_{FCN} is the diffusion coefficient for FCN, C_{FCN}^* is the bulk concentration of FCN and r_e is the radius of the UME. In the second stage, we simulated i_{ss} assuming the presence of the insulating bacillus on the UME surface (the J_d boundary condition of the simulation was set to zero for the insulating region representing the location of the bacillus). The calculation of Δi was done by computing the difference in i_{ss} between stage one and two.¹⁰⁷

Fig. A8 (Appendix A) shows the simulated current i_{ss} for 100 mM FCN under a potential step of 0.4 V lasting 2 s. The resulting magnitude of i_{ss} , which follows the expected time profile,¹ was taken at 2 s, and was also found to be very close to the value obtained in the CV experiment (Fig. 3.2).

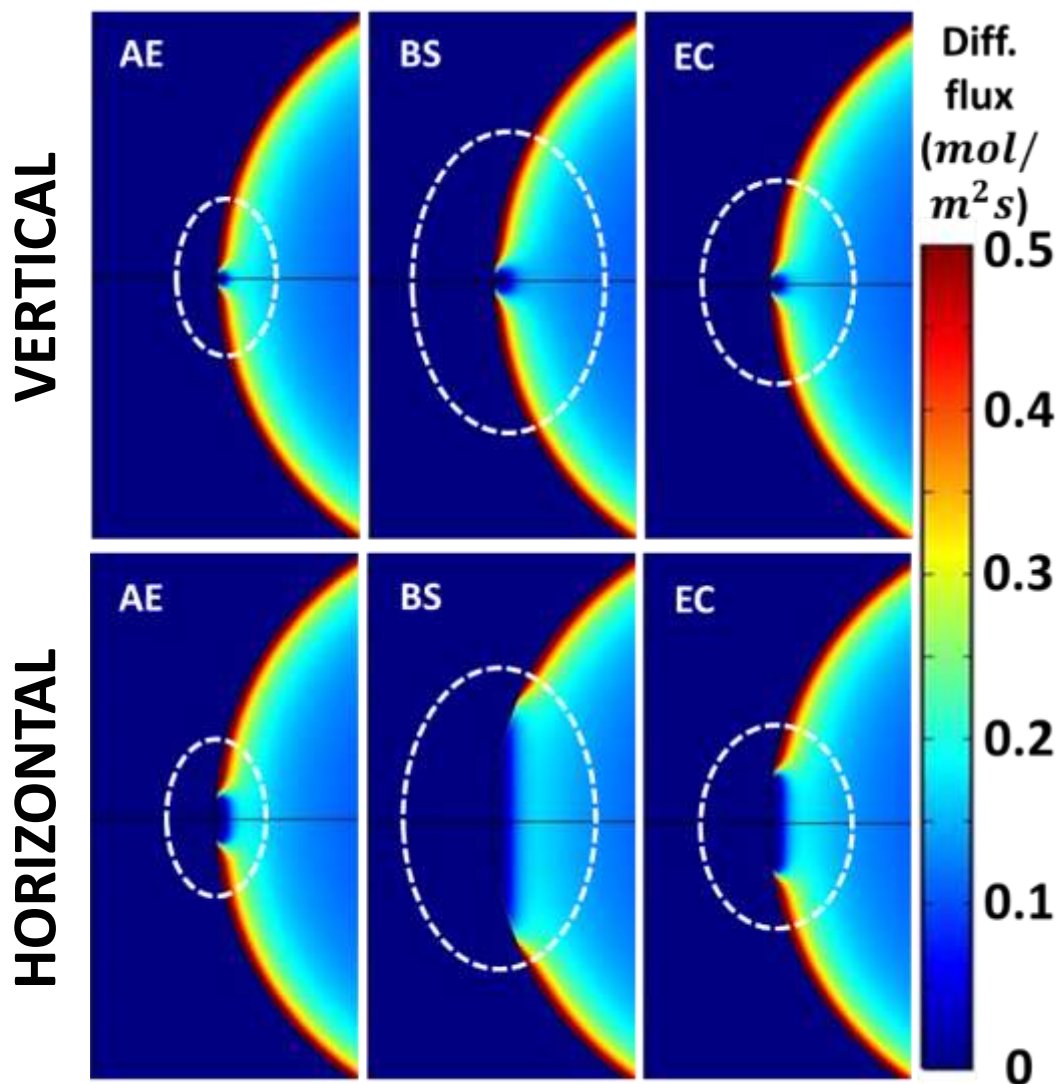


Figure 3.4: Simulation of blocking at the UME-edge due to bacteria adsorption.

Fig. 3.4 shows the top view of simulation snapshots for the three bacilli located at the UME-edge in vertical and horizontal orientation. The color gradient in the figure indicates how the blocking of both electron transfer and J_d ($\text{mol}/\text{m}^2 \text{ s}$) nullify the flux at the adsorption site. Everywhere else on the edge the magnitude of J_d is maximum and decreases to about 10% at the UME-center (Fig. A9, Appendix A). As expected, the calculated Δi is larger for the bacillus adsorbed horizontally than when is in vertical position. This is a consequence of the rectangular projected area in horizontal position being larger than the circular area in vertical orientation.

Figure 3.5 summarizes the values of Δi as a function of distance from the UME-center for the bacilli adsorbed on the surface including the shroud region.

Fig. 3.5A shows the data simulated with vertical orientation while Fig. 3.5B shows the horizontal one. In both cases, the maximum magnitude of Δi occurs at the edge locus (5 μm) and decreases on both sides of the boundary. At every distance from the UME center including the shroud, the values of Δi scale down with the size of the bacillus. For BS and EC, the match with the experimental Δi -values plotted in Fig. 3.2A (most frequent event), corresponds to 0.6 and 0.3 nA, respectively, which are for vertical orientation. By the same token, for AE, the experimental Δi -value of 0.4 nA in Fig. 2A, only matches the horizontal orientation in Fig. 4B. This difference in orientation may be rooted in the lack of autonomous motility for AE,¹²⁴ which is present in the other two bacilli.¹²⁶⁻¹²⁷

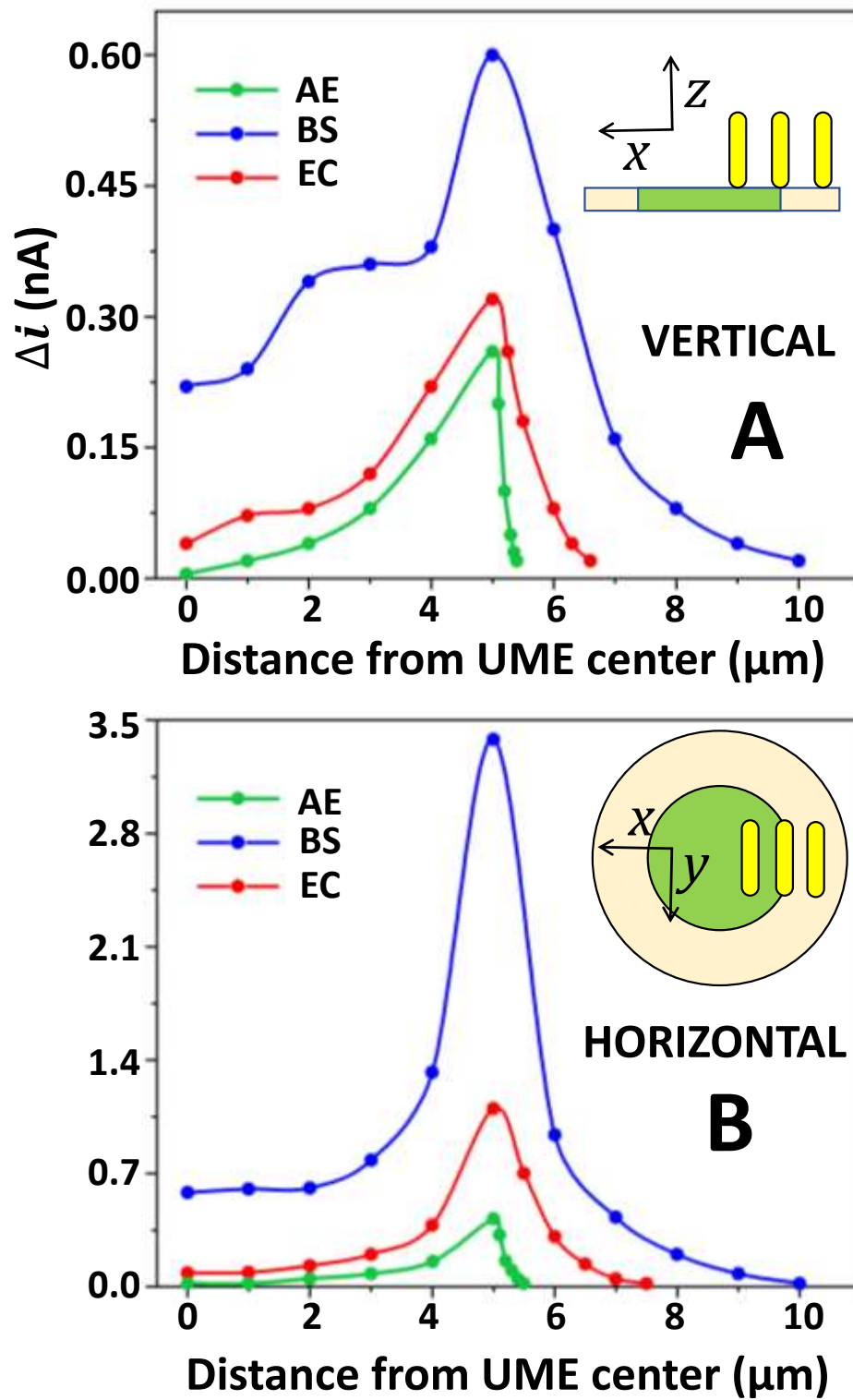
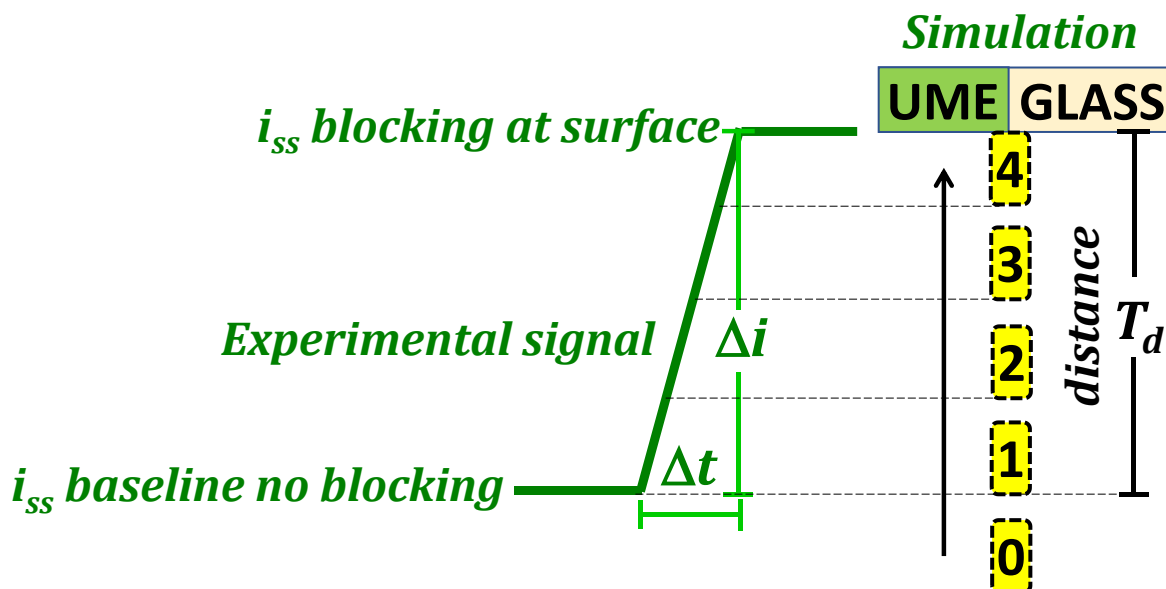


Figure 3.5: Simulated Δi for bacilli adsorption on a 10 μm -diameter UME including the shroud surface. A) Vertical, B) Horizontal adsorption orientation

To simulate Δt in the Δi -signal, the bacillus arrival to the UME surface is discretized in distance steps that represent time steps in the experimental signal (Scheme 3.3). In this model, the signal



Scheme 3.3: Simulation of bacillus arrival in steps of increasing degree of blocking from a threshold distance T_d .

Δi grows from zero to its maximum value on the surface as the bacillus approaches following the arrow in Scheme 3.3. Starting with the bacillus at location 4 on the surface (Scheme 3.3), the steady-state current, i_{ss} , was simulated at increasingly farther distances perpendicular to the surface on the edge locus, until the value of i_{ss} matched the baseline current in absence of bacillus. The latter is equal to i_{ss} at location 0 in Scheme 3.3, where the bacillus is farther than the threshold distance T_d and has null effect on perturbing J_d . Therefore, every time point in the experimental Δi -trace is related to a value of i_{ss} that is proportional to the degree of blocking (J_d and/or electron transfer) and can be simulated at certain distance (Scheme 3.3). The value of Δi_n for each location in Scheme 3.3 can be calculated with Eq. 3.2 while Δi becomes the sum of all those steps (Eq. 3.3), which is the same as the difference between i_{ss0} and i_{ss4} , as explained in the previous section.

$$\Delta i_n = i_{ss(n-1)} - i_{ss(n)} \quad 3.2$$

$$\Delta i = \sum_{n=1}^4 \Delta i_n \quad 3.3$$

For the vertical orientation in Fig. 3.5A, the values of Δi between 2 and 4 μm of the UME center appear as a shoulder for BS (largest bacillus) and dissipates significantly for EC (second largest). In AE this feature is no longer present and is not observed either in horizontal configuration. This effect is attributed to the way the rod shape interacts with J_d along the z -axis away from the UME surface (Fig. A11, Appendix A). The flux is a result of the gradient of concentric iso-concentration lines that conform to the hemispherical shape of the flux (Fig. A11, Appendix A). It turns out there is a distortion of the iso-concentration lines when disrupted by the one end of the bacillus, so that the distance between two iso-concentration lines along the vertical z -axis ($\partial C_{FCN}/\partial z$) becomes different on both sides of the rod (Fig. A11, Appendix A). The ratio $\partial C_{FCN}/\partial z$ on the side near the UME center appears larger than on the opposite side of the bacillus. Given that $\partial C_{FCN}/\partial z$ is related to J_d and i through Eq. 3.4,¹ this explains the increased values of Δi for BS in Fig. 3.5A near the UME center.

$$\frac{i}{nFA} = J_d = D_{FCN} \left(\frac{\partial C_{FCN}}{\partial z} \right)_{z=0} \quad 3.4$$

The critical parameter to simulate Δt is the threshold distance T_d , which we define as the location perpendicular to the UME edge, where perturbation of J_d becomes zero. This parameter was first simulated by Boika, Thorgaard, and Bard,¹⁶ in their seminal work characterizing blocking electrochemistry of sub-micrometer spherical beads. They concluded that their particles were moving by electromigration instead of diffusion because the latter would take too long to travel the simulated distance T_d and replicate the experimental “vertical Δi -steps” ($\Delta t \approx 0$). Here their idea was expanded by using T_d to simulate the time response of experimental blocking signals and demonstrate that the bacillus size and orientation are encoded in the Δt part of the signal.

Nevertheless, this result is only possible because the cells in this study are slow enough to produce discernable Δt slopes in their Δi -signals.

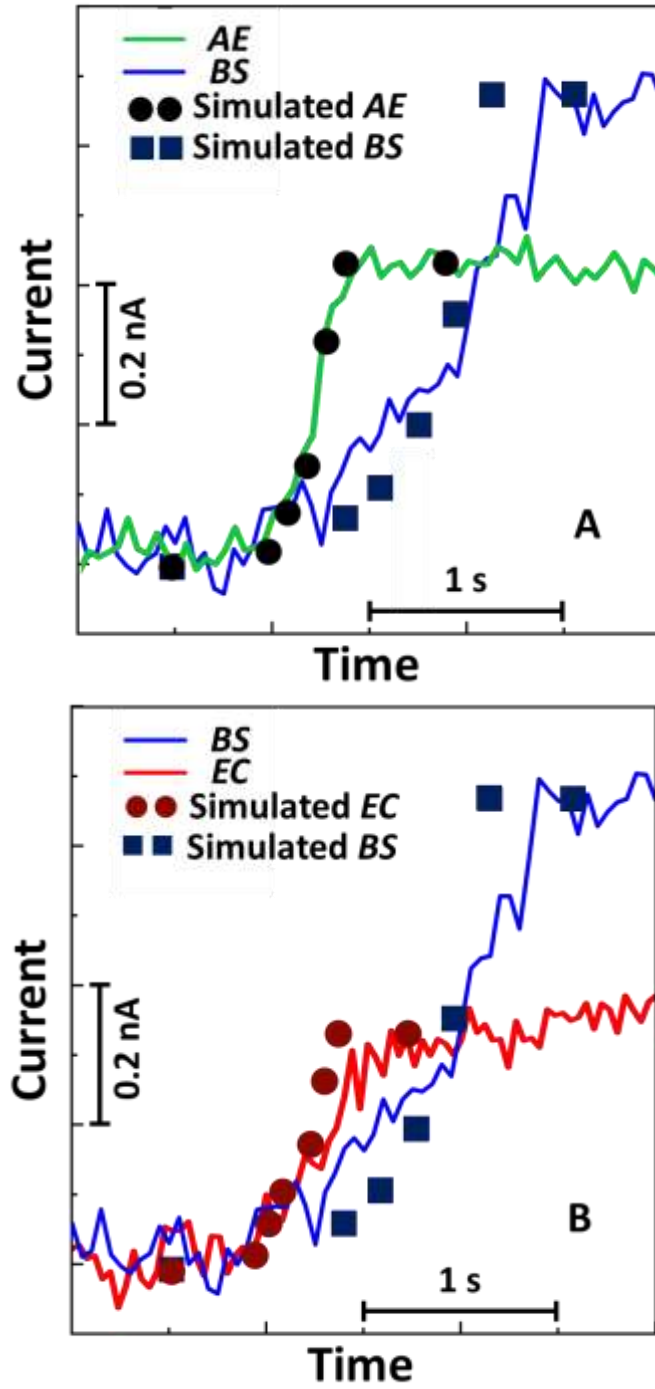


Figure 3.6: Δi -traces for bacilli blocking in conditions of Fig. 3.1 overlapped with simulated Δi

Figure 3.6 shows the experimental (lines) and simulated (circles and squares) traces for Δi in the same conditions of Fig. 3.1. The traces are displayed in pairs (Fig. 3.6A and 3.6B) for easy contrast between the large (BS) and small (EC and AE) bacilli. Figure 3.7 summarizes the trend for perturbations of J_d along the z direction for both landing orientations. The value of T_d scales up with the length of the bacillus according to the sequence, 0.4, 1.7 and 5 μm , for AE, EC, and BS, respectively. These values are for the landing orientations that match the data in Fig. 3.2, that is, vertical for EC and BS, and horizontal for AE. In general, the T_d -values are slightly higher for horizontal landing than for vertical (Fig. 6A and 6B). So, the difference between both orientation is in the way Δi approaches its maximum value. For instance, vertical landing leads to a more gradual increase of the Δi -signal than horizontal orientation. This is because the long axis of the bacillus can disrupt concentric iso-concentration lines more effectively than the short axis (Fig. A9, Appendix A). As explained above, the magnitude of Δi at the UME surface increases with the projected area that blocks electron transfer, so the horizontal landing has always higher Δi -value than vertical.

The estimated arrival speeds that result from dividing T_d over the average experimental value of Δt from Table 3.1 are: 0.67, 2.83, and 4.54 $\mu\text{m/s}$, for AE, EC, and BS, respectively. These velocities indicate that BS, despite being the largest bacillus of the group, is the fastest, and conversely, AE is the slowest. Such a result might be counterintuitive when looking at the Δi -traces in Fig. 3.6A, because they imply that AE has a faster rise in signal than BS. Though that is true, it is not because AE moves faster than BS, but because by being large, BS can perturb J_d at a farther distance ($\sim 5 \mu\text{m}$) than AE ($\sim 0.4 \mu\text{m}$). The “allocated” time Δt that each bacillus has for traveling the T_d distance, is what renders their corresponding speeds. It is easy to see then, that both Δt and T_d are primarily determined by the size of the particle, but also influenced by the

magnitude of J_d and the radius of the electrode. Therefore, the trend of increasing arrival velocity in proportion to the size of the bacillus, is what is expected when electromigration dominates over diffusion,¹¹³⁻¹¹⁴ and has been reported before for electrochemical blocking with some of these bacteria.²²⁻²⁴

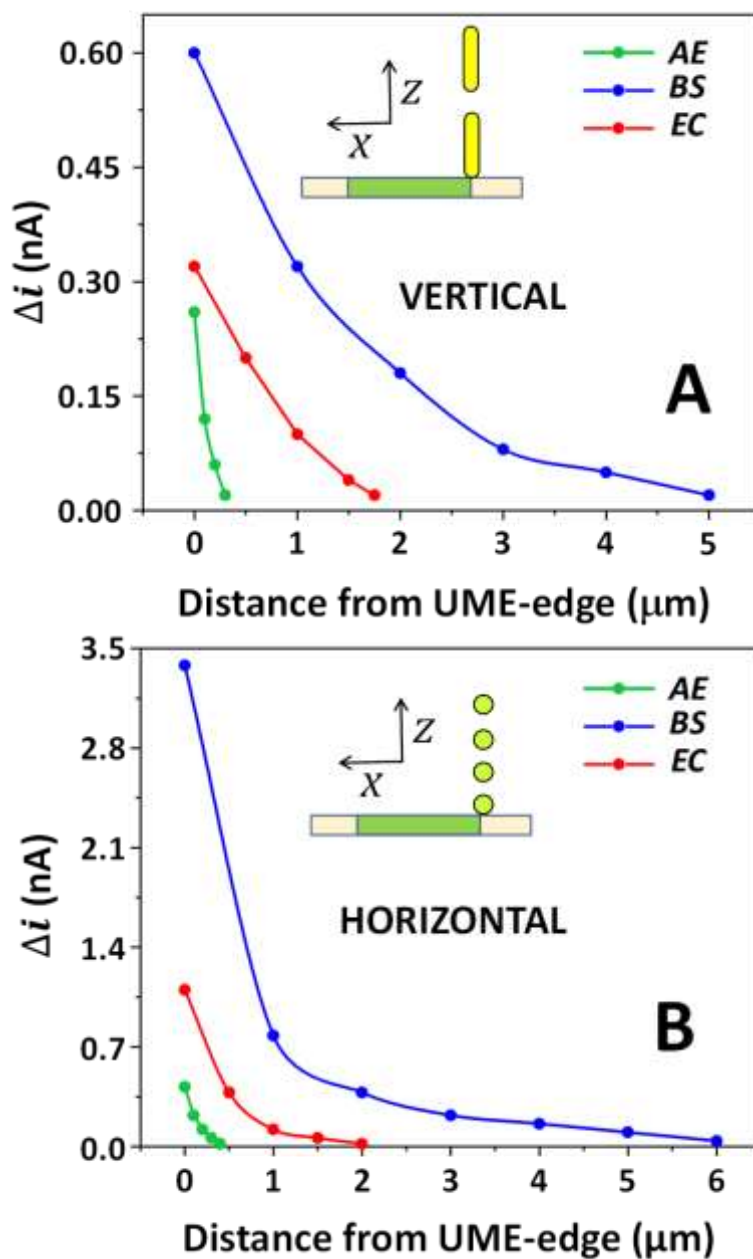


Figure 3.7: Δi -values simulated for bacilli at various distances from the UME-edge along the z-axis.

3.6.3 Transport mode of the bacteria: Though the Δi -signal is informed by the transport mechanism (frequency of collision, arrival speed, etc.), in the end the detection comes from adsorption on the UME surface. One advantage of the simulation approach here is that to make the analysis and reach the conclusions described so far, we do not need to know the transport mechanism of the bacteria. Furthermore, those mechanisms are represented in the simulation results because we use the experimental data to guide and fit the simulation. This is useful because the modes of transport that occur in bacteria are rather complex and can involve migration,²²⁻²⁴ diffusion, convection via electroosmosis,^{26, 28} and autonomous flagellated motion.¹²⁶⁻¹²⁷

The mass transport for particles in an electrochemical cell includes contributions from diffusion (d), migration (m) and convection (c):

$$J = J_d + J_m + J_c = -D\nabla C + \mu CE + Cv \quad 3.5$$

where, J , D , C and m , are the local flux, the diffusion coefficient, the concentration, and the electrophoretic mobility of the particles, E is the local electric field, v is the solution flow velocity, and ∇C is the spatial gradient of particle concentration.¹ The electrode blocking experiments were conducted in still solution, so convection was ignored. However, recently it was demonstrated in blocking experiments with bacteria, that convection can occur by way of electroosmotic flow due to the charge of the glass shroud.^{26, 28} In any case, here the discussion confines within diffusion and migration. The frequency of particle collision or adsorption by diffusion is given by:

$$f_d = 4DCN_A r_e \quad 3.6$$

where D , and C , are the diffusion coefficient and concentration of the particles, respectively, while N_A is the Avogadro's number and r_e is the electrode radius. Typically, the diffusion coefficient for spherical particles is estimated with the Stokes-Einstein equation:

$$D = \frac{k_B T}{6\pi\eta r} \quad 3.7$$

where k_B is the Boltzmann constant, T is the absolute temperature, η is the solution viscosity, and r is the radius of the particle. However, because bacilli are rod-shaped particles, with length (a) and width (b) we used the expressions for circular cylinders by Tirado and Garcia de la Torre:⁷⁵⁻⁷⁷

$$D = \frac{k_B T}{3\pi\eta a} \left[\ln\left(\frac{a}{b}\right) + w \right] \quad 3.8$$

$$w = 0.312 + 0.565 \frac{b}{a} - 0.1 \frac{b^2}{a^2} \quad 3.9$$

Table 3.2 shows the values of diffusion coefficient estimated with Eq. 3.8 and 3.9 for each bacillus, as well as the collision frequency calculated (f_d) with Eq. 3.6 and the experimental frequency (f_{exp}) obtained from the traces in Fig. 3.1.

Table 3.2. Diffusion and Frequency values for Bacilli.

Cell	D (cm ² /s)	f_d (Hz)	f_{exp} (Hz)
AE	5.57 x 10 ⁻⁹	0.00505	0.30
EC	3.82 x 10 ⁻⁹	0.00267	0.24
BS	2.20 x 10 ⁻⁹	0.00051	0.11

When examining the values of diffusional frequency f_d , it is evident, that bacillus diffusion is too slow to account for the experimental frequency, which must have contribution from migration given the value of zeta potential and electrophoretic mobility measured for these bacteria (Table B10, Appendix B). Additionally, the trend in arrival velocity estimated from Fig. 3.5 and 3.7 indicating that the large bacillus moves faster than the small one, further supports the dominance of migration over diffusion. This result is in general agreement with previous blocking experiments done with EC and BS.^{23, 116}

3.7 Conclusions

A systematic study has done combining experiments and numerical simulations of electrochemical blocking to determine relative differences in size, landing orientation and arrival velocity for three bacilli of varying lengths. The present work expands the scope of analysis and interpretation of electrochemical blocking data for micrometer-size particles like bacteria and possibly larger cells. This chapter shows that by assigning the most frequent values of blocking signals (Δi) to events at the UME edge, and with the aid of simulations, one can match experimental size data and in the case of bacilli, infer their landing orientation.

Despite all this, developing an electrochemical method to distinguish bacteria from one another based on size, still remains quite challenging. This is due to the bacteria's intrinsic broad polydispersity, influenced by culture conditions and other variables. However, thanks to the “slow dynamics” of bacteria, that allows the discerning of slight differences in the time scale of blocking signals, which are dependent on bacillus size and arrival velocity. This is a result of perturbations of the redox diffusional flux that start to occur at a certain threshold distance when the bacillus approaches the electrode. By simulating these perturbations, the arrival velocity for each bacillus was estimated, and reproducing the time profile of blocking signals was reproduced. In doing so,

it was found that the largest cell is the fastest and vice versa, indicating a dominance by migration over diffusion, and in agreement with previous work on these bacteria.

Chapter 4: Concluding Remarks and Future Direction

Electroanalytical chemistry is entering a digital era⁶⁴ with the introduction of SEE, where the signal has on and off properties similar to binary coding used in computers. For ensemble electrochemistry described in the overview of chapter 1, the current signals do not change rapidly with respect to time due to trillions or more electroactive analytes undergoing simultaneous electron-transfer reactions on the electrode surface. While in SEE, the signal is generated once an individual analyte particle collides and/or adsorbs on the electrode surface, thus, gaining a time-dependent profile. In my view, one needs to think innovatively to deconvolute the physicochemical properties related to these transient signals. Particularly, a better understanding of the particle interaction dynamics with UME with the effect of signal acquisitions on the resulting SEE signals is necessary to extract the properties correctly.

In most cases, systematic studies on particle-UME dynamics were done for fast-moving non-adsorbing nanoparticles, where the charge (q) transferred during their diffusional nanosecond collisional times (τ).^{43, 69, 71-72} In experimental $i - t$ curves, observed current spikes emerged from the merging of these nanoseconds peaks as the instrumental acquisitions time (t) is higher than their collisional times (τ). As a result, electrochemists devised creative experimental designs with simulations to address this challenge, such as driving NPs adsorption on modified electrode surface or spatially trapping them in nanopore.¹²⁸⁻¹³⁰ In case of microparticle, no dynamic model for the collision and adsorption is available except for the recent contribution detailed in Chapter 2.⁷⁸ This chapter explores systematically the dynamics of microdroplet (1.0 μm) with the UME as a model system. Our model strongly suggests that the electrochemical current spikes observed in $i - t$ curves at potentials to electrolyze droplet contents, come from single adsorption events instead of diffusional collisions. This chapter also demonstrated that the instrumental signal acquisition has

minimum effects on adsorbing droplet current signal while dramatically impacting current signals resulting from diffusional collisions. Chapter 3 of this dissertation explored the adsorption dynamics of rod-shaped bacteria cells in electrode blocking experiments. Based on this technique, this chapter is one of the few reports that described the systematic analysis of the current step signals to correlate with the bacteria's size, shape, velocity, and adsorption orientation. This also demonstrates the utility of SEE in determining the cytometric characteristics of living bacteria. In my view, the findings of this chapter could lay a foundation of analytical selectivity for detecting pathogens based on size, landing orientation, and approach speed.

While the experiments and simulations using emulsion droplets and bacteria were accomplished in this dissertation to advance SEE for microparticle analysis, the findings of chapters 2 and 3 can be used as a building block for future research. As chapter 2 demonstrated that the droplets irreversibly adsorbed on the electrode surface, the current signals generated by these droplets can be used to investigate a variety of physicochemical properties, including chemical partitioning, determining diffusion coefficient, droplet medium viscosity, surface tensions, and catalysis. In chapter 3, successful correlation of current signals to bacteria's adsorption dynamics (thanks to slow moving bacteria) has been established; however, quantitative research is required to evaluate the instrument acquisition effects on current step signals. This will provide the opportunity to decode the dynamics of fast-moving particle in electrode blocking experiments. Additionally, the sessile droplet system described in chapter 3 can be used to study the real-time response of bacteria on stimuli such as 2-propanol, ethanol, H₂O₂.

Lastly, the fundamental insights obtained by the emulsion droplets and the adsorption dynamics of single bacteria will advance the SEE field to design selective and specific sensors for relevant microparticles such as red blood cells, cancer cells, and sickle cells. Furthermore, these

findings will facilitate the studies of ion-transfer kinetics across the interface, drug-partitioning for drug delivery applications, and fundamental studies such as merging SEE signals to bulk signals.

Appendix A

A1. CV for 1 mM ferrocenemethanol for determining UME radius

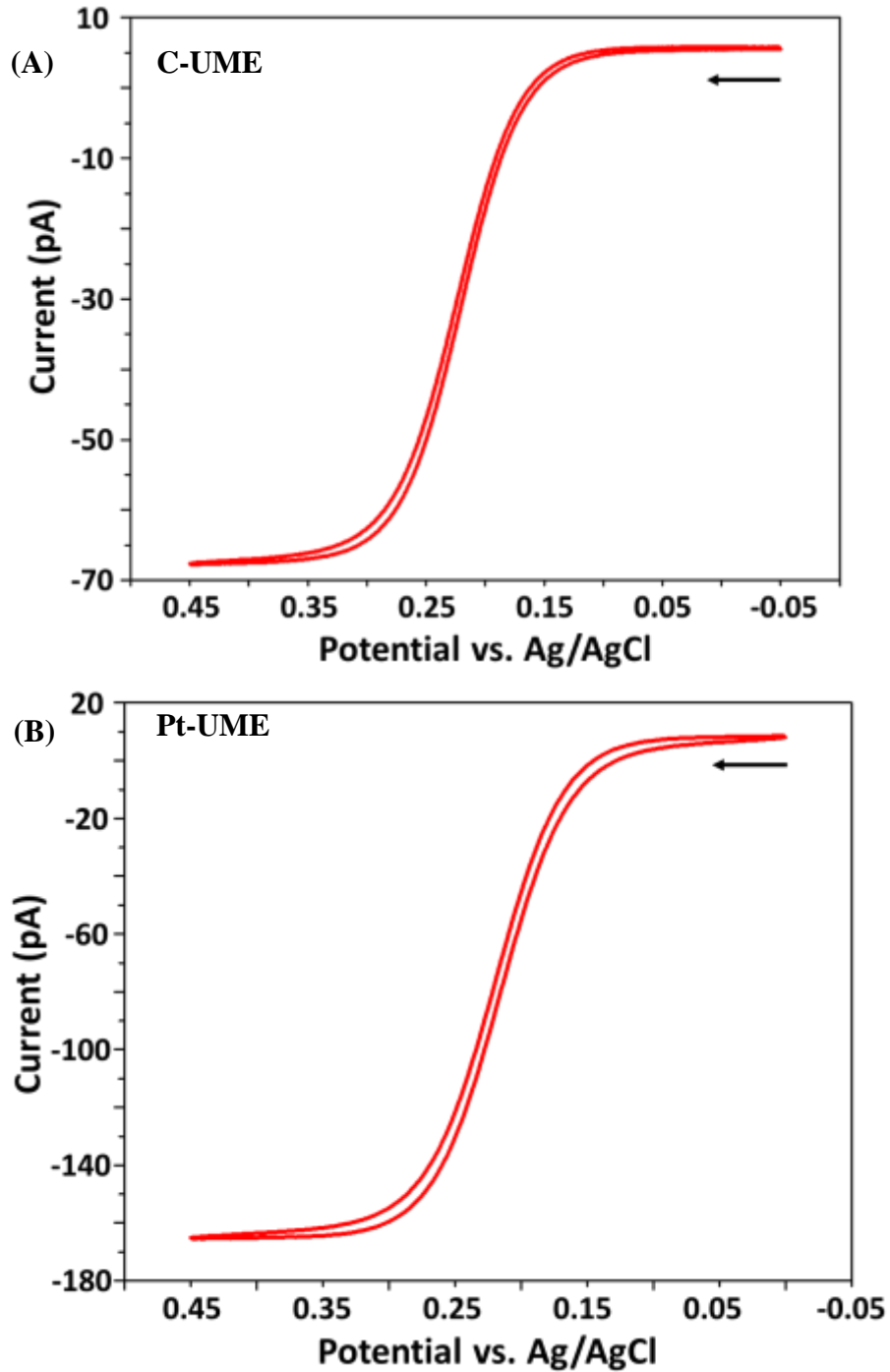


Figure A1: Cyclic voltammograms for 1 mM ferrocenemethanol and 0.1 M KCl aqueous solution at a scan rate of 10 mV/s. (A) 5.0 μm C-UME, (B) 11.4 μm Pt-UME

A2. CV of 20 mM ferrocene and 400 mM trihexyltetradecylphosphonium bis(trifluoromethylsulfonyl)amide (ILPA) in toluene

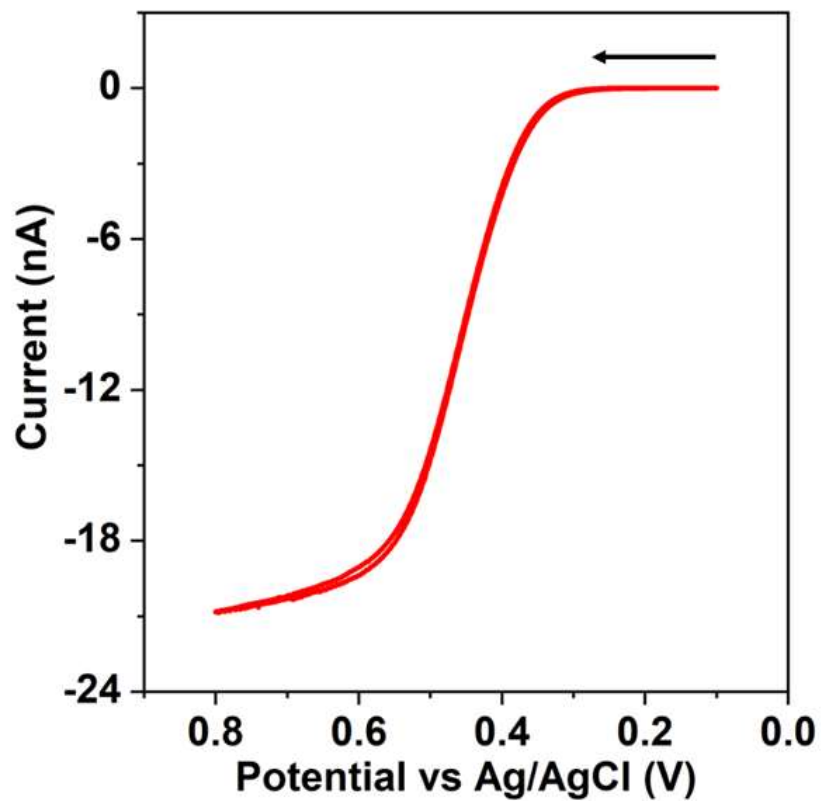


Figure A2: CV of 20 mM Fc and 400 mM ILPA in toluene at a scan rate of 20 mV/s with 5.0 μm C-UME (diameter).

A3. Expanded $i - t$ curves for 50 pM of toluene droplets in water at different oxidation potentials

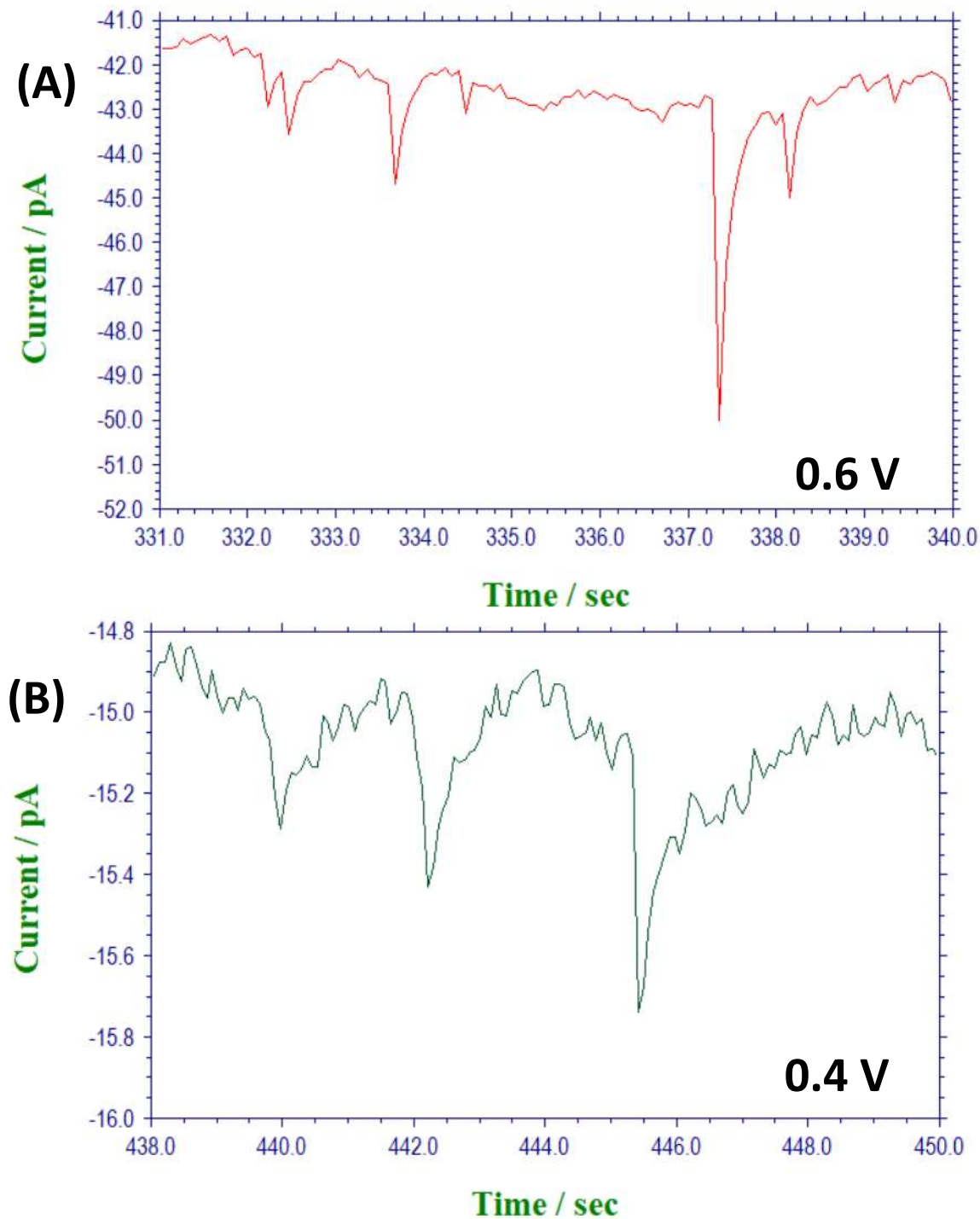


Figure A3: Expanded $i - t$ curves for 50 pM of toluene droplets in water at different oxidation potentials and Fc-concentration; C-UME of 5 μm -diameter. (A) 0.6 V and (B) 0.4 V vs Ag/AgCl reference electrode.

A4. Droplet distribution and random walk at the hemispherical simulation domain

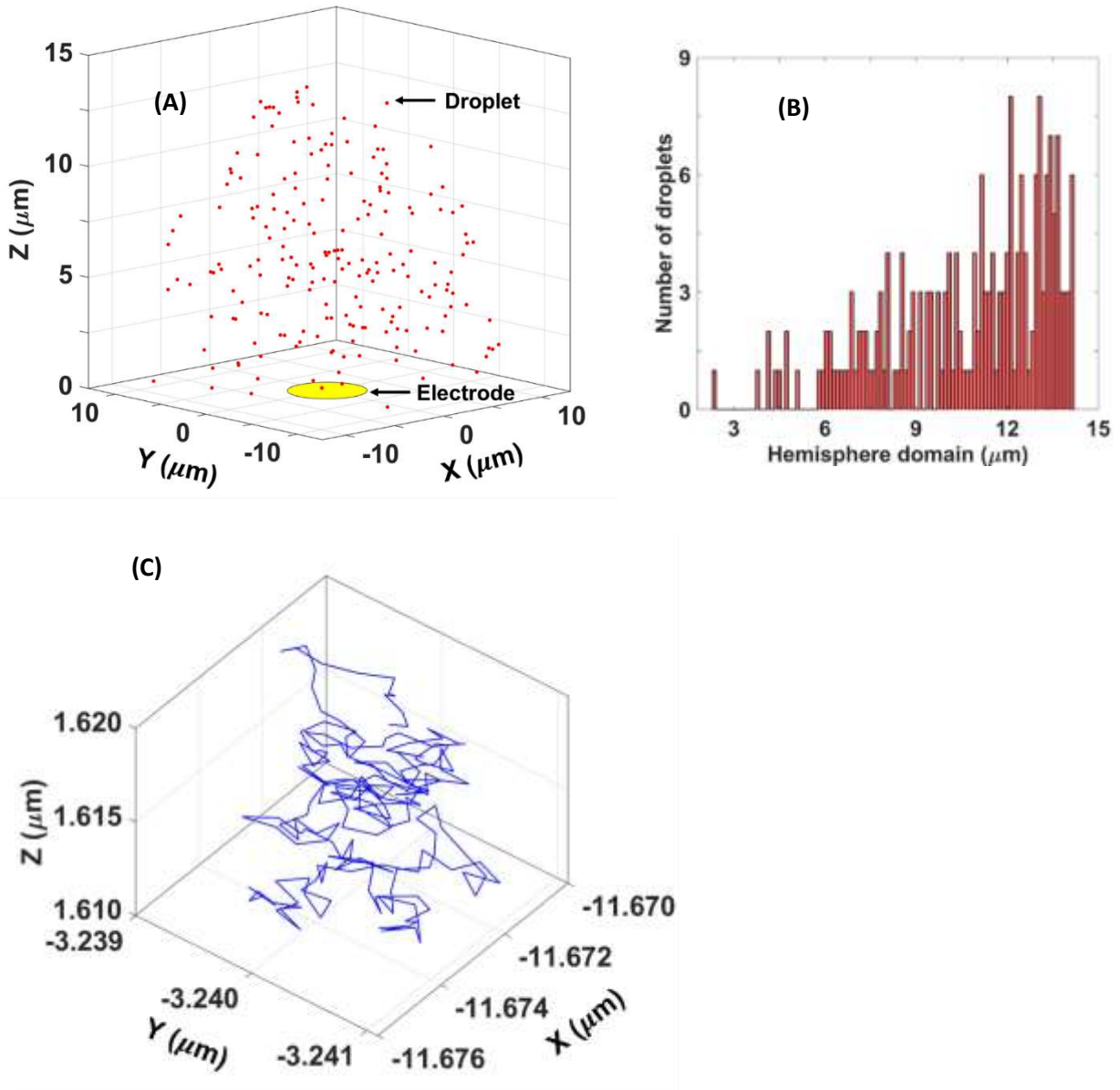


Figure A3: (A) Random distribution of 200 droplet particles inside the simulation hemispherical domain (radius 14.69 μm). (B) Distance of randomly generated droplets from the origin. (C) Random walk of a 1.0 μm droplet for 200 steps inside the hemispherical simulation domain. In every step the droplet travelled 0.57 nm (see table A.3.1 below).

Table A.4.1. Coordinates for random walk. The red outline designates the randomly generated starting position of the droplet.

Step number	X Coordinate	Y Coordinate	Z Coordinate	Distance Travelled (nm)
	-11.67232485	-3.238358867	1.618840233	
1	-11.67196078	-3.238490680	1.618428243	0.57
2	-11.67193077	-3.238384361	1.618982732	0.57
3	-11.67192819	-3.238069143	1.619452086	0.57
4	-11.67162549	-3.238086708	1.618974880	0.57
5	-11.67142036	-3.237864853	1.618497002	0.57
6	-11.67090775	-3.237684166	1.618341303	0.57
7	-11.67115875	-3.237196480	1.618204108	0.57
8	-11.67141129	-3.236699352	1.618297664	0.57
9	-11.67153023	-3.236324712	1.618704061	0.57
10	-11.67155451	-3.236072826	1.618198466	0.57
11	-11.67104229	-3.236226282	1.618014777	0.57
12	-11.67144686	-3.236608535	1.617915417	0.57
13	-11.67196002	-3.236833281	1.617991673	0.57
14	-11.67233190	-3.237193629	1.617764696	0.57
15	-11.67249695	-3.237608432	1.618111622	0.57
16	-11.67255363	-3.238074691	1.617796896	0.57
17	-11.67311706	-3.238121542	1.617799780	0.57
18	-11.67298104	-3.238646833	1.617640940	0.57
19	-11.67287614	-3.239146081	1.617397200	0.57
20	-11.67257134	-3.239411646	1.617792465	0.57
21	-11.67290826	-3.238987285	1.617631027	0.57
22	-11.67281090	-3.239301126	1.617170934	0.57
23	-11.67233583	-3.239001509	1.617235784	0.57
24	-11.67210599	-3.239137983	1.616737577	0.57
25	-11.67201096	-3.239573210	1.617085727	0.57
26	-11.67192109	-3.239039898	1.616920915	0.57
27	-11.67159919	-3.238865974	1.617351956	0.57
28	-11.67196878	-3.239283422	1.617258135	0.57
29	-11.67203377	-3.238765856	1.617040042	0.57
30	-11.67181123	-3.238530834	1.616576466	0.57
31	-11.67131304	-3.238624149	1.616826975	0.57
32	-11.67142360	-3.238895419	1.617310555	0.57
33	-11.67189221	-3.238922416	1.616995380	0.57
34	-11.67182799	-3.238673629	1.616491750	0.57
35	-11.67234448	-3.238572456	1.616698315	0.57
36	-11.67269232	-3.238891979	1.617009078	0.57
37	-11.67243849	-3.238386901	1.616997797	0.57

38	-11.67288453	-3.238070528	1.617141371	0.57
39	-11.67253982	-3.238205678	1.616714089	0.57
40	-11.67252103	-3.238450965	1.616205028	0.57
41	-11.67238178	-3.238997396	1.616246092	0.57
42	-11.67259308	-3.238637743	1.615864430	0.57
43	-11.67219320	-3.238982910	1.616065968	0.57
44	-11.67245232	-3.238976497	1.616568438	0.57
45	-11.67299501	-3.239095599	1.616673142	0.57
46	-11.67316568	-3.238719411	1.616287117	0.57
47	-11.67346982	-3.238383389	1.615949107	0.57
48	-11.67328105	-3.238916181	1.615936479	0.57
49	-11.67289007	-3.238596524	1.615682281	0.57
50	-11.67268628	-3.238092432	1.615837270	0.57
51	-11.67262033	-3.238438068	1.615394720	0.57
52	-11.67230406	-3.238902086	1.615328992	0.57
53	-11.67251917	-3.238769364	1.615834733	0.57
54	-11.67287780	-3.239029271	1.615483306	0.57
55	-11.67338300	-3.238956267	1.615726408	0.57
56	-11.67332424	-3.238396464	1.615779601	0.57
57	-11.67282415	-3.238145399	1.615860442	0.57
58	-11.67316298	-3.237694473	1.615821449	0.57
59	-11.67325634	-3.237308577	1.616223979	0.57
60	-11.67320369	-3.237801223	1.615951600	0.57
61	-11.67304640	-3.237258421	1.615934568	0.57
62	-11.67254061	-3.237459647	1.615781782	0.57
63	-11.67247488	-3.236901758	1.615845838	0.57
64	-11.67276220	-3.237297184	1.615561671	0.57
65	-11.67221340	-3.237238797	1.615438895	0.57
66	-11.67246032	-3.237272428	1.615946400	0.57
67	-11.67279865	-3.237291300	1.616398993	0.57
68	-11.67268045	-3.237033053	1.616887869	0.57
69	-11.67232380	-3.237242601	1.617273296	0.57
70	-11.67226933	-3.237765272	1.617481888	0.57
71	-11.67269988	-3.237821599	1.617843989	0.57
72	-11.67295341	-3.238005647	1.617373337	0.57
73	-11.67296595	-3.237883475	1.617925224	0.57
74	-11.67339235	-3.237811777	1.618289513	0.57
75	-11.67315118	-3.237372247	1.618028146	0.57
76	-11.67317375	-3.237728501	1.618466593	0.57
77	-11.67328389	-3.238234480	1.618693564	0.57
78	-11.67281259	-3.238534552	1.618607008	0.57
79	-11.67243088	-3.238362373	1.618227121	0.57

80	-11.67237665	-3.238558192	1.618754736	0.57
81	-11.67233505	-3.239116863	1.618831012	0.57
82	-11.67198353	-3.239488921	1.619071146	0.57
83	-11.67227494	-3.239557777	1.619550726	0.57
84	-11.67225505	-3.238996101	1.619489198	0.57
85	-11.67208069	-3.239160063	1.618976972	0.57
86	-11.67250380	-3.238824807	1.618808933	0.57
87	-11.67276559	-3.238571375	1.618376609	0.57
88	-11.67244528	-3.239027202	1.618280230	0.57
89	-11.67247309	-3.238591136	1.617921434	0.57
90	-11.67270182	-3.239106164	1.617967169	0.57
91	-11.67315855	-3.239145384	1.617636231	0.57
92	-11.67293640	-3.239030624	1.617129137	0.57
93	-11.67292922	-3.238465441	1.617115773	0.57
94	-11.67299616	-3.238271618	1.616588883	0.57
95	-11.67337144	-3.238144995	1.616992369	0.57
96	-11.67342823	-3.237864233	1.616504917	0.57
97	-11.67391368	-3.238020926	1.616261109	0.57
98	-11.67353843	-3.238346828	1.616530616	0.57
99	-11.67304845	-3.238222389	1.616277425	0.57
100	-11.67300555	-3.238262632	1.616839744	0.57
101	-11.67329263	-3.238743148	1.616760045	0.57
102	-11.67275363	-3.238680707	1.616601169	0.57
103	-11.67316478	-3.238498157	1.616943646	0.57
104	-11.67350331	-3.238436310	1.616495054	0.57
105	-11.67345518	-3.237985023	1.616157881	0.57
106	-11.67314953	-3.237934438	1.615684928	0.57
107	-11.67300840	-3.238481258	1.615711953	0.57
108	-11.67331050	-3.238948766	1.615612783	0.57
109	-11.67344086	-3.238777539	1.615089955	0.57
110	-11.67360111	-3.238260415	1.614926974	0.57
111	-11.67332918	-3.238214294	1.615420520	0.57
112	-11.67311474	-3.237875048	1.615818752	0.57
113	-11.67275702	-3.238302928	1.615725906	0.57
114	-11.67255969	-3.237860720	1.615434063	0.57
115	-11.67307342	-3.237625753	1.615457073	0.57
116	-11.67363110	-3.237714821	1.615430182	0.57
117	-11.67369434	-3.237702133	1.614868486	0.57
118	-11.67420878	-3.237509626	1.614734489	0.57
119	-11.67444817	-3.237968584	1.614961892	0.57
120	-11.67417552	-3.237747622	1.615405174	0.57
121	-11.67408373	-3.238069175	1.614949279	0.57

122	-11.67371981	-3.238273399	1.615330740	0.57
123	-11.67427681	-3.238360689	1.615288436	0.57
124	-11.67477476	-3.238113499	1.615391433	0.57
125	-11.67453683	-3.237625027	1.615235067	0.57
126	-11.67480574	-3.237193100	1.615481623	0.57
127	-11.67443301	-3.237610218	1.615563748	0.57
128	-11.67433967	-3.237952597	1.615123603	0.57
129	-11.67442698	-3.238078371	1.615667864	0.57
130	-11.67451577	-3.238592127	1.615886573	0.57
131	-11.67490119	-3.238965262	1.616065137	0.57
132	-11.67436919	-3.238861330	1.616225878	0.57
133	-11.67458140	-3.238940133	1.615707788	0.57
134	-11.67486602	-3.238829829	1.615231879	0.57
135	-11.67431832	-3.238950735	1.615303141	0.57
136	-11.67428037	-3.239511119	1.615367876	0.57
137	-11.67444921	-3.238977085	1.615445089	0.57
138	-11.67454869	-3.238537709	1.615103452	0.57
139	-11.67420519	-3.238874333	1.614806203	0.57
140	-11.67425105	-3.239151879	1.615296640	0.57
141	-11.67464664	-3.239352644	1.615647150	0.57
142	-11.67491301	-3.239435250	1.615155332	0.57
143	-11.67516931	-3.239795791	1.614803216	0.57
144	-11.67476018	-3.239464410	1.614597144	0.57
145	-11.67442076	-3.239427985	1.614146451	0.57
146	-11.67397005	-3.239756463	1.614053573	0.57
147	-11.67427190	-3.240141569	1.614336836	0.57
148	-11.67472886	-3.239970222	1.614051357	0.57
149	-11.67438216	-3.240000602	1.613605778	0.57
150	-11.67465153	-3.240187040	1.613144973	0.57
151	-11.67424080	-3.239873869	1.612915008	0.57
152	-11.67466036	-3.239523669	1.612770128	0.57
153	-11.67415910	-3.239663270	1.612548968	0.57
154	-11.67435028	-3.239309381	1.612151636	0.57
155	-11.67386505	-3.239581391	1.612050518	0.57
156	-11.67346811	-3.239496872	1.611656875	0.57
157	-11.67336659	-3.239386596	1.612202031	0.57
158	-11.67359619	-3.238870033	1.612191565	0.57
159	-11.67360870	-3.239145154	1.611697789	0.57
160	-11.67315642	-3.238861153	1.611883386	0.57
161	-11.67264384	-3.238678664	1.612037082	0.57
162	-11.67217981	-3.238985262	1.611935431	0.57
163	-11.67168735	-3.238802106	1.611726610	0.57

164	-11.67118446	-3.238548710	1.611777153	0.57
165	-11.67128524	-3.238272032	1.612259808	0.57
166	-11.67093061	-3.238403240	1.612680147	0.57
167	-11.67122050	-3.238668792	1.612273814	0.57
168	-11.67118121	-3.238885306	1.611753007	0.57
169	-11.67148917	-3.239254182	1.612050925	0.57
170	-11.67177377	-3.239738517	1.612114842	0.57
171	-11.67224408	-3.239818215	1.611811329	0.57
172	-11.67188226	-3.239404025	1.611942463	0.57
173	-11.67167382	-3.239926414	1.611884808	0.57
174	-11.67158566	-3.239535849	1.612283994	0.57
175	-11.67197597	-3.239260651	1.611981358	0.57
176	-11.67195199	-3.238743379	1.612208330	0.57
177	-11.67240267	-3.238920247	1.611916325	0.57
178	-11.67268124	-3.238428433	1.611929841	0.57
179	-11.67309521	-3.238130581	1.611685764	0.57
180	-11.67325219	-3.237639947	1.611452743	0.57
181	-11.67337776	-3.237783024	1.610920368	0.57
182	-11.67285551	-3.237583536	1.611004768	0.57
183	-11.67324641	-3.237602047	1.610596704	0.57
184	-11.67375970	-3.237634370	1.610831554	0.57
185	-11.67375974	-3.238152796	1.611057158	0.57
186	-11.67431041	-3.238275536	1.611094011	0.57
187	-11.67406497	-3.237857727	1.611385313	0.57
188	-11.67355503	-3.237661977	1.611239352	0.57
189	-11.67396120	-3.237304340	1.611075702	0.57
190	-11.67408156	-3.237762830	1.610767538	0.57
191	-11.67460804	-3.237669039	1.610951050	0.57
192	-11.67481137	-3.238192878	1.611013592	0.57
193	-11.67472481	-3.237796369	1.611407228	0.57
194	-11.67464222	-3.238125205	1.611859675	0.57
195	-11.67501489	-3.237834538	1.612169985	0.57
196	-11.67520353	-3.237781857	1.612700365	0.57
197	-11.67565291	-3.237778203	1.613043440	0.57
198	-11.67518372	-3.237666913	1.612748259	0.57
199	-11.67542884	-3.238109203	1.613001153	0.57
200	-11.67528693	-3.237562845	1.612969269	0.57

A5. Droplet diameter vs. effective contact radius, r_{eff} , of the droplet.

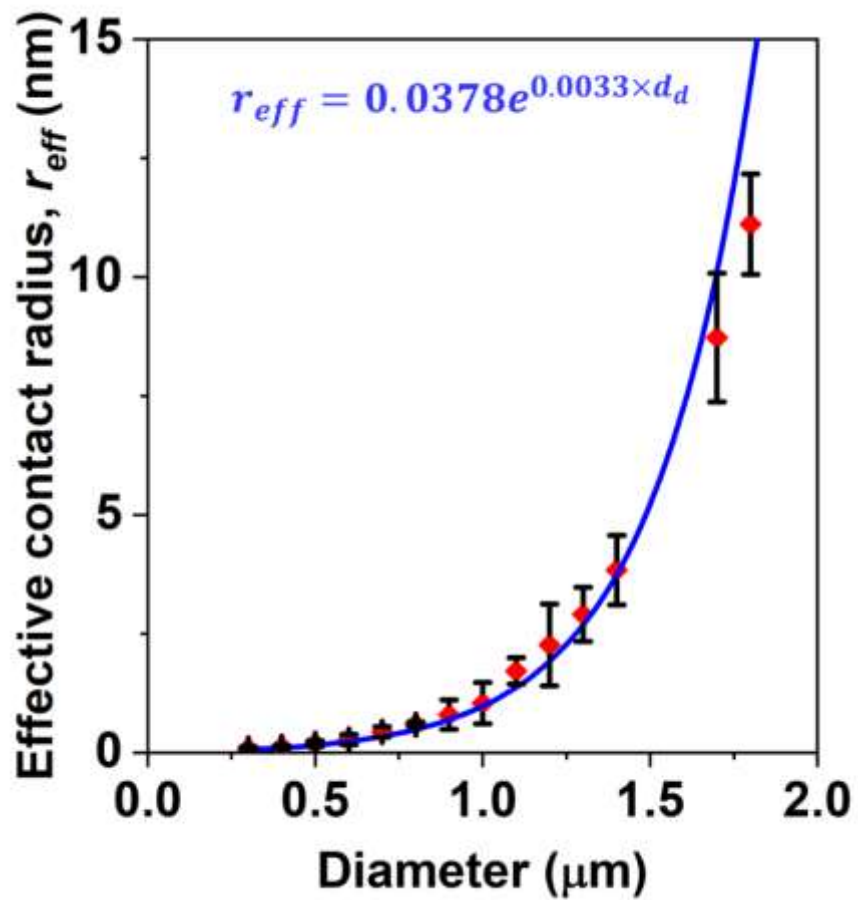


Figure A5: Droplet diameter vs. effective contact radius, r_{eff} , of the droplet. The blue line is the fitted line from the given best fit equation.

A6. Droplet adsorption from random walk (blue); Fc electrolysis (black) and (B) $i - t$ response from adsorbed 1.0 μm droplet.

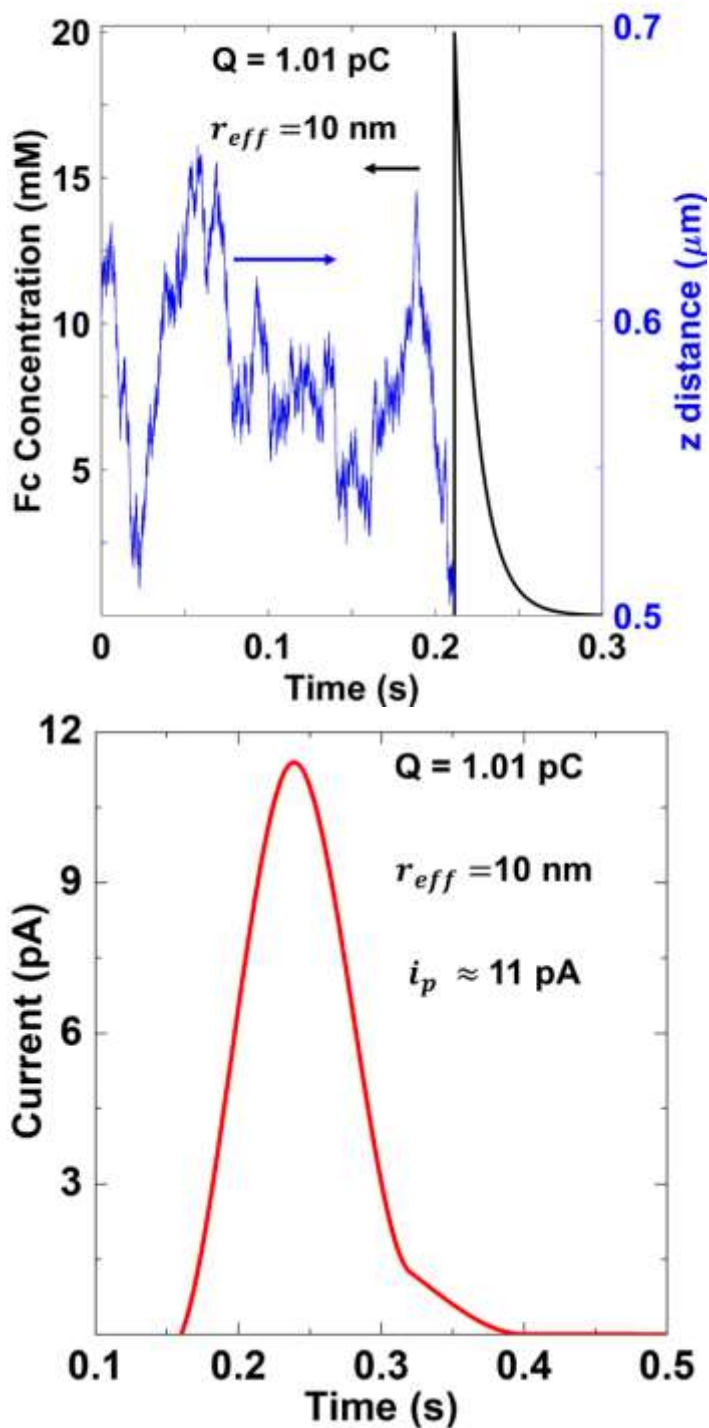


Figure A6: (A) Droplet adsorption from random walk (blue); Fc electrolysis (black) and (B) $i - t$ response from adsorbed 1.0 μm droplet.

A7. Experimental current peaks of the droplet producing ~ 11 pA peak current.

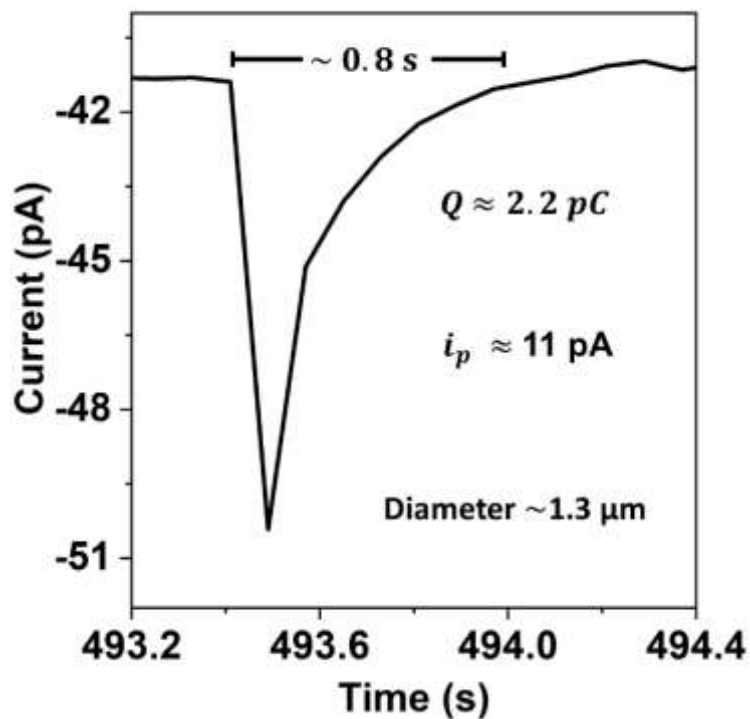
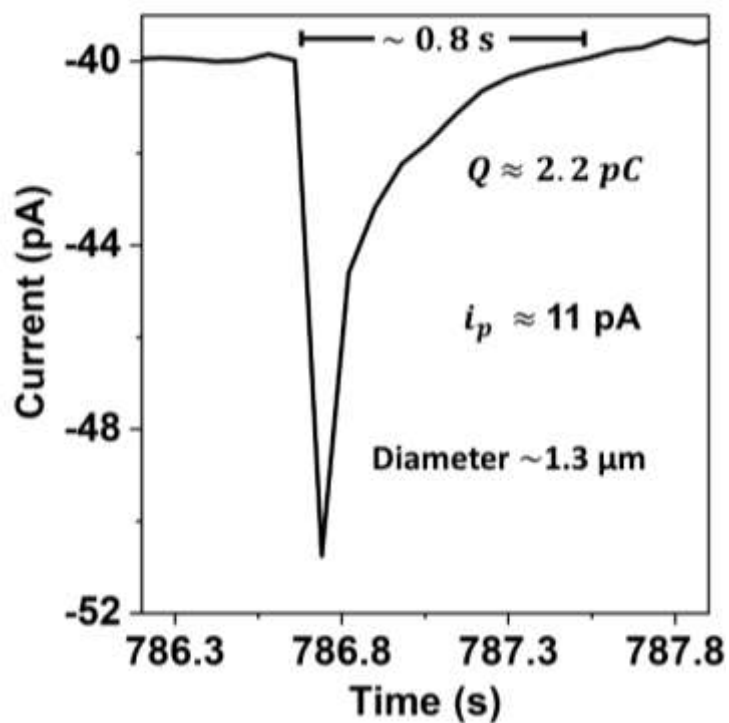


Figure A7: Experimental current peaks of the droplet producing ~ 11 pA peak current.

A8. Simulated Steady-state current of 100 mM ferrocyanide solution.

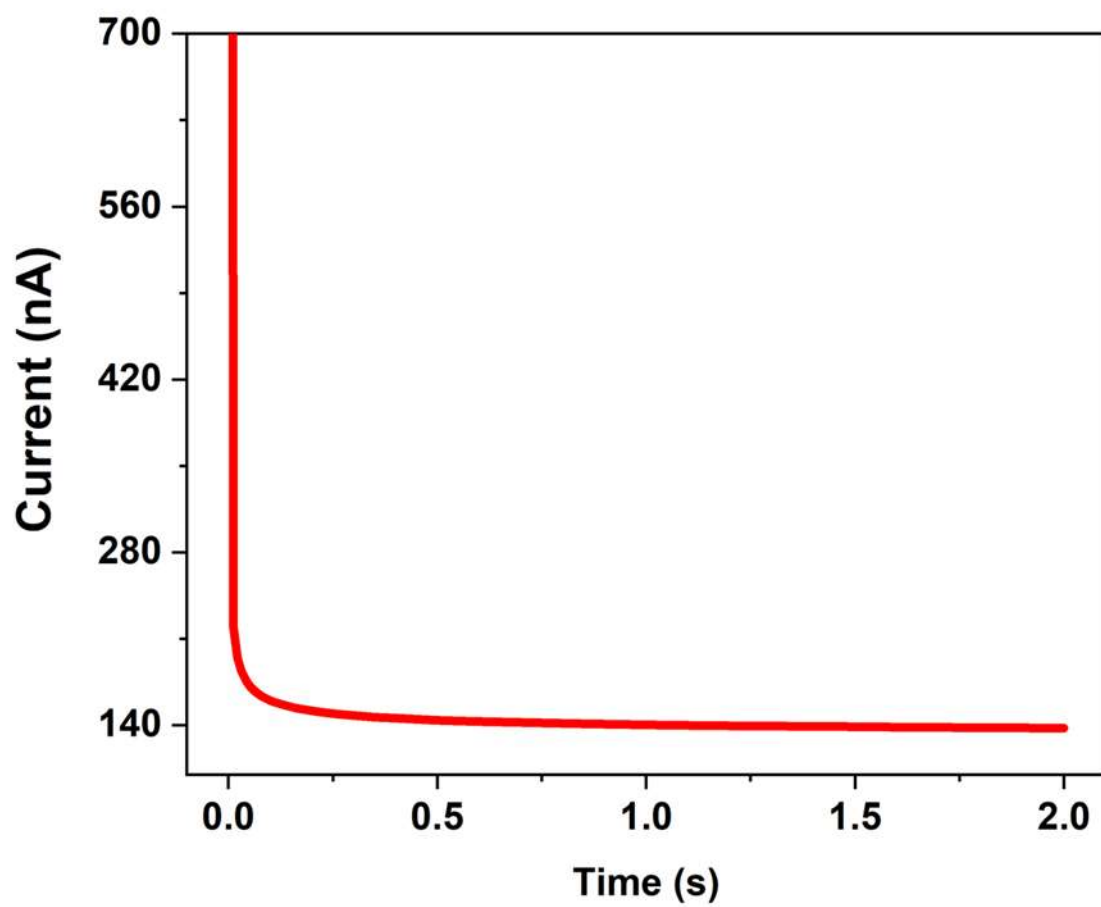


Figure A8: Simulated Steady-state current of 100 mM Ferrocyanide solution.

A9. Simulated ferrocyanide flux at the electrode surface

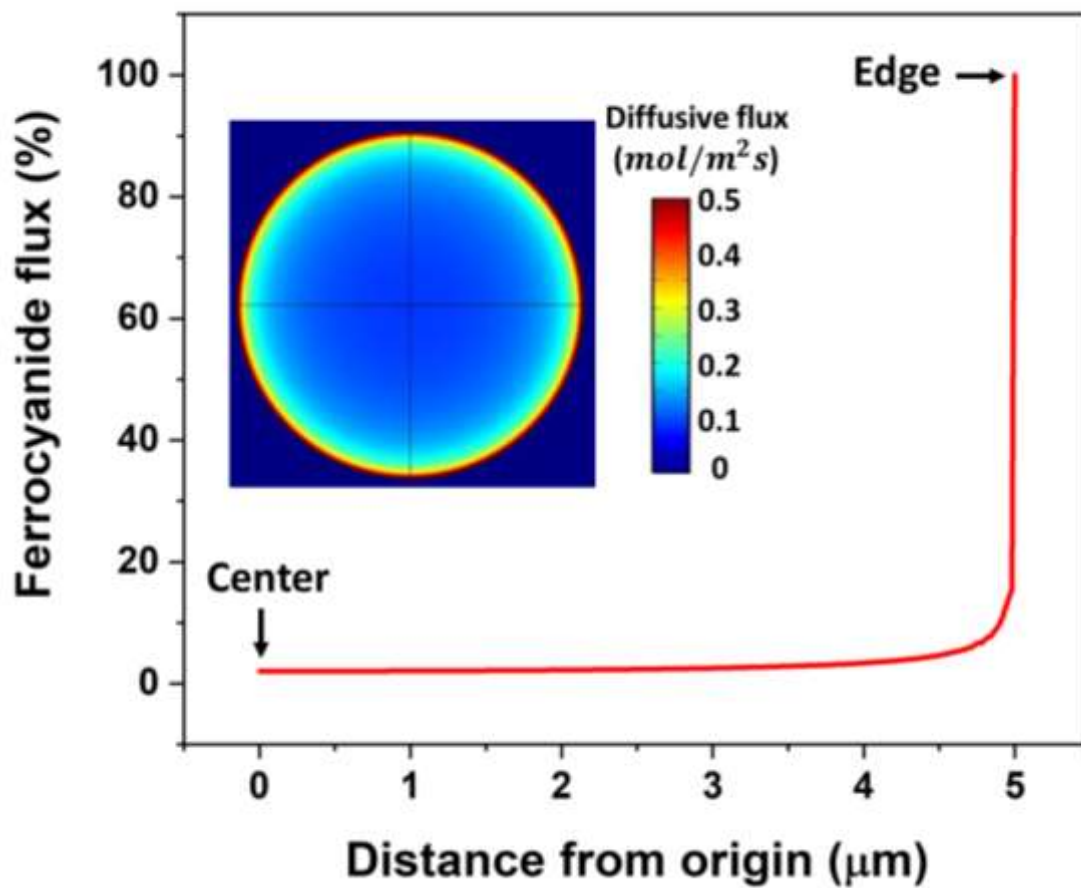


Figure A9: Simulated ferrocyanide flux along the radius of 10 μm (diameter) Pt-UME surface. Inset: The flux at the UME surface.

A10. Electron microscopy images of the bacteria

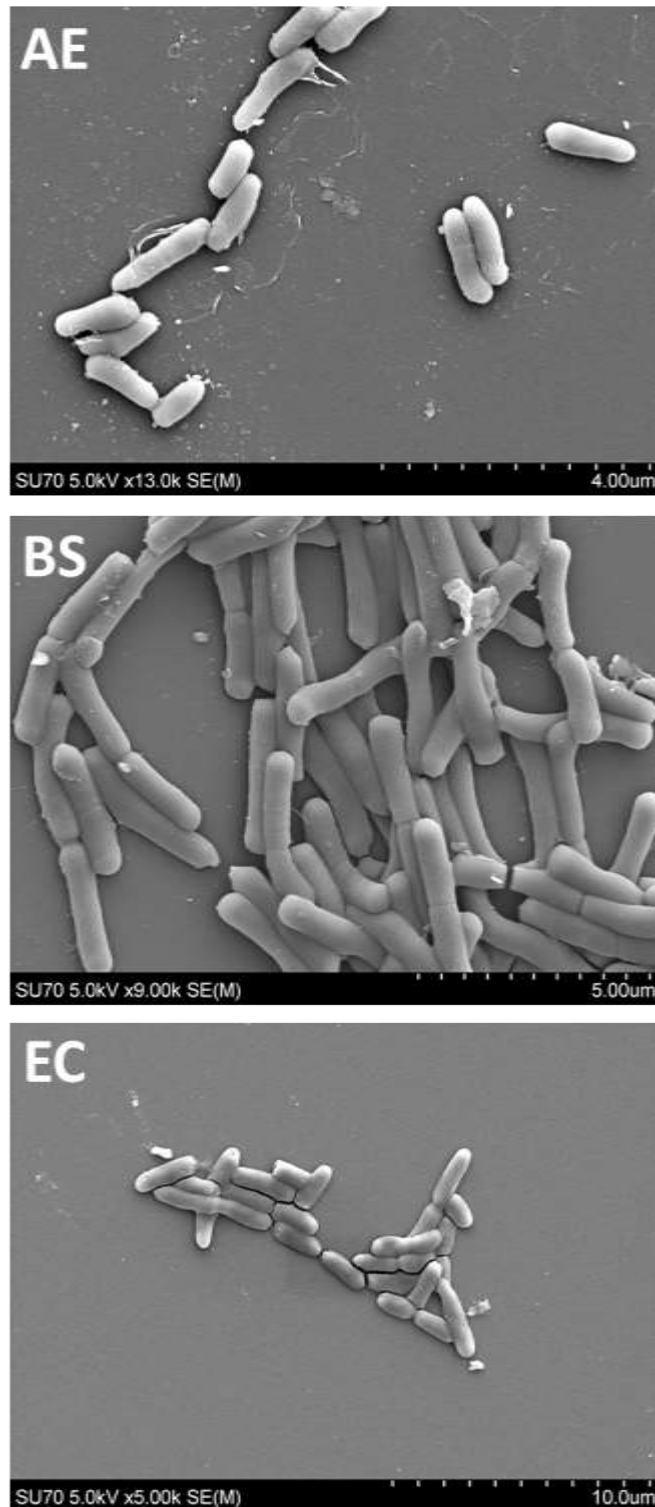


Figure A10: Scanning Electron Microscopy images of the bacteria, A) *A. erythreum*, B) *B. subtilis*, C) *E. coli*

A11. Simulated ferrocyanide concentration perturbation by the BS at various separation distances electrode

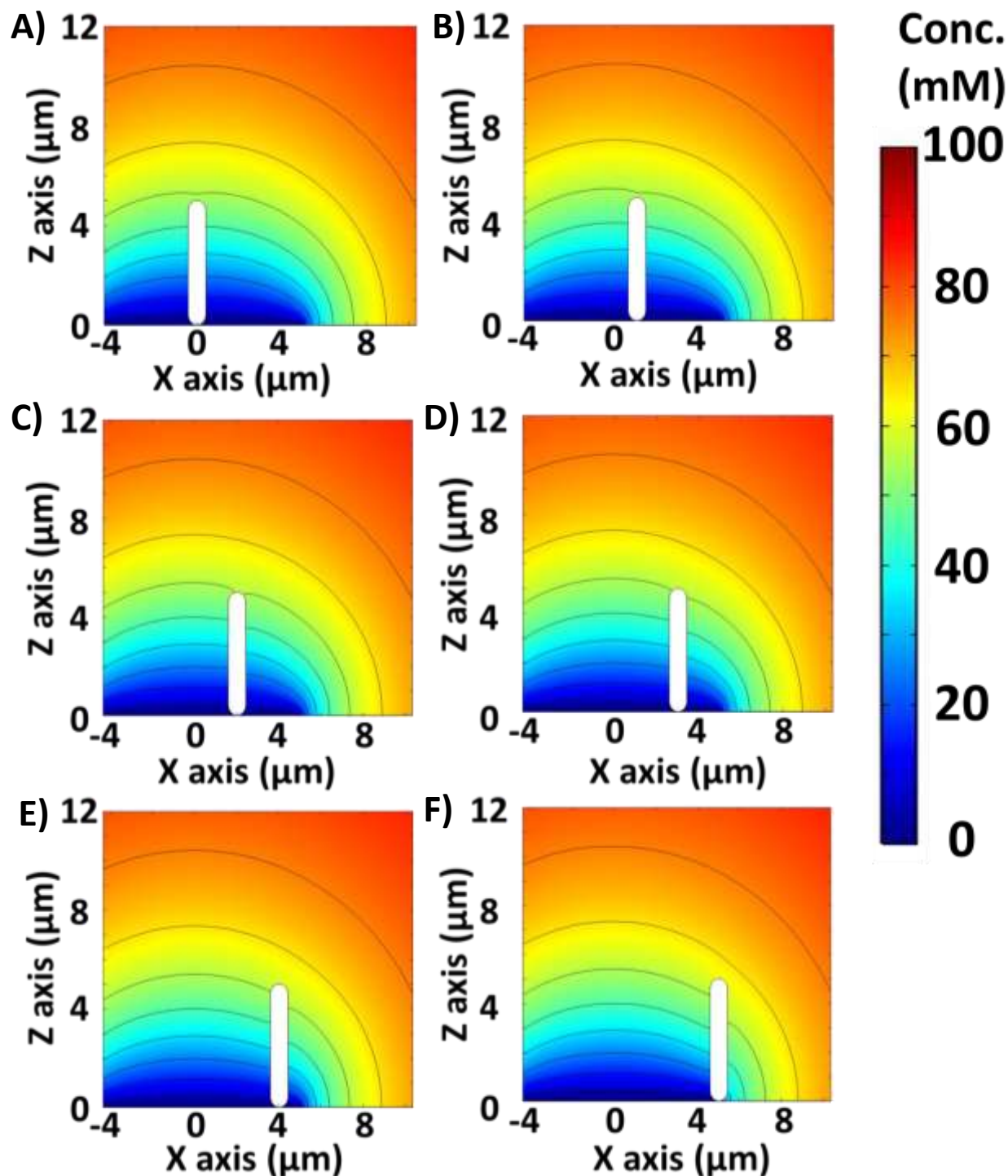


Figure A11: Simulated Ferrocyanide concentration perturbation by the BS at A) 0 μm , B) 1 μm , C) 2 μm , D) 3 μm , E) 4 μm , F) 5 μm separation distance from electrode center.

Appendix B

B1. Calculation of UME radius

Concentration of ferrocenemethanol, $C_{Fcm} = 1 \text{ mM} = 1 \times 10^{-6} \text{ mol/cm}^3$

Diffusion coefficient of ferrocenemethanol,¹⁰⁵ $D_{Fcm} = 7.8 \times 10^{-6} \text{ cm}^2/\text{s}$

Number of electron-transferred, $n = 1$

Faraday constant, $F = 96485.33 \text{ C/mol}$

C-UME:

Steady-state current for 1 mM ferrocenemethanol, $I_{ss} = 75 \text{ pA} = 7.5 \times 10^{-10} \text{ C/s}$

$$\begin{aligned} \text{Radius of C-UME} &= \frac{I_{ss}}{4\pi n C_{Fcm} D_{Fcm}} \\ &= \frac{7.5 \times 10^{-10} \text{ C/s}}{4 \times \pi \times 1 \times \left(1 \times 10^{-6} \frac{\text{mol}}{\text{cm}^3}\right) \times \left(7.8 \times 10^{-6} \frac{\text{cm}^2}{\text{s}}\right)} = 2.5 \times 10^{-6} \text{ cm} = 2.5 \mu\text{m} \end{aligned}$$

Diameter of C-UME = $2.5 \times 2 \mu\text{m} = 5.0 \mu\text{m}$

Pt-UME:

Steady-state current for 1 mM ferrocenemethanol, $I_{ss} = 75 \text{ nA} = 1.72 \times 10^{-9} \text{ C/s}$

$$\begin{aligned} \text{Radius of C-UME} &= \frac{I_{ss}}{4\pi n C_{Fcm} D_{Fcm}} \\ &= \frac{1.72 \times 10^{-9} \text{ C/s}}{4 \times \pi \times 1 \times \left(1 \times 10^{-6} \frac{\text{mol}}{\text{cm}^3}\right) \times \left(7.8 \times 10^{-6} \frac{\text{cm}^2}{\text{s}}\right)} = 5.7 \times 10^{-6} \text{ cm} = 5.7 \mu\text{m} \end{aligned}$$

Diameter of C-UME = $5.7 \times 2 \mu\text{m} = 11.4 \mu\text{m}$

B2. Calculation of Droplet Concentration

Total volume of the emulsion, $V = 5 \text{ mL (water)} + 0.1 \text{ mL (toluene)} = 5.1 \text{ mL}$

Average diameter of droplet (DLS), $d_d = 1.0 \mu\text{m}$

$$\text{Volume of } 1.0 \mu\text{m droplet} = \frac{4}{3}\pi(0.5d_d)^3 = 0.52 \mu\text{m}^3$$

$$\text{Number of droplets formed by } 0.1 \text{ mL toluene} = \frac{0.1 \text{ mL} \times 10^{12} \mu\text{m}^3 \text{ mL}^{-1}}{0.52 \mu\text{m}^3} = 1.91 \times 10^{11}$$

$$\text{Moles of droplets} = \frac{1.91 \times 10^{11}}{6.023 \times 10^{23} \text{ mole}^{-1}} = 3.17 \times 10^{-13} \text{ mole}$$

$$\text{Concentration of droplets in } 5.1 \text{ mL emulsion solution} = \frac{3.17 \times 10^{-13} \text{ mole}}{5.1 \text{ mL} \times 1 \text{ L}/1000 \text{ mL}} = 6.22 \times$$

$$10^{-12} \text{ mole/L} = 62.2 \text{ pM}$$

For electrochemical droplet Fc oxidation, 1 mL of water was added to 4 mL of emulsion to obtain 50 pM droplet concentration.

For droplet blocking experiments, 0.1 mL of emulsion was added to 4 mL of redox solution to obtain 1.5 pM droplet concentration.

B3. Calculation of Theoretical charge for 1.0 μm droplet

Concentration of ferrocene, $C_{Fc} = 20 \text{ mM}$

$$\text{Faraday constant, } F = 96485.33 \frac{\text{C}}{\text{mole}}$$

Number of electrons transferred per molecule, $n = 1$

Droplet diameter, $d_d = 1.0 \mu\text{m}$

$$\text{Droplet volume, } V = \frac{1}{6}\pi d_d^3$$

$$\text{Charge containing } 1.0 \mu\text{m droplet, } q = F \times n \times C_{Fc} \times V = \frac{1}{6} \times F \times n \times C_{Fc} \times \pi \times d_d^3 =$$

$$1.01 \times 10^{-12} \text{ C} = 1.01 \text{ pC}$$

B4. Calculation of Time required for complete electrolysis of Fc per droplet collision

The concentration of the Fc content inside the droplet is as follows:

$$C_{redox}^*(t) = C_{redox}^*(0)e^{-\left(\frac{4D_{redox}r_{eff}}{V_{droplet}}\right)\tau} \dots\dots (S1)$$

The initial concentration of the Fc, $C_{Fc} = 20 \text{ mM} = 2.00 \times 10^{-17} \text{ mol}/\mu\text{m}^3$.

Diameter of the droplet is $1.0 \mu\text{m}$, so the volume of the droplet, $V_d = 0.52 \mu\text{m}^3$

Effective contact radius, $r_{eff} = 1 \text{ nm} = 0.001 \mu\text{m}$

Step time, $\tau = 0.11 \mu\text{s}$

Faraday constant, $F = 96485.33 \text{ C/mol}$

Now, $\left(\frac{4D_{redox}r_{eff}}{V_{droplet}}\right)\tau = 8.91 \times 10^{-7}$ and $e^{-\left(\frac{4D_{redox}r_{eff}}{V_{droplet}}\right)\tau} = 0.99$

So, the concentration of Fc inside the droplet reduces to, $C_{redox}^* = 1.99 \times 10^{-17} \text{ mol}/\mu\text{m}^3$ for the first collision.

The change in concentration for this collision, $\Delta C = (2.00 \times 10^{-17} - 1.99 \times 10^{-17}) \text{ mol}/\mu\text{m}^3$

The number of electron transfer for ferrocene, $n = 1$

Charge passed for this collision $= nF\Delta CV_d = 1 \times 96485.33 \frac{\text{C}}{\text{mol}} \times 1.78 \times 10^{-23} \frac{\text{mol}}{\mu\text{m}^3} \times$

$0.52 \mu\text{m}^3 = 9.00 \times 10^{-19} \text{ C} = 9.00 \times 10^{-7} \text{ pC}$

A significant point to notice is, $C_{redox}^*(0)$ for the second collision is now the reduced concentration of the Fc inside the droplet due to the first collision, not the initial $2.00 \times 10^{-17} \text{ mol}/\mu\text{m}^3$.

Another significant point is that the amount of charge passed in every collision is not constant as the concentration reduces on successive collisions. For the first 50 collisions, the starting concentration of Fc inside the droplet, the subsequent change in concentration, and the charge passed for each collision is computed and presented in Table B5.

As the amount of passed charge is not constant and the value is very small, a MATLAB code was developed to estimate the time requires to pass ~1.01 pC of charge. The code calculated the concentration change for every collision according to Eq. S1 and computed the change in concentration and charge passed. It requires ~0.6 seconds to pass this amount of charge.

So, the number of collisions in this time = $\frac{0.6 \text{ s}}{0.11 \times 10^{-6} \text{ s}} = 5.45 \times 10^6$ collision

To determine the average collisional frequency (ACF) for a 1.0 μm droplet, the simulation was run 500 times and the ACF was calculated by the following formula:

$$\text{ACF} = \frac{\frac{\sum \text{Collision number of each droplet}}{\text{Simulation runtime}}}{\text{Simulation number}}$$

The calculated ACF was 1.2 KHz, thus it requires = $\frac{5.45 \times 10^6 \text{ collision}}{1.2 \times 10^3 \frac{\text{collision}}{\text{second}}} = 4545.5$ seconds = 1.26

hours for complete electrolysis of the droplet Fc content.

Table B5. Concentration and charge change in droplet per collision (data shown for 50 collisions).

Collision Number	Concentration of Fc (mol/μm^3)	Change in Concentration (mol/μm^3)	Charge passed (pC)
1	1.99999822E-17	1.78151598E-23	9.00011679E-07
2	1.99999644E-17	1.78151439E-23	9.00010878E-07
3	1.99999466E-17	1.78151280E-23	9.00010076E-07
4	1.99999287E-17	1.78151122E-23	9.00009274E-07
5	1.99999109E-17	1.78150963E-23	9.00008472E-07
6	1.99998931E-17	1.78150804E-23	9.00007671E-07
7	1.99998753E-17	1.78150646E-23	9.00006869E-07
8	1.99998575E-17	1.78150487E-23	9.00006067E-07
9	1.99998397E-17	1.78150328E-23	9.00005266E-07
10	1.99998218E-17	1.78150170E-23	9.00004464E-07
11	1.99998040E-17	1.78150011E-23	9.00003662E-07
12	1.99997862E-17	1.78149852E-23	9.00002861E-07
13	1.99997684E-17	1.78149694E-23	9.00002059E-07

14	1.99997506E-17	1.78149535E-23	9.00001257E-07
15	1.99997328E-17	1.78149376E-23	9.00000456E-07
16	1.99997150E-17	1.78149217E-23	8.99999654E-07
17	1.99996971E-17	1.78149059E-23	8.99998852E-07
18	1.99996793E-17	1.78148900E-23	8.99998051E-07
19	1.99996615E-17	1.78148741E-23	8.99997249E-07
20	1.99996437E-17	1.78148583E-23	8.99996447E-07
21	1.99996259E-17	1.78148424E-23	8.99995645E-07
22	1.99996081E-17	1.78148265E-23	8.99994844E-07
23	1.99995903E-17	1.78148107E-23	8.99994042E-07
24	1.99995724E-17	1.78147948E-23	8.99993240E-07
25	1.99995546E-17	1.78147789E-23	8.99992439E-07
26	1.99995368E-17	1.78147631E-23	8.99991637E-07
27	1.99995190E-17	1.78147472E-23	8.99990835E-07
28	1.99995012E-17	1.78147313E-23	8.99990034E-07
29	1.99994834E-17	1.78147155E-23	8.99989232E-07
30	1.99994656E-17	1.78146996E-23	8.99988430E-07

31	1.99994477E-17	1.78146837E-23	8.99987629E-07
32	1.99994299E-17	1.78146678E-23	8.99986827E-07
33	1.99994121E-17	1.78146520E-23	8.99986025E-07
34	1.99993943E-17	1.78146361E-23	8.99985224E-07
35	1.99993765E-17	1.78146202E-23	8.99984422E-07
36	1.99993587E-17	1.78146044E-23	8.99983620E-07
37	1.99993408E-17	1.78145885E-23	8.99982819E-07
38	1.99993230E-17	1.78145726E-23	8.99982017E-07
39	1.99993052E-17	1.78145568E-23	8.99981215E-07
40	1.99992874E-17	1.78145409E-23	8.99980414E-07
41	1.99992696E-17	1.78145250E-23	8.99979612E-07
42	1.99992518E-17	1.78145092E-23	8.99978810E-07
43	1.99992340E-17	1.78144933E-23	8.99978009E-07
44	1.99992161E-17	1.78144774E-23	8.99977207E-07
45	1.99991983E-17	1.78144616E-23	8.99976405E-07
46	1.99991805E-17	1.78144457E-23	8.99975604E-07
47	1.99991627E-17	1.78144298E-23	8.99974802E-07

48	1.99991449E-17	1.78144139E-23	8.99974000E-07
49	1.99991271E-17	1.78143981E-23	8.99973199E-07
50	1.99991093E-17	1.78143822E-23	8.99972397E-07

B6. Calculation of Current density for 1 nm and 10 nm effective contact radius

The $E_{1/2} = E^0 = 0.43 \text{ V Ag/AgCl}$ for ferrocene in 400 mM ILPA and toluene was determined from the CV (Fig. A2). Applying 0.6V provides the overpotential, $\eta = E_{applied} - E^0 \approx 0.17 \text{ V Ag/AgCl}$. Thus the $J_{BV} = 195.2 \text{ A/cm}^2$

The current density for the given effective contact radii was determined using equation 2.9 of Chapter 2.

For Fc oxidation, the number of electrons transferred, $n = 1$, the initial concentration of the Fc, $C_{Fc}^* = 20 \text{ mM}$, the diffusion coefficient of the Fc, $D_{Fc} = 1.06 \times 10^{-5} \text{ cm}^2/\text{s}$, and the Faraday constant, $F = 96485.33 \text{ C/mol}$.

For 1 nm effective contact radius, $r_{eff} = 1 \text{ nm}$, and $i_1 = 4nFD_{Fc}C_{Fc}^* r_{eff} = 8.18 \times 10^{-12} \text{ A}$

Area for $r_{eff} = 1 \text{ nm}$, $A_1 = \pi \times r_{eff}^2 = 3.14 \text{ nm}^2 = 3.14 \times 10^{-14} \text{ cm}^2$

Thus, current density, $J_1 = \frac{i_1}{A_1} = 260.4 \text{ A/cm}^2$

For 10 nm effective contact radius, $r_{eff} = 10 \text{ nm}$, and $i_2 = 4nFD_{Fc}C_{Fc}^* r_{eff} = 8.18 \times 10^{-11} \text{ A}$

Area for $r_{eff} = 10 \text{ nm}$, $A_2 = \pi \times r_{eff}^2 = 3.14 \times 10^2 \text{ nm}^2 = 3.14 \times 10^{-12} \text{ cm}^2$

Thus, current density, $J_2 = \frac{i_2}{A_2} = 26.0 \text{ A/cm}^2$

B7. Determination of Bacteria cell concentration

Initially, the optical density (OD) of the bacteria was determined in Luria-Bertani (LB) at 600 nm wavelength. The *Aeromicrobium erythreum* (AE) bacteria solution was diluted by eight orders of magnitude in LB media, while *Bacillus subtilis* (BS), and *Escherichia coli* (EC) were diluted seven orders of magnitude. 100 μL of the respective bacteria solutions were spread on separate LB agar plates and grown in the same conditions described in the main text. After culturing, each bacteria colony was counted to determine the optical dilution factor. This dilution factor was then used to determine cells/mL. Table B7.1 shows the concentration of bacteria cells.

Table B7.1. Concentration of the bacteria

Bacteria	OD₆₀₀	cells/mL	Concentration (pM)
<i>Aeromicrobium erythreum</i> (AE)	2.00 ± 0.10	2.0×10^9	3.32
<i>Bacillus subtilis</i> (BS)	1.70 ± 0.05	2.6×10^8	0.42
<i>Escherichia coli</i> (EC)	1.94 ± 0.06	1.6×10^9	2.58

Table B8. No. of steps in every 60 seconds in the experimental $i - t$ curve

Time interval (s)	Average number of steps		
	<i>Aeromicrobium erythreum (AE)</i>	<i>Bacillus subtilis (BS)</i>	<i>Escherichia coli (EC)</i>
0-60	23 ± 4	9 ± 3	17 ± 5
61-120	15 ± 3	6 ± 1	15 ± 4
121-180	15 ± 1	5 ± 1	12 ± 3

Table B9. Required number of bacteria for monolayer electrode surface coverage

Bacteria	Number of bacteria for monolayer coverage	Total number of steps observed experimentally in 180 s
<i>Aeromicrobium erythreum (AE)</i>	131 (Horizontal orientation)	54 ± 9 (41.2 %)
<i>Bacillus subtilis (BS)</i>	142 (Vertical orientation)	20 ± 4 (14.08 %)
<i>Escherichia coli (EC)</i>	230 (Vertical orientation)	44 ± 4 (19.1%)

Table B10. Zeta potential of the bacteria at 0.01 M potassium ferrocyanide solution

Bacteria	Zeta potential, ζ (mV)	Electrophoretic mobility, μ $\times 10^{-4}(\text{cm}^2/\text{Vs})$
<i>Aeromicrobium erythreum</i> (AE)	-42.1	-3.34
<i>Bacillus subtilis</i> (BS)	-45.2	-3.56
<i>Escherichia coli</i> (EC)	-56.4	-4.40

Appendix C

COMSOL Report



10 um platinum diskelectrode potentiostatic simulation

Report date

Mar 17, 2022 4:02:44 PM

Contents

1. Global Definitions.....	103
1.1. Parameters.....	103
2. Component 1	104
2.1. Definitions.....	104
2.2. Geometry 1	104
2.3. Materials	105
2.4. Electroanalysis 2	106
2.5. Mesh 1	107
3. Study 1.....	108
3.1. Time Dependent.....	108
4. Results	109
4.1. Datasets	109
4.2. Tables.....	113
4.3. Plot Groups.....	119

1 Global Definitions

Date	Mar 17, 2022 12:07:43 PM
------	--------------------------

GLOBAL SETTINGS

Name	10 um platinum diskelectrode potentiostatic simulation.mph
Path	D:\Comsol\Junaid\10 um platinum diskelectrode potentiostatic simulation.mph
Version	COMSOL Multiphysics 5.6 (Build: 401)

USED PRODUCTS

COMSOL Multiphysics
Electrochemistry Module

COMPUTER INFORMATION

CPU	Intel64 Family 6 Model 165 Stepping 5, 10 cores
Operating system	Windows 10

1.1 PARAMETERS

PARAMETERS 1

Name	Expression	Value	Description
c_bulk	100[mmol/L]	100 mol/m ³	Reactant concentration
re	5[um]	5E-6 m	Electrode radius
r_max	500E-6 [m]	5E-4 m	Size of simulation
D	0.67E-9[m ² /s]	6.7E-10 m ² /s	Reactant diffusion Coefficient
E_vertex	0.4[V]	0.4 V	Applied potential
A_el	pi*re^2	7.854E-11 m ²	Electrode area
IDr	200E-6 [m]	2E-4 m	Inner Domain Radius

2 Component 1

2.1 DEFINITIONS

2.1.1 Selections

3

Selection type
Explicit

Selection
No boundaries

2.1.2 Coordinate Systems

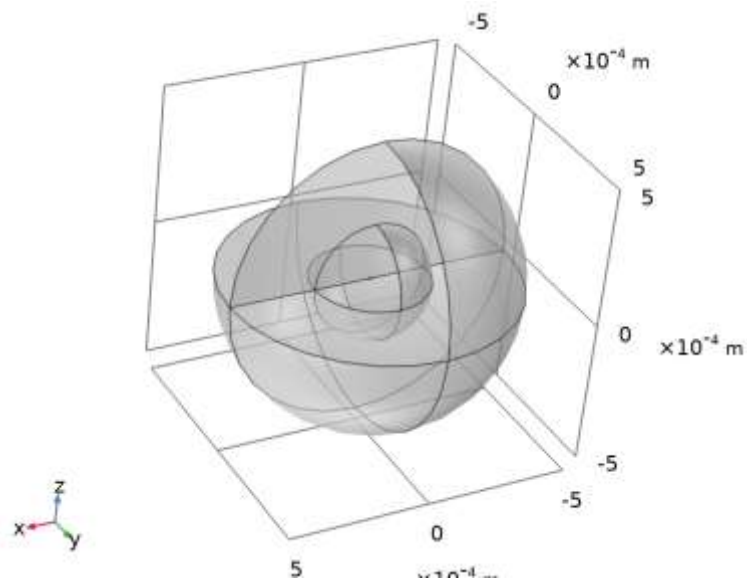
Boundary System 1

Coordinate system type	Boundary system
Tag	sys1

COORDINATE NAMES

First	Second	Third
t1	t2	n

2.2 GEOMETRY 1



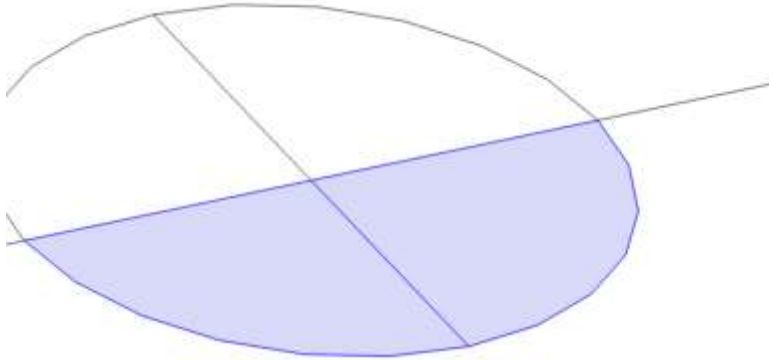
Geometry 1

UNITS

Length unit	m
Angular unit	deg

2.3 MATERIALS

2.3.1 Platinum

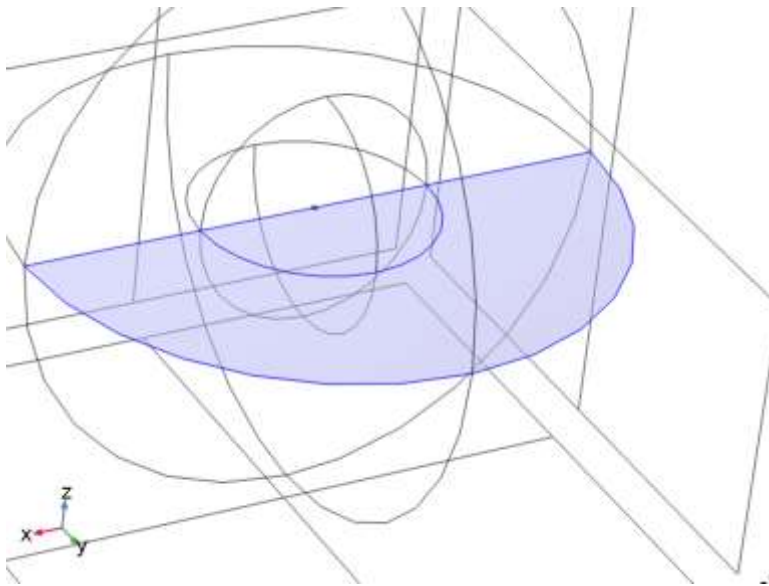


Platinum

SELECTION

Geometric entity level	Boundary
Selection	Geometry geom1: Dimension 2: Boundaries 14, 20

2.3.2 Glass (quartz)

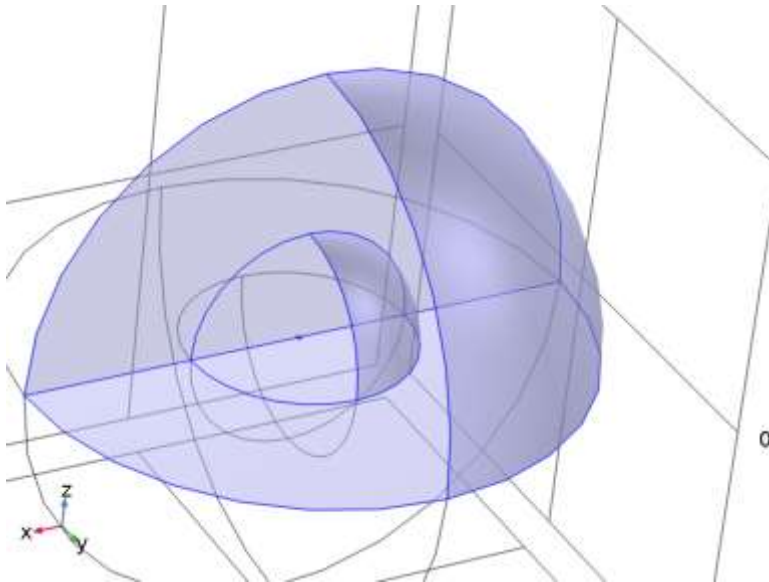


Glass (quartz)

SELECTION

Geometric entity level	Boundary
Selection	Geometry geom1: Dimension 2: Boundaries 3, 9

2.3.3 Water, liquid

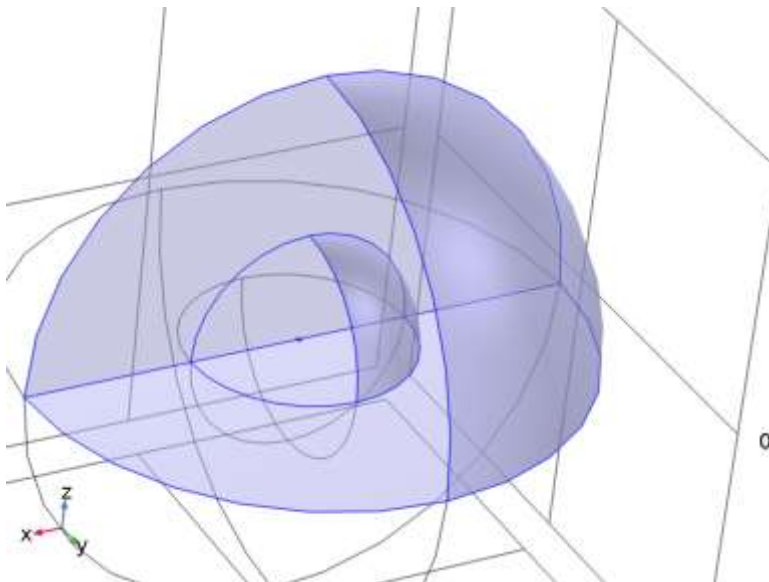


Water, liquid

SELECTION

Geometric entity level	Domain
Selection	Geometry geom1: Dimension 3: Domains 2, 4

2.4 ELECTROANALYSIS 2



Electroanalysis 2

EQUATIONS

$$\frac{\partial c_i}{\partial t} + \nabla \cdot \mathbf{J}_i + \mathbf{u} \cdot \nabla c_i = R_i$$

$$\nabla \cdot \mathbf{i}_s = Q_s$$

$$\mathbf{J}_i = -D_i \nabla c_i$$

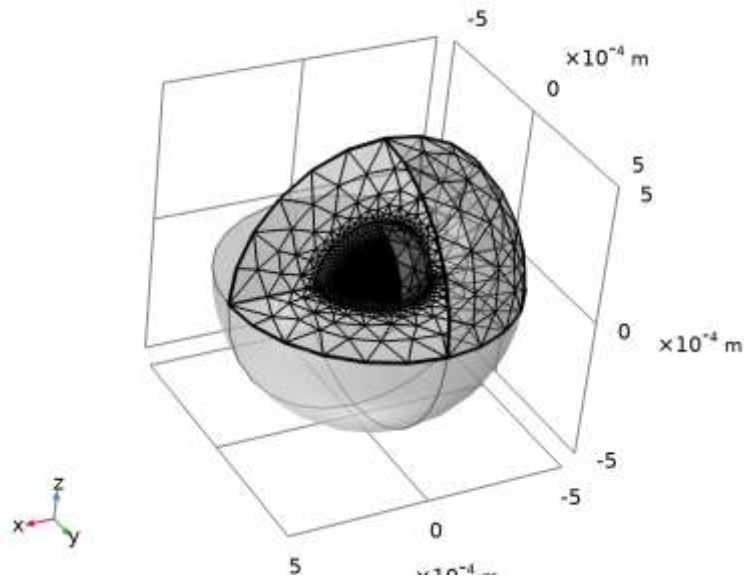
$$\mathbf{i}_s = -\sigma_s \nabla \phi_s$$

$$\phi_1 = 0, \quad \phi_s = \text{phis2}$$

FEATURES

Name	Level
Electrolyte 1	Domain
No Flux 1	Boundary
Insulation 1	Boundary
Initial Values 1	Domain
Electrode Surface 1	Boundary
Symmetry 1	Boundary

2.5 MESH 1



Mesh 1

3 Study 1

COMPUTATION INFORMATION

Computation time	32 min 59 s
------------------	-------------

3.1 TIME DEPENDENT

Times	Unit
range(0,0.01,2)	s

STUDY SETTINGS

Description	Value
Include geometric nonlinearity	Off

STUDY SETTINGS

Description	Value
Output times	{0, 0.01, 0.02, 0.03, 0.04, 0.05, 0.06, 0.07, 0.08, 0.09, 0.1, 0.11, 0.12, 0.13, 0.14, 0.15, 0.16, 0.17, 0.18, 0.19, 0.2, 0.21, 0.22, 0.23, 0.24, 0.25, 0.26, 0.27, 0.28, 0.29, 0.3, 0.31, 0.32, 0.33, 0.34, 0.35000000000000003, 0.36, 0.37, 0.38, 0.39, 0.4, 0.41000000000000003, 0.42, 0.43, 0.44, 0.45, 0.46, 0.47000000000000003, 0.48, 0.49, 0.5, 0.51, 0.52, 0.53, 0.54, 0.55, 0.56, 0.57000000000000001, 0.58, 0.59, 0.6, 0.61, 0.62, 0.63, 0.64, 0.65, 0.66, 0.67, 0.68, 0.69000000000000001, 0.70000000000000001, 0.71, 0.72, 0.73, 0.74, 0.75, 0.76, 0.77, 0.78, 0.79, 0.8, 0.81, 0.82000000000000001, 0.83000000000000001, 0.84, 0.85, 0.86, 0.87, 0.88, 0.89, 0.9, 0.91, 0.92, 0.93, 0.94000000000000001, 0.95000000000000001, 0.96, 0.97, 0.98, 0.99, 1, 1.01, 1.02, 1.03, 1.04, 1.05, 1.06, 1.07, 1.08, 1.09, 1.1, 1.11, 1.12, 1.13000000000000001, 1.14000000000000001, 1.15000000000000001, 1.16, 1.17, 1.18, 1.19, 1.2, 1.21, 1.22, 1.23, 1.24, 1.25, 1.26, 1.27, 1.28, 1.29, 1.3, 1.31, 1.32, 1.33, 1.34, 1.35, 1.36, 1.37, 1.38000000000000001, 1.39000000000000001, 1.40000000000000001, 1.41, 1.42, 1.43, 1.44, 1.45, 1.46, 1.47, 1.48, 1.49, 1.5, 1.51, 1.52, 1.53, 1.54, 1.55, 1.56, 1.57, 1.58, 1.59, 1.6, 1.61, 1.62, 1.63000000000000001, 1.64000000000000001, 1.65000000000000001, 1.66000000000000001, 1.67, 1.68, 1.69, 1.7, 1.71, 1.72, 1.73, 1.74, 1.75, 1.76, 1.77, 1.78, 1.79, 1.8, 1.81, 1.82, 1.83, 1.84, 1.85, 1.86, 1.87, 1.88000000000000001, 1.89000000000000001, 1.90000000000000001, 1.91000000000000001, 1.92, 1.93, 1.94, 1.95, 1.96, 1.97, 1.98, 1.99, 2}

PHYSICS AND VARIABLES SELECTION

Physics interface	Discretization
Electroanalysis 2 (tcd2)	physics

MESH SELECTION

Geometry	Mesh
Geometry 1 (geom1)	mesh1

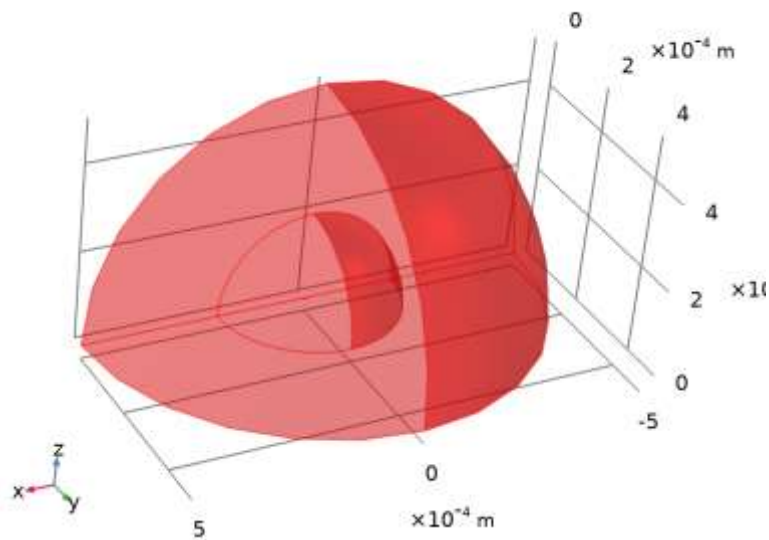
4 Results

4.1 DATASETS

4.1.1 Study 1/Solution 1

SOLUTION

Description	Value
Solution	Solution 1
Component	Component 1 (comp1)



Dataset: Study 1/Solution 1

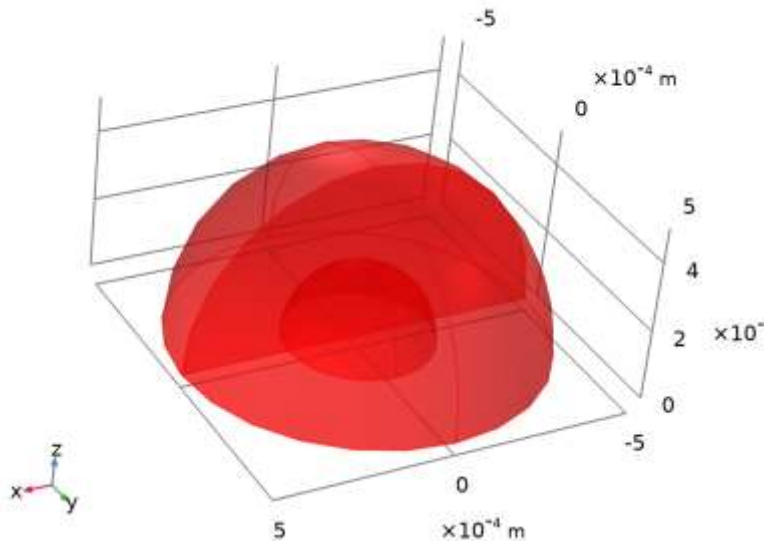
4.1.2 Mirror 3D 1

DATA

Description	Value
Dataset	Study 1/Solution 1

PLANE DATA

Description	Value
Plane type	Quick
Plane	XZ - planes
Y-coordinate	0



Dataset: Mirror 3D 1

4.1.3 Surface 1

DATA

Description	Value
Dataset	Study 1/Solution 1

PARAMETERIZATION

Description	Value
x- and y-axes	Surface parameters

4.1.4 Cut Plane 1

DATA

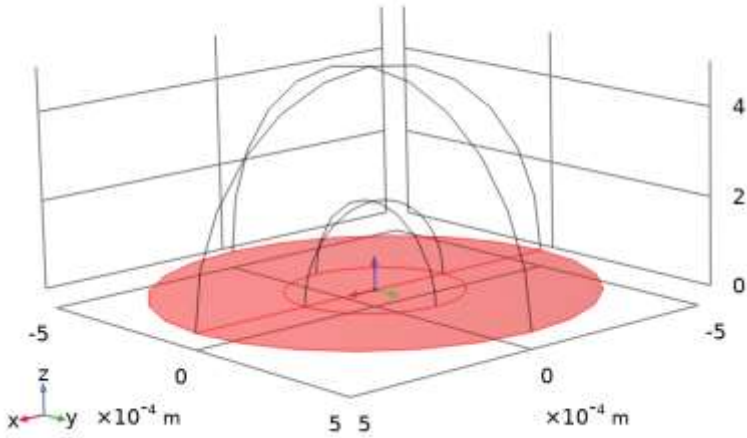
Description	Value
Dataset	Mirror 3D 1

PLANE DATA

Description	Value
Plane type	Quick
Plane	xy - planes
z-coordinate	0

ADVANCED

Description	Value
Space variables	{cpl1x, cpl1y}
Normal variables	{cpl1nx, cpl1ny, cpl1nz}



Dataset: Cut Plane 1

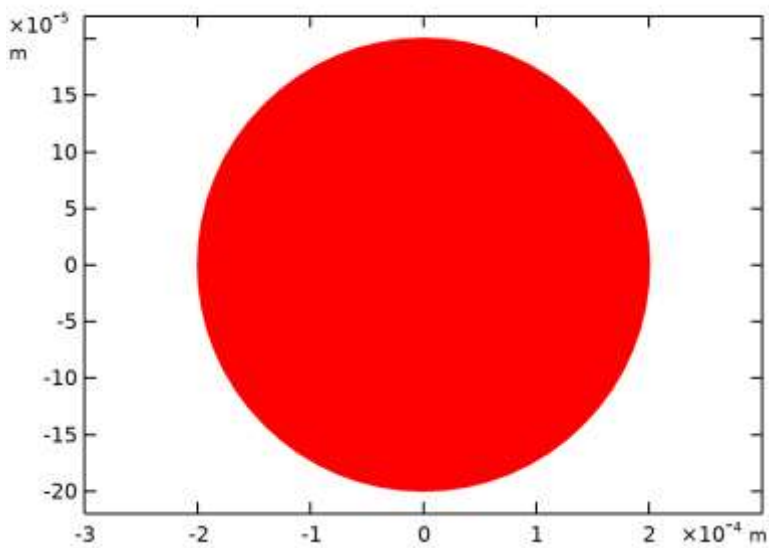
4.1.5 Mirror 2D 2

DATA

Description	Value
Dataset	Surface 1

AXIS DATA

Description	Value
Axis entry method	Two points
Points	{{0, 0}, {1, 0}}



Dataset: Mirror 2D 2

4.1.6 Surface 2

DATA

Description	Value
Dataset	Study 1/Solution 1

PARAMETERIZATION

Description	Value
x- and y-axes	Surface parameters

4.1.7 Cut Line 2D 1

DATA

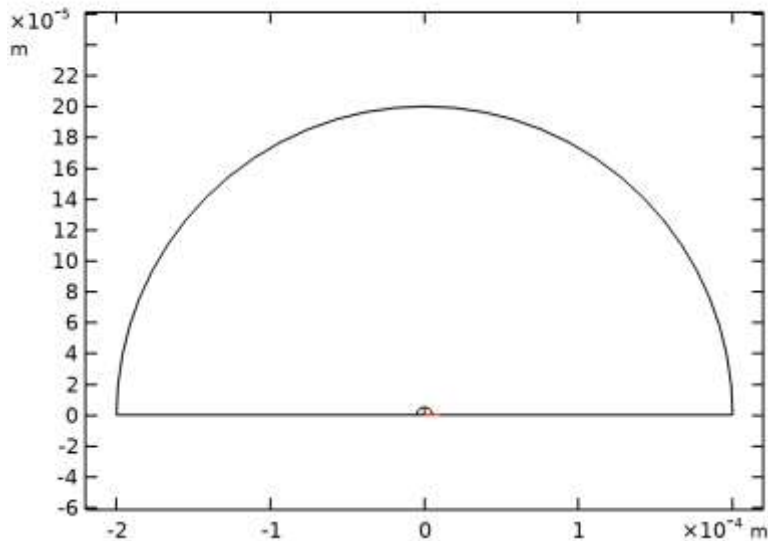
Description	Value
Dataset	Surface 1

LINE DATA

Description	Value
Line entry method	Two points
Points	{{0, 0}, {10e-6, 0}}

ADVANCED

Description	Value
Space variable	cln1x
Normal variables	{cln1nx, cln1ny}



Dataset: Cut Line 2D 1

4.1.8 Surface 3

DATA

Description	Value
Dataset	Study 1/Solution 1

PARAMETERIZATION

Description	Value
x- and y-axes	Surface parameters

4.2 TABLES

4.2.1 Evaluation 3D

Interactive 3D values

x	y	z	Value
-6.4146E-7	2.8626E-7	1.3553E-20	0.48692
-3.6979E-6	-3.3257E-6	1.3553E-20	1.4044
-4.2408E-5	-2.8827E-6	0.0000	-3.6692E-13
-1.0673E-6	-7.6865E-5	1.3553E-20	-1.1803E-12
-2.2825E-5	-1.1926E-4	1.3553E-20	-8.6631E-13
-3.7803E-5	-1.6642E-4	-2.7105E-20	-1.5890E-12
-2.2316E-5	4.3993E-6	1.3553E-20	-1.6752E-13
-1.2635E-8	-5.0517E-7	-1.3553E-20	6.5010E-4
1.0316E-8	-3.6520E-7	-1.3553E-20	6.3850E-4
-6.8195E-8	-2.1080E-7	2.7105E-20	6.2899E-4
-5.7855E-9	-1.9700E-7	-4.0658E-20	6.2595E-4
6.4279E-8	-1.6920E-7	-1.3553E-20	6.2398E-4
4.3102E-7	-2.4467E-7	5.1212E-7	-4.2017E-16
1.4098E-7	2.6498E-7	4.0658E-20	6.3042E-4
-7.4718E-6	3.9641E-6	1.3553E-20	-1.5472E-15
-4.2550E-6	-2.5837E-6	-2.7105E-20	7.3675E-4
-4.2377E-6	-2.5426E-6	-2.7105E-20	7.2396E-4
-4.1437E-6	-2.4854E-6	0.0000	6.9413E-4
-4.0051E-6	-2.3429E-6	-4.0658E-20	6.5459E-4
-3.6586E-6	-2.2655E-6	5.4210E-20	6.1257E-4
-3.4656E-6	-2.2203E-6	-5.4210E-20	5.9407E-4
-3.1907E-6	-2.2725E-6	-5.4210E-20	5.7832E-4
-2.7950E-6	-2.1792E-6	4.0658E-20	5.5036E-4
-2.4637E-6	-1.8053E-6	-2.7105E-20	5.2291E-4
-1.8567E-6	-1.9001E-6	-2.7105E-20	5.0692E-4
-1.2995E-6	-1.9668E-6	0.0000	4.9537E-4
1.1825E-7	-5.2582E-6	-5.4210E-20	-3.4587E-16
1.1318E-7	-5.1450E-6	2.7105E-20	-3.6183E-16
2.4001E-6	-6.1718E-6	0.0000	1.4878E-15
2.2734E-6	-5.6370E-6	0.0000	9.2856E-16
2.1179E-6	-5.0794E-6	0.0000	7.0144E-16
2.0079E-8	-1.6135E-7	0.0000	1.8842E-4
1.5361E-9	-2.7055E-7	0.0000	2.9246E-4

x	y	z	Value
-3.6315E-9	-4.6619E-7	5.4210E-20	4.3009E-4
8.2031E-8	-7.8916E-7	5.4210E-20	5.1596E-4
-6.1615E-9	-1.3079E-6	-1.0842E-19	5.4558E-4
-1.6446E-8	-1.6992E-6	-5.4210E-20	5.6109E-4
-3.5996E-8	-2.1450E-6	5.4210E-20	5.8555E-4
5.4274E-8	-2.4407E-6	5.4210E-20	6.0754E-4
6.2043E-8	-2.8911E-6	-5.4210E-20	6.4879E-4
1.4255E-7	-3.4097E-6	-5.4210E-20	7.2962E-4
5.9005E-8	-3.9010E-6	5.4210E-20	8.5581E-4
-1.8301E-9	-4.4243E-6	0.0000	0.0011202
-3.5323E-8	-4.9520E-6	0.0000	0.0021838
2.3403E-6	-4.7919E-6	5.4210E-20	5.3541E-16
2.5604E-6	-5.1279E-6	5.4210E-20	1.3368E-15
2.9795E-6	-5.7839E-6	2.7105E-20	4.4774E-15
3.8065E-6	-7.2805E-6	5.4210E-20	1.4578E-14
4.6164E-6	-8.4864E-6	2.7105E-20	2.5804E-14
5.1333E-6	-9.2448E-6	-5.4210E-20	3.3133E-14
5.6888E-6	-1.0171E-5	-5.4210E-20	3.0886E-14
6.2806E-6	-1.1153E-5	5.4210E-20	3.6776E-14
6.7556E-6	-1.1878E-5	1.0842E-19	4.6683E-14
7.3262E-6	-1.2843E-5	-5.4210E-20	4.6244E-14
-4.2737E-7	-4.0839E-7	1.3553E-20	4.1766E-4
1.1296E-6	-4.8281E-6	5.4210E-20	0.0022198
-4.5605E-6	-6.8667E-5	2.5000E-4	-1.7410E-12
-4.3637E-6	-6.9260E-5	2.5000E-4	-1.7593E-12
-4.1837E-6	-7.0305E-5	2.5000E-4	-1.7920E-12
-4.0387E-6	-7.1311E-5	2.5000E-4	-1.8236E-12
-3.9267E-6	-7.2221E-5	2.5000E-4	-1.8079E-12
-7.9394E-7	1.4484E-6	-1.0842E-19	5.5620E-4
4.0554E-6	2.4815E-7	0.0000	5.2129E-4
3.9466E-6	1.0710E-7	-1.0842E-19	2.3958E-4
3.9318E-6	1.9296E-8	0.0000	1.5687E-4
-3.6584E-6	-8.5383E-8	0.0000	5.3675E-4
3.9801E-6	2.1805E-8	1.0842E-19	1.3705E-4
-4.1967E-6	3.1670E-8	0.0000	5.8157E-4
-1.7041E-6	-7.0575E-6	2.7105E-20	1.1577E-14
1.0395E-6	-8.4181E-6	5.4210E-20	1.5162E-14
1.5990E-6	-1.0168E-5	-2.7105E-20	2.2999E-14
1.5200E-6	-8.7646E-6	2.7105E-20	1.6264E-14
1.2937E-6	-7.1984E-6	-8.1315E-20	1.0574E-14
8.4444E-7	-4.9464E-6	-1.3553E-20	8.4180E-17
8.3432E-7	-4.8206E-6	1.3553E-20	0.0018892
9.0914E-7	-5.5432E-6	-6.7763E-20	2.1592E-15
1.1480E-6	-6.6372E-6	-1.3553E-20	8.4244E-15
1.2855E-6	-7.5142E-6	-2.7105E-20	1.0596E-14

x	y	z	Value
1.5010E-6	-9.1540E-6	0.0000	1.7277E-14
2.0218E-6	-1.0842E-5	2.7105E-20	1.9606E-14
2.3860E-6	-1.2042E-5	-2.7105E-20	3.0892E-14
3.0292E-6	-4.6952E-8	5.4210E-20	1.2502E-4
-3.0734E-6	-5.8982E-8	2.7105E-20	3.9064E-4
2.3546E-6	-6.8232E-7	-1.0164E-20	0.21224
3.3862E-7	-5.0118E-7	-3.3881E-21	0.18471
-9.8742E-7	-6.4234E-7	-6.7763E-21	0.18862
-2.5290E-7	-8.9159E-7	1.3553E-20	0.18671
6.9264E-7	-1.1334E-6	-1.0164E-20	0.19031
2.0147E-6	-1.3501E-6	-1.0164E-20	0.21162
3.2299E-6	-1.5703E-6	-1.0164E-20	0.27106
3.9114E-6	-1.6420E-6	3.3881E-21	0.35531
4.0766E-6	-1.6242E-6	-3.3881E-21	0.38955
2.2309E-6	-3.7156E-6	3.3881E-21	0.37625
2.5701E-6	-3.9300E-6	1.6941E-20	0.50056
-7.0069E-8	-1.2213E-7	2.7105E-20	3.1037E-4
4.0581E-7	-1.3607E-7	-2.7105E-20	3.1821E-4
5.0892E-7	-1.4359E-7	-8.1315E-20	3.2417E-4
6.5485E-7	-1.3348E-7	0.0000	3.2122E-4
9.8480E-7	-1.5754E-7	5.4210E-20	3.3567E-4
1.2941E-6	-1.8009E-7	2.7105E-20	3.6651E-4
1.6019E-6	-2.2326E-7	0.0000	4.0928E-4
1.8921E-6	-2.2368E-7	0.0000	4.3446E-4
2.1918E-6	-1.0030E-7	-2.7105E-20	3.7828E-4
2.4218E-6	-7.5579E-8	2.7105E-20	3.7542E-4
2.1109E-6	-7.3665E-8	-2.7105E-20	3.5281E-4
1.8366E-6	-1.3663E-7	0.0000	3.7454E-4
1.5494E-6	-9.4962E-8	2.7105E-20	3.2619E-4
1.1767E-6	-8.8532E-8	2.7105E-20	3.1589E-4
9.0703E-7	-8.9635E-8	-8.1315E-20	3.0461E-4
2.5440E-6	-1.0524E-7	-5.4210E-20	4.2205E-4
2.7549E-6	-5.8359E-8	-8.1315E-20	3.9549E-4
2.9611E-6	-7.3404E-8	2.7105E-20	4.3969E-4
3.1261E-6	-8.5436E-8	-8.1315E-20	4.8245E-4
3.2926E-6	-7.6821E-8	-5.4210E-20	4.9434E-4
3.4782E-6	-9.0357E-8	0.0000	5.6174E-4
3.6447E-6	-8.1752E-8	0.0000	4.9907E-4
3.7875E-6	-1.1290E-7	-2.7105E-20	3.7979E-4
3.9730E-6	-1.2644E-7	-5.4210E-20	2.6679E-4
4.1412E-6	-9.7192E-8	-5.4210E-20	4.2908E-4
4.3092E-6	-6.7963E-8	2.7105E-20	7.8318E-4
4.4108E-6	-9.6114E-8	2.7105E-20	9.8540E-4
4.5963E-6	-1.0964E-7	0.0000	0.0012778
4.4314E-6	-9.7617E-8	2.7105E-20	0.0010218

x	y	z	Value
4.2252E-6	-8.2588E-8	0.0000	6.0555E-4
4.0365E-6	-1.1032E-7	2.7105E-20	2.7237E-4
4.1205E-6	-9.5684E-8	5.4210E-20	3.8451E-4
-3.8837E-6	-9.3074E-8	0.0000	6.1622E-4
-3.8631E-6	-9.4577E-8	-5.4210E-20	6.0595E-4
-4.0899E-6	-7.8037E-8	2.7105E-20	6.7351E-4
1.5123E-8	-1.5525E-7	0.0000	3.4276E-4
-1.1330E-7	-1.6347E-7	5.4210E-20	3.4109E-4
2.5181E-6	-7.8705E-8	-2.7105E-20	1.3554E-4
2.4736E-6	-8.7999E-8	0.0000	1.4158E-4
-1.9185E-6	-6.6611E-8	8.1315E-20	3.2259E-4
-2.3629E-6	-7.5743E-8	0.0000	3.4359E-4
-2.5410E-6	-1.1290E-7	8.1315E-20	3.8892E-4
-1.6037E-6	-4.7216E-6	2.7105E-20	0.0015847
-1.6037E-6	-4.7216E-6	2.7105E-20	0.0015847
-1.6035E-6	-4.7150E-6	0.0000	0.0017311
-1.6033E-6	-4.7072E-6	-8.1315E-20	0.0019041
-1.6032E-6	-4.6993E-6	-8.1315E-20	0.0020785
-1.6031E-6	-4.6902E-6	-8.1315E-20	0.0022771
-1.6039E-6	-4.6835E-6	5.4210E-20	0.0022423
3.4980E-6	-3.5641E-6	-5.4210E-20	0.0014193
3.4904E-6	-3.5524E-6	0.0000	0.0017364
3.4874E-6	-3.5448E-6	-2.7105E-20	0.0019106
3.4784E-6	-3.5301E-6	-1.0842E-19	0.0022783
4.8065E-6	-1.3855E-6	0.0000	0.0010214
4.8027E-6	-1.3859E-6	5.4210E-20	0.0015055
4.7926E-6	-1.4282E-6	5.4210E-20	0.0011696
4.7903E-6	-1.4280E-6	-8.1315E-20	0.0014688
4.7787E-6	-1.4274E-6	0.0000	0.0024805
4.7764E-6	-1.4286E-6	0.0000	0.0024613
4.7804E-6	-1.5138E-6	8.1315E-20	2.4282E-17
-4.9143E-6	-1.0744E-7	0.0000	0.0019882
4.9106E-6	-8.8864E-8	2.7105E-20	0.0019742
-4.7445E-7	5.2684E-6	-5.4210E-20	1.9340E-16
4.7794E-4	1.0842E-19	4.1249E-4	4.9920
4.9124E-4	0.0000	3.8897E-4	4.9917
3.3828E-4	-2.0278E-5	5.0000E-4	4.9914
4.0508E-4	-5.8088E-5	5.0000E-4	4.9922
4.9340E-4	-3.8451E-6	5.0000E-4	4.9925
4.9502E-4	-4.8131E-6	5.0000E-4	5.0000
1.0939E-5	-5.5512E-6	0.0000	0.073688
8.2032E-4	2.1684E-19	7.8307E-4	400.00
7.2304E-4	-2.1684E-19	8.4023E-4	400.00
4.6388E-4	2.1684E-19	5.4619E-4	400.00
2.5623E-4	2.1684E-19	1.6076E-4	400.00

x	y	z	Value
1.4824E-4	-5.4210E-19	7.7955E-6	399.84

4.2.2 Evaluation 2D

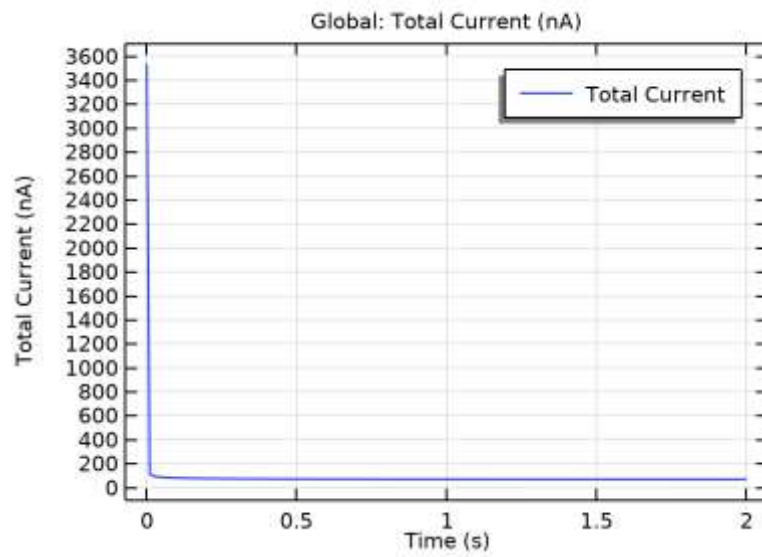
Interactive 2D values

x	y	Value
-4.9907E-6	-1.4470E-7	0.0021325
-4.7838E-6	-4.8858E-6	1.7758E-15
-5.0958E-7	-1.6073E-6	5.5961E-4
-4.5960E-6	2.1549E-6	2.4842E-16
-4.7892E-6	2.3481E-6	5.7527E-16
-4.7064E-6	2.1687E-6	2.9087E-16
-4.6857E-6	2.1687E-6	3.0611E-16
-4.6443E-6	2.1411E-6	3.0436E-16
-4.6443E-6	2.1411E-6	3.0436E-16
-8.6275E-6	-1.4951E-6	0.019949
-9.7059E-6	-1.3971E-6	0.022948
-1.1127E-5	-1.3971E-6	0.032134
-1.1814E-5	-1.3971E-6	0.046093
-1.2206E-5	-1.3971E-6	0.076433
-1.2353E-5	-1.3971E-6	0.11385
1.9563E-5	3.7593E-6	1.2314E-11
2.3002E-5	3.1860E-6	4.4218E-11
2.7015E-5	2.3261E-6	4.9274E-10
5.5105E-5	1.9136E-4	3.6869E-8
7.4749E-5	1.9332E-4	3.4555E-8
1.6491E-5	1.6672E-6	2.4341E-12
1.1277E-5	1.3116E-6	-2.4052E-14
-1.2845E-5	1.8630E-5	1.2781E-7
-2.3102E-5	1.8781E-6	7.7005E-8
6.5251E-6	2.1093E-6	1.6107E-8
9.2212E-6	3.5323E-6	-2.8640E-10
1.0195E-5	4.6556E-6	1.5373E-11
9.3710E-6	5.7041E-6	-1.7884E-12
5.3377E-7	6.4530E-6	7.9206E-13
1.1329E-6	9.6734E-6	-8.7623E-11
-7.7792E-6	1.9671E-5	-6.9156E-10
3.9039E-6	3.0606E-5	1.4913E-17
1.2078E-6	3.3601E-5	-2.3172E-17
-7.5049E-5	1.6351E-5	391.97
-8.1711E-5	2.0590E-5	394.42
-8.7162E-5	2.3619E-5	395.91
-8.8979E-5	2.3619E-5	396.22
-9.1402E-5	2.4224E-5	396.65
-4.2344E-5	8.9030E-5	397.46

x	y	Value
-4.2344E-5	1.0902E-4	398.92
-3.6893E-5	1.3748E-4	399.81
-3.8104E-5	1.5444E-4	399.94
-3.8104E-5	1.6534E-4	399.96
-3.8104E-5	1.7564E-4	399.97
-3.8710E-5	1.8533E-4	399.98
-4.5372E-5	2.0289E-4	400.00
5.2016E-8	2.0955E-4	399.99
5.2016E-8	2.2106E-4	400.00
5.5575E-6	2.0724E-6	-4.9147E-13
7.0750E-6	3.3731E-6	-6.3276E-12
9.8931E-6	4.6738E-6	-7.9741E-12
1.0543E-5	8.1422E-6	2.5189E-12
1.3795E-5	8.1422E-6	-9.7227E-14
1.0110E-5	1.4222E-6	2.4584E-14
-5.1228E-7	7.1442E-5	390.36
1.8723E-6	7.3176E-5	391.15
-5.2814E-6	1.1230E-4	398.78
-5.2814E-6	1.2098E-4	399.27
-2.2465E-6	1.2705E-4	399.50
-2.2465E-6	1.3051E-4	399.56
-6.5821E-6	2.3955E-4	400.00
-6.5821E-6	2.2048E-4	400.00
3.8233E-6	2.0140E-4	399.99
3.5483E-7	2.0400E-4	399.99
3.5483E-7	2.0834E-4	399.99
3.5483E-7	2.1267E-4	400.00

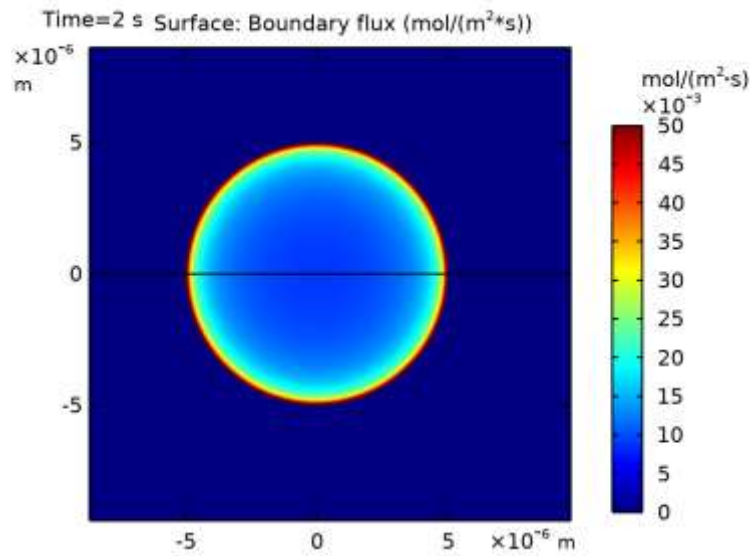
4.3 PLOT GROUPS

4.3.1 Average Current (tcd2)



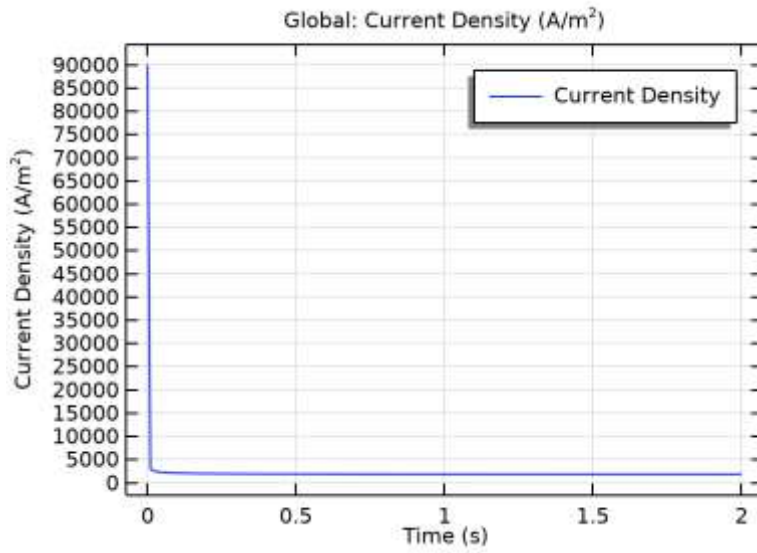
Global: Total Current (nA)

4.3.2 2D Normal Diffusive Flux Surface, Red, Surface (tcd2)



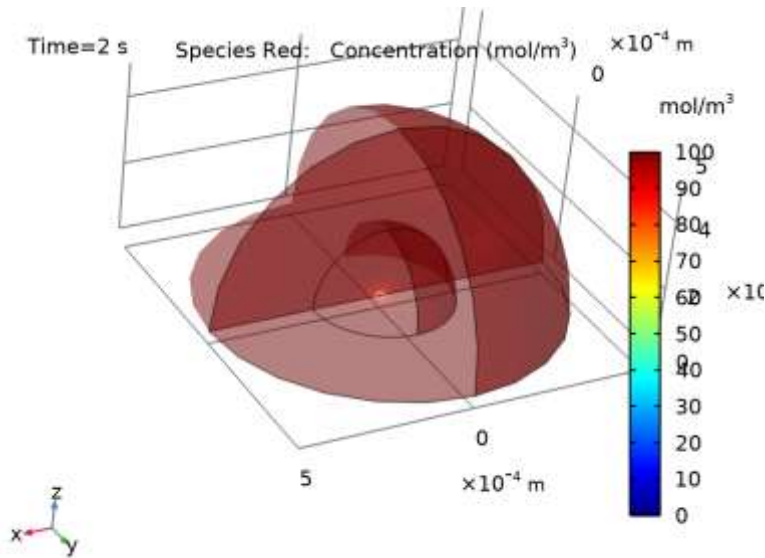
*Surface: Boundary flux (mol/(m²*s))*

4.3.3 Average Current Density (tcd2)



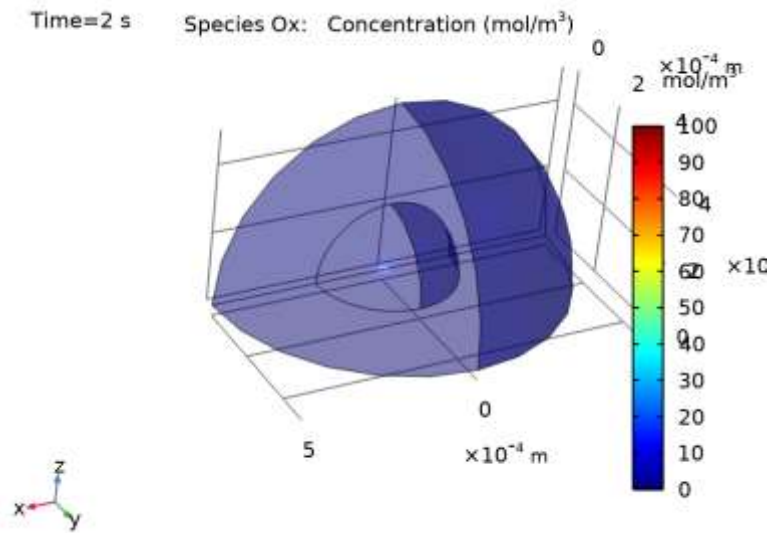
Global: Current Density (A/m²)

4.3.4 Concentration, Red, Surface (tcd2)



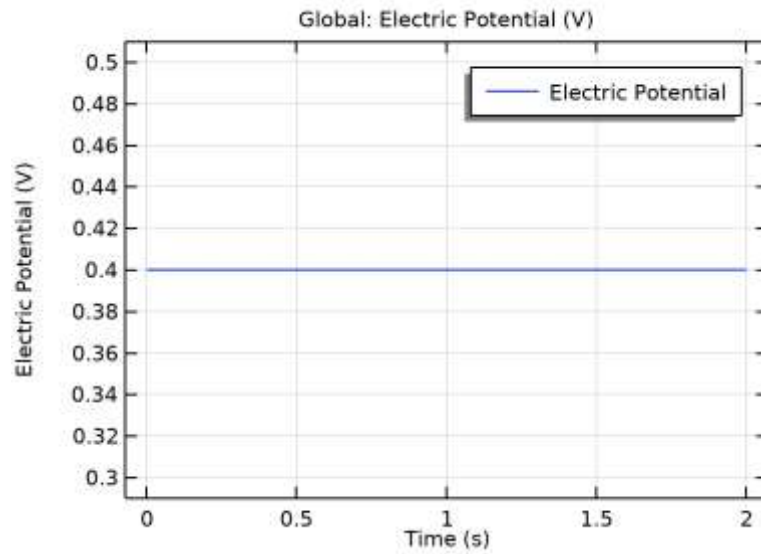
Species Red: Concentration (mol/m³)

4.3.5 Concentration, Ox, Surface (tcd2)



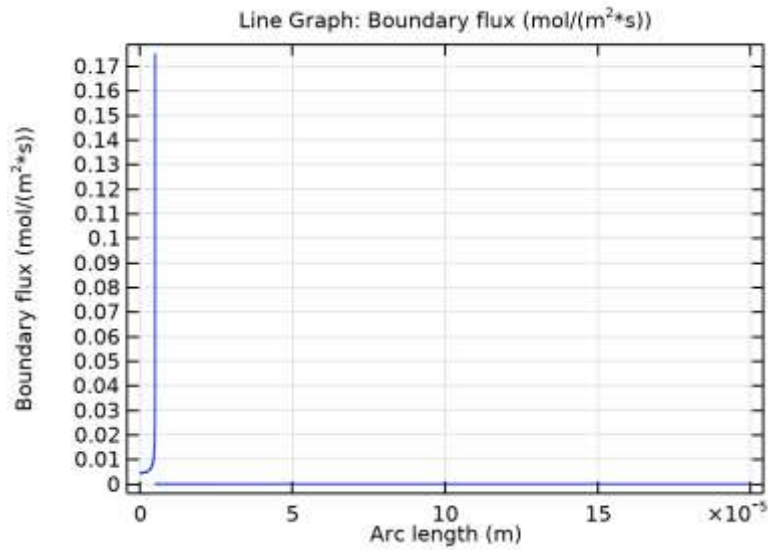
Species Ox: Concentration (mol/m³)

4.3.6 Electrode Potential (tcd2)



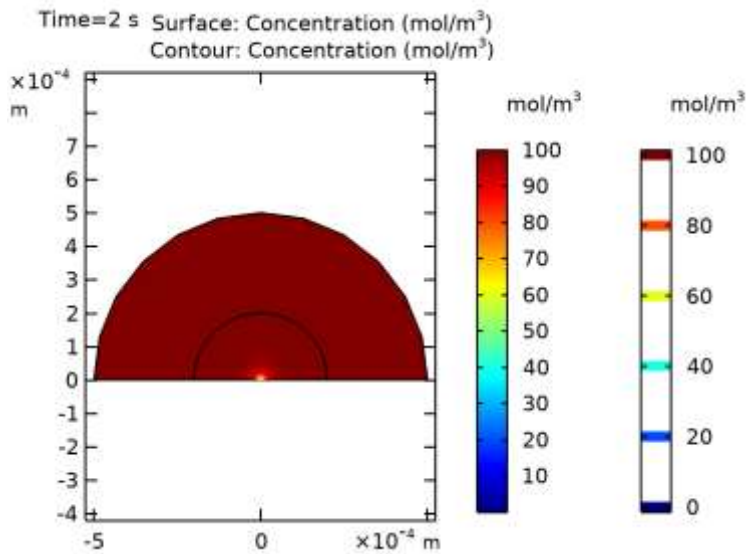
Global: Electric Potential (V)

4.3.7 Diffusive flux, Red, along electrode surface X direction



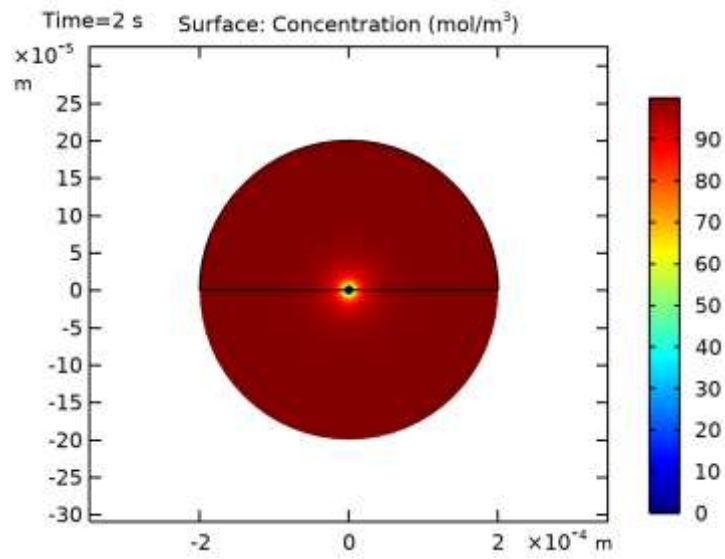
Line Graph: Boundary flux (mol/(m²*s))

4.3.8 Concentration, YZ plane



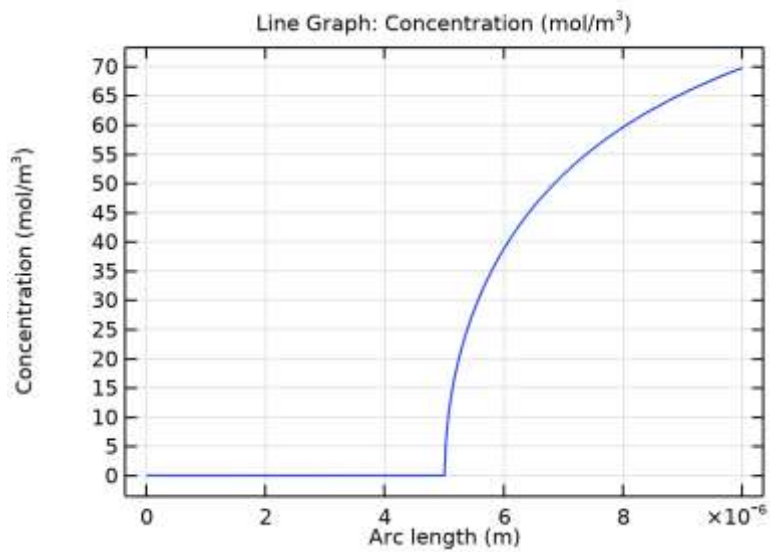
Surface: Concentration (mol/m³) Contour: Concentration (mol/m³)

4.3.9 Concentration



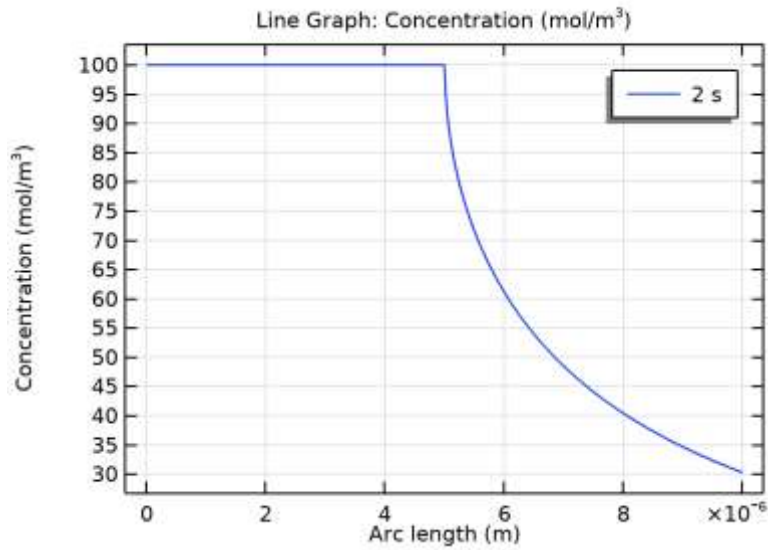
Surface: Concentration (mol/m³)

4.3.10 Concentration of redox (ferrocyanide) on electrode surface along X axis



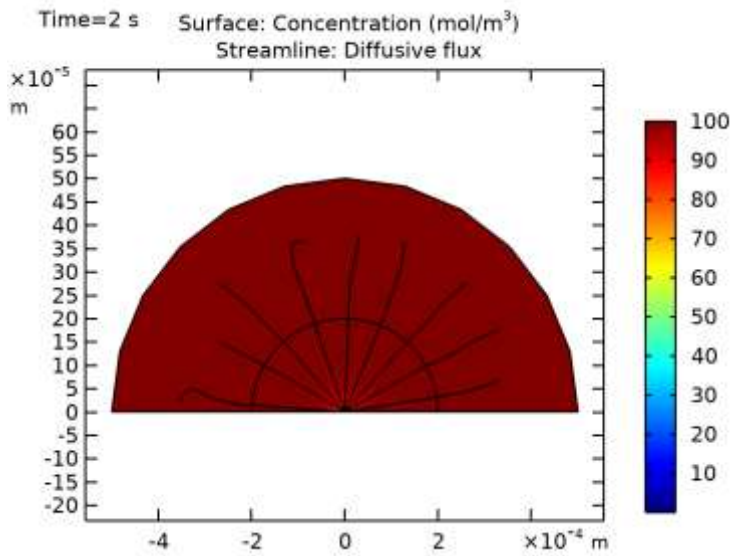
Line Graph: Concentration (mol/m³)

4.3.11 Concentration of redox (ferricyanide) on electrode surface along X axis 1



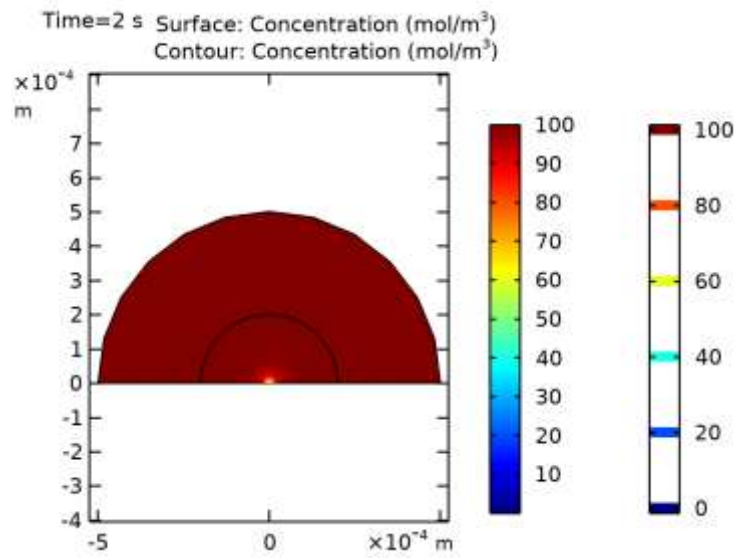
Line Graph: Concentration (mol/m³)

4.3.12 Concentration, Red, along XZ plane 1



Surface: Concentration (mol/m³) Streamline: Diffusive flux

4.3.13 Concentration, Red, along XZ plane contour plot



Surface: Concentration (mol/m³) Contour: Concentration (mol/m³)

References:

1. Faulkner, L. R.; Bard, A. J., *Electrochemical methods: fundamentals and applications*, 2e. John Wiley and Sons: **2002**.
2. Singh, P. S.; Lemay, S. G., *Stochastic Processes in Electrochemistry*. *Anal. Chem.* **2016**, 88 (10), 5017-5027.
3. Dix, J. A.; Verkman, A. S., *Crowding Effects on Diffusion in Solutions and Cells*. *Annu. Rev. Biophys.* **2008**, 37 (1), 247-263.
4. Ren, H.; Edwards, M. A., *Stochasticity in single-entity electrochemistry*. *Curr. Opin. Electrochem.* **2021**, 25, 100632.
5. Zhou, Y.-G.; Rees, N. V.; Compton, R. G., *Electrode–nanoparticle collisions: The measurement of the sticking coefficient of silver nanoparticles on a glassy carbon electrode*. *Chem. Phys. Lett.* **2011**, 514 (4-6), 291-293.
6. Rees, N. V.; Zhou, Y. G.; Compton, R. G., *The aggregation of silver nanoparticles in aqueous solution investigated via anodic particle coulometry*. *ChemPhysChem* **2011**, 12 (9), 1645-1647.
7. Zhou, Y. G.; Rees, N. V.; Compton, R. G., *The electrochemical detection and characterization of silver nanoparticles in aqueous solution*. *Angew. Chem. Int. Ed.* **2011**, 50 (18), 4219-4221.
8. Haddou, B.; Rees, N. V.; Compton, R. G., *Nanoparticle–electrode impacts: the oxidation of copper nanoparticles has slow kinetics*. *Phys. Chem. Chem. Phys.* **2012**, 14 (39), 13612-13617.
9. Zhou, Y.-G.; Haddou, B.; Rees, N. V.; Compton, R. G., *The charge transfer kinetics of the oxidation of silver and nickel nanoparticles via particle–electrode impact electrochemistry*. *Phys. Chem. Chem. Phys.* **2012**, 14 (41), 14354-14357.
10. Stuart, E. J.; Zhou, Y.-G.; Rees, N. V.; Compton, R. G., *Determining unknown concentrations of nanoparticles: the particle-impact electrochemistry of nickel and silver*. *RSC Adv.* **2012**, 2 (17), 6879-6884.
11. Ellison, J.; Tschulik, K.; Stuart, E. J.; Jurkschat, K.; Omanović, D.; Uhlemann, M.; Crossley, A.; Compton, R. G., *Get more out of your data: A new approach to agglomeration and aggregation studies using nanoparticle impact experiments*. *ChemistryOpen* **2013**, 2 (2), 69-75.
12. Cheng, W.; Zhou, X. F.; Compton, R. G., *Electrochemical sizing of organic nanoparticles*. *Angew. Chem. Int. Ed.* **2013**, 52 (49), 12980-12982.
13. Tschulik, K.; Haddou, B.; Omanović, D.; Rees, N. V.; Compton, R. G., *Coulometric sizing of nanoparticles: cathodic and anodic impact experiments open two independent routes to electrochemical sizing of Fe₃O₄ nanoparticles*. *Nano Res.* **2013**, 6 (11), 836-841.
14. Sun, T.; Yu, Y.; Zacher, B. J.; Mirkin, M. V., *Scanning electrochemical microscopy of individual catalytic nanoparticles*. *Angew. Chem. Int. Ed.* **2014**, 53 (51), 14120-14123.
15. Quinn, B. M.; van't Hof, P. G.; Lemay, S. G., *Time-Resolved Electrochemical Detection of Discrete Adsorption Events*. *J. Am. Chem. Soc.* **2004**, 126 (27), 8360-8361.
16. Boika, A.; Thorgaard, S. N.; Bard, A. J., *Monitoring the Electrophoretic Migration and Adsorption of Single Insulating Nanoparticles at Ultramicroelectrodes*. *J. Phys. Chem. B* **2013**, 117 (16), 4371-4380.
17. Fosdick, S. E.; Anderson, M. J.; Nettleton, E. G.; Crooks, R. M., *Correlated Electrochemical and Optical Tracking of Discrete Collision Events*. *J. Am. Chem. Soc.* **2013**, 135 (16), 5994-5997.
18. Park, J.-H.; Boika, A.; Park, H. S.; Lee, H. C.; Bard, A. J., *Single Collision Events of Conductive Nanoparticles Driven by Migration*. *J. Phys. Chem. C* **2013**, 117, 6651-6657.
19. Kim, B. K.; Boika, A.; Kim, J.; Dick, J. E.; Bard, A. J., *Characterizing Emulsions by Observation of Single Droplet Collisions - Attoliter Electrochemical Reactors*. *J. Am. Chem. Soc.* **2014**, 136, 4849-4852.
20. Lebegue, E.; Anderson, C. M.; Dick, J. E.; Webb, L. J.; Bard, A. J., *Electrochemical Detection of Single Phospholipid Vesicle Collisions at a Pt Ultramicroelectrode*. *Langmuir* **2015**, 31, 11734-11739.
21. Dick, J. E.; Hilterbrand, A. T.; Boika, A.; Upton, J. W.; Bard, A. J., *Electrochemical Detection of a Single Cytomegalovirus at an Ultramicroelectrode and its Antibody Anchoring*. *Proc. Natl. Acad. Sci. U.S.A.* **2015**, 112, 5303-5308.
22. Lee, J. Y.; Kim, B. K.; Kang, M.; Park, J.-H., *Label-Free Detection of Single Living Bacteria via Electrochemical Collision Event*. *Sci. Rep.* **2016**, 6, 30022.
23. Gao, G.; Wang, D.; Brocenschi, R.; Zhi, J.; Mirkin, M. V., *Toward the Detection and Identification of Single Bacteria by Electrochemical Collision Technique*. *Anal. Chem.* **2018**, 90, 12123-12130.
24. Ronspees, A. T.; Thorgaard, S. N., *Blocking Electrochemical Collisions of Single E. coli and B. subtilis bacteria at Ultramicroelectrodes Elucidated Using Simultaneous Fluorescence Microscopy*. *Electrochim. Acta* **2018**, 278, 412-420.

25. Ho, T. L. T.; Hoang, N. T. T.; Lee, J. Y.; Park, H. J.; Kim, B. K., Determining Mean Corpuscular Volume and Red Blood Cell Count Using Electrochemical Collision Events. *Biosens. Bioelectron.* **2018**, 110, 155-159.
26. Thorgaard, S. N.; Jenkins, S.; Tarach, A. R., Influence of Electroosmotic Flow on Stochastic Collisions at Ultramicroelectrodes. *Anal. Chem.* **2020**, 92, 12663-12669.
27. Renault, C.; Lemay, S. G., Electrochemical Collisions of Individual Graphene Oxide Sheets: An Analytical and Fundamental Study. *ChemElectroChem* **2020**, 7, 69-73.
28. Moazzenzade, T.; Yang, X.; Walterbos, L.; Huskens, J.; Renault, C.; Lemay, S. G., Self-Induced Convection at Microelectrodes via Electroosmosis and its Influence on Impact Electrochemistry. *J. Am. Chem. Soc.* **2020**, 142, 17908-17912.
29. Roehrich, B.; Liu, E. L.; Silverstein, R.; Sepunaru, L., Detection and Characterization of Single Particles by Electrochemical Impedance Spectroscopy. *J. Phys. Chem. Lett.* **2021**, 12, 9748-9753.
30. Pendergast, A. D.; Renault, C.; Dick, J. E., Correlated Optical -Electrochemical Measurements Reveal Bidirectional Current Steps for Graphene Nanoplatelet Collisions at Ultramicroelectrodes. *Anal. Chem.* **2021**, 93, 2898-2906.
31. Stevenson, K. J.; Tschulik, K., A materials driven approach for understanding single entity nano impact electrochemistry. *Curr. Opin. Electrochem.* **2017**, 6 (1), 38-45.
32. Xiao, X.; Fan, F.-R. F.; Zhou, J.; Bard, A. J., Current transients in single nanoparticle collision events. *J. Am. Chem. Soc.* **2008**, 130 (49), 16669-16677.
33. Zhou, H.; Fan, F.-R. F.; Bard, A. J., Observation of discrete Au nanoparticle collisions by electrocatalytic amplification using Pt ultramicroelectrode surface modification. *J. Phys. Chem. Lett.* **2010**, 1 (18), 2671-2674.
34. Kwon, S. J.; Fan, F.-R. F.; Bard, A. J., Observing iridium oxide (IrO_x) single nanoparticle collisions at ultramicroelectrodes. *J. Am. Chem. Soc.* **2010**, 132 (38), 13165-13167.
35. Stuart, E. J. E.; Zhou, Y.-G.; Rees, N. V.; Compton, R. G., Determining unknown concentrations of nanoparticles: the particle-impact electrochemistry of nickel and silver. *RSC Adv.* **2012**, 2 (17), 6879-6884.
36. Lees, J. C.; Ellison, J.; Batchelor-McAuley, C.; Tschulik, K.; Damm, C.; Omanović, D.; Compton, R. G., Nanoparticle Impacts Show High-Ionic-Strength Citrate Avoids Aggregation of Silver Nanoparticles. *ChemPhysChem* **2013**, 14 (17), 3895-3897.
37. Stuart, E. J.; Tschulik, K.; Batchelor-McAuley, C.; Compton, R. G., Electrochemical observation of single collision events: Fullerene nanoparticles. *ACS Nano* **2014**, 8 (8), 7648-7654.
38. Guo, Z.; Percival, S. J.; Zhang, B., Chemically resolved transient collision events of single electrocatalytic nanoparticles. *J. Am. Chem. Soc.* **2014**, 136 (25), 8879-8882.
39. Jung, A. R.; Lee, S.; Joo, J. W.; Shin, C.; Bae, H.; Moon, S. G.; Kwon, S. J., Potential-controlled current responses from staircase to blip in single Pt nanoparticle collisions on a Ni ultramicroelectrode. *J. Am. Chem. Soc.* **2015**, 137 (5), 1762-1765.
40. Anderson, T. J.; Zhang, B., Single-nanoparticle electrochemistry through immobilization and collision. *Acc. Chem. Res.* **2016**, 49 (11), 2625-2631.
41. Dick, J. E.; Bard, A. J., Toward the digital electrochemical recognition of cobalt, iridium, nickel, and iron ion collisions by catalytic amplification. *J. Am. Chem. Soc.* **2016**, 138 (27), 8446-8452.
42. Kwon, S. J.; Zhou, H.; Fan, F.-R. F.; Vorobyev, V.; Zhang, B.; Bard, A. J., Stochastic electrochemistry with electrocatalytic nanoparticles at inert ultramicroelectrodes—theory and experiments. *Phys. Chem. Chem. Phys.* **2011**, 13 (12), 5394-5402.
43. Robinson, D. A.; Liu, Y.; Edwards, M. A.; Vitti, N. J.; Oja, S. M.; Zhang, B.; White, H. S., Collision dynamics during the electrooxidation of individual silver nanoparticles. *J. Am. Chem. Soc.* **2017**, 139 (46), 16923-16931.
44. Robinson, D. A.; Edwards, M. A.; Ren, H.; White, H. S., Effects of Instrumental Filters on Electrochemical Measurement of Single-Nanoparticle Collision Dynamics. *ChemElectroChem* **2018**, 5 (20), 3059-3067.
45. Baker, L. A., Perspective and Prospectus on Single-Entity Electrochemistry. *J. Am. Chem. Soc.* **2018**, 140 (46), 15549-15559.
46. Kim, B.-K.; Boika, A.; Kim, J.; Dick, J. E.; Bard, A. J., Characterizing Emulsions by Observation of Single Droplet Collisions-Attoliter Electrochemical Reactors. *J. Am. Chem. Soc.* **2014**, 136 (13), 4849-4852.
47. Dick, J. E.; Renault, C.; Kim, B.-K.; Bard, A. J., Electrogenerated chemiluminescence of common organic luminophores in water using an emulsion system. *J. Am. Chem. Soc.* **2014**, 136 (39), 13546-13549.
48. Dick, J. E.; Renault, C.; Kim, B. K.; Bard, A. J., Simultaneous detection of single attoliter droplet collisions by electrochemical and electrogenerated chemiluminescent responses. *Angew. Chem. Int. Ed.* **2014**, 53 (44), 11859-11862.
49. K.; Kim, J.; Bard, A. J., Electrochemistry of a single attoliter emulsion droplet in collisions. *J. Am. Chem. Soc.* **2015**, 137 (6), 2343-2349.

50. Li, Y.; Deng, H.; Dick, J. E.; Bard, A. J., Analyzing benzene and cyclohexane emulsion droplet collisions on ultramicroelectrodes. *Anal. Chem.* **2015**, 87 (21), 11013-11021.
51. Dick, J. E.; Lebègue, E.; Strawsine, L. M.; Bard, A. J., Millisecond Coulometry via Zeptoliter Droplet Collisions on an Ultramicroelectrode. *Electroanal.* **2016**, 28 (10), 2320-2326.
52. Cheng, W.; Compton, R. G., Quantifying the Electrocatalytic Turnover of Vitamin B12-Mediated Dehalogenation on Single Soft Nanoparticles. *Angew. Chem. Int. Ed.* **2016**, 55 (7), 2545-2549.
53. Park, S.; Kim, H.; Chae, J.; Chang, J., Electrochemical generation of single emulsion droplets and in situ observation of collisions on an ultramicroelectrode. *J. Phys. Chem. C* **2016**, 120 (7), 3922-3928.
54. Deng, H.; Dick, J. E.; Kummer, S.; Kragl, U.; Strauss, S. H.; Bard, A. J., Probing Ion Transfer across Liquid-Liquid Interfaces by Monitoring Collisions of Single Femtoliter Oil Droplets on Ultramicroelectrodes. *Anal. Chem.* **2016**, 88 (15), 7754-7761.
55. Hoang, N. T.; Ho, T. L.; Park, J. H.; Kim, B.-K., Detection and study of single water/oil nanoemulsion droplet by electrochemical collisions on an ultramicroelectrode. *Electrochim. Acta* **2017**, 245, 128-132.
56. Lee, J.; Ho, T. L.; Kim, H. Y.; Park, J. H.; Kim, B. K., Direct electrolysis and detection of single nanosized water emulsion droplets in organic solvent using stochastic collisions. *Electroanal.* **2019**, 31 (1), 167-171.
57. Chang, L.; Bard, A. J., Electrochemical Characterization of Bromine Reduction to Tribromide in Individual Nitrobenzene-in-Water Emulsion Droplets. *J. Electrochem. Soc.* **2020**, 167 (6), 066505.
58. Lebègue, E.; Anderson, C. M.; Dick, J. E.; Webb, L. J.; Bard, A. J., Electrochemical detection of single phospholipid vesicle collisions at a Pt ultramicroelectrode. *Langmuir* **2015**, 31 (42), 11734-11739.
59. Sepunaru, L.; Sokolov, S. V.; Holter, J.; Young, N. P.; Compton, R. G., Electrochemical red blood cell counting: one at a time. *Angew. Chem. Int. Ed.* **2016**, 55 (33), 9768-9771.
60. Ho, T. L.; Hoang, N. T.; Lee, J.; Park, J. H.; Kim, B.-K., Determining mean corpuscular volume and red blood cell count using electrochemical collision events. *Biosens. Bioelectron.* **2018**, 110, 155-159.
61. Lee, J. Y.; Kim, B.-K.; Kang, M.; Park, J. H., Label-free detection of single living bacteria via electrochemical collision event. *Sci. Rep.* **2016**, 6 (1), 1-6.
62. Ronspees, A. T.; Thorgaard, S. N., Blocking electrochemical collisions of single E. coli and B. subtilis bacteria at ultramicroelectrodes elucidated using simultaneous fluorescence microscopy. *Electrochim. Acta* **2018**, 278, 412-420.
63. Gao, G.; Wang, D.; Brocenschi, R.; Zhi, J.; Mirkin, M. V., Toward the detection and identification of single bacteria by electrochemical collision technique. *Anal. Chem.* **2018**, 90 (20), 12123-12130.
64. Goines, S.; Dick, J. E., Electrochemistry's Potential to Reach the Ultimate Sensitivity in Measurement Science. *J. Electrochem. Soc.* **2019**, 167 (3), 037505.
65. Renault, C.; Lemay, S. G., Electrochemical collisions of individual graphene oxide sheets: an analytical and fundamental study. *ChemElectroChem* **2020**, 7 (1), 69-73.
66. Xiao, X.; Bard, A. J., Observing single nanoparticle collisions at an ultramicroelectrode by electrocatalytic amplification. *J. Am. Chem. Soc.* **2007**, 129 (31), 9610-9612.
67. Luo, L.; White, H. S., Electrogeneration of Single Nanobubbles at Sub-50-nm-Radius Platinum Nanodisk Electrodes. *Langmuir* **2013**, 29 (35), 11169-11175.
68. Dickinson, E. J. F.; Rees, N. V.; Compton, R. G., Nanoparticle-electrode collision studies: Brownian motion and the timescale of nanoparticle oxidation. *Chem. Phys. Lett.* **2012**, 528, 44-48.
69. Ustarroz, J.; Kang, M.; Bullions, E.; Unwin, P. R., Impact and oxidation of single silver nanoparticles at electrode surfaces: one shot versus multiple events. *Chem. Sci.* **2017**, 8 (3), 1841-1853.
70. Robinson, D. A.; Edwards, M. A.; Liu, Y.; Ren, H.; White, H. S., Effect of viscosity on the collision dynamics and oxidation of individual Ag nanoparticles. *J. Phys. Chem. C* **2020**, 124 (16), 9068-9076.
71. Oja, S. M.; Robinson, D. A.; Vitti, N. J.; Edwards, M. A.; Liu, Y.; White, H. S.; Zhang, B., Observation of multiple collision behavior during the electro-oxidation of single Ag nanoparticles. *J. Am. Chem. Soc.* **2017**, 139 (2), 708-718.
72. Ma, H.; Zhong, C. B.; Ying, Y.-L.; Long, Y.-T., Seeing Is Not Believing: Filtering Effects on Random Nature in Electrochemical Measurements of Single-Entity Collision. *ACS Meas. Sci. Au* **2022**.
73. Bonezzi, J.; Boika, A., Deciphering the magnitude of current steps in electrochemical blocking collision experiments and its implications. *Electrochim. Acta* **2017**, 236, 252-259.
74. Lee, J. Y.; Kim, B.-K.; Kang, M.; Park, J. H., Label-free detection of single living bacteria via electrochemical collision event. *Sci. Rep.* **2016**, 6, 30022.
75. Tirado, M. M.; de la Torre, J. G., Translational friction coefficients of rigid, symmetric top Macromolecules. Application to Circular Cylinders. *J. Chem. Phys.* **1979**, 71, 2581-2587.

76. Tirado, M. M.; de la Torre, J. G., Rotational Dynamics of Rigid, Symmetric Top macromolecules. application to Circular Cylinders. *J. Chem. Phys.* **1980**, 73, 1986-1993.
77. Nixon-Luke, R.; Bryant, G., A depolarized dynamic light scattering method to calculate translational and rotational diffusion coefficients of nanorods. *Part. Part. Syst. Charact.* **2019**, 36, 1800388.
78. Ahmed, J. U.; Lutkenhaus, J. A.; Alam, M. S.; Marshall, I.; Paul, D. K.; Alvarez, J. C., Dynamics of Collisions and Adsorption in the Stochastic Electrochemistry of Emulsion Microdroplets. *Anal. Chem.* **2021**, 93 (22), 7993-8001.
79. Robinson, D. A.; Liu, Y.; Edwards, M. A.; Vitti, N. J.; Oja, S. M.; Zhang, B.; White, H. S., Collision dynamics during the electrooxidation of individual silver nanoparticles. *J. Am. Chem. Soc.* **2017**, 139, 16923-16931.
80. White, R. J.; White, H. S., A random walk through electron-transfer kinetics. *Anal. Chem.* **2005**, 77, 214A-220A.
81. Dick, J. E., Electrochemical detection of single cancer and healthy cell collisions on a microelectrode. *Chem. Commun.* **2016**, 52, 10906-10909.
82. Sepunaru, L.; Sokolov, S. V.; Holter, J.; Young, N. P.; Compton, R. G., Electrochemical red blood cell counting: one at a time. *Angew. Chem. Int. Ed.* **2016**, 55, 9768-9771.
83. Svetlicic, V.; Ivosevic, N.; Kovac, S.; Zutic, V., Charge displacement by adhesion and spreading of a cell. *Bioelectrochemistry* **2000**, 53, 79-86.
84. Rees, N. V.; Banks, C. E.; Compton, R. G., Ultrafast chronoamperometry of acoustically agitated solid particulate suspensions: nonfaradaic and faradaic processes at a polycrystalline gold electrode. *J. Phys. Chem. B* **2004**, 108, 18391-18394.
85. Scholz, F.; Hellberg, D.; Harnisch, F.; Hummel, A.; Hasse, U., Detection of the adhesion events of dispersed single montmorillonite particles at a static mercury drop electrode. *Electrochem. Commun.* **2004**, 6, 929-933.
86. Huang, K.-C.; White, R. J., Random walk on a leash: a simple single-molecule diffusion model for surface-tethered redox molecules with flexible linkers. *J. Am. Chem. Soc.* **2013**, 135, 12808-12817.
87. Einstein, A., Uber die von der molekularkinetischen Theorie der Wärme geforderte Bewegung von in ruhenden Flüssigkeiten suspendierten Teilchen. *Ann. Phys.* **1905**, 322, 549-560.
88. White, R. J.; White, H. S., Electrochemistry in nanometer-wide electrochemical cells. *Langmuir* **2008**, 24, 2850-2855.
89. Kwon, S. J.; Zhou, H.; Fan, F.-R. F.; Vorobyev, V.; Zhang, B.; Bard, A. J., Stochastic electrochemistry with electrocatalytic nanoparticles at inert ultramicroelectrodes—theory and experiments. *Phys. Chem. Chem. Phys.* **2011**, 13, 5394-5402.
90. Dickinson, E. J. F.; Rees, N. V.; Compton, R. G., Nanoparticle-electrode collision studies: Brownian motion and the timescale of nanoparticle oxidation. *Chem. Phys. Lett.* **2012**, 528, 44-48.
91. Ma, W.; Ma, H.; Chen, J.-F.; Peng, Y.-Y.; Ynag, Z.-Y.; Wang, H.-F.; Ying, Y.-L.; Tian, H.; Long, Y.-T., Tracking motion trajectories of individual nanoparticles using time-resolved current traces. *Chem. Sci.* **2017**, 8, 1854-1861.
92. Andersen, O. S.; Feldberg, S. W., The Heterogeneous Collision Velocity for Hydrate Ions in Aqueous Solutions is ~104 cm/s. *J. Phys. Chem.* **1996**, 1996, 4622-4629.
93. Hupp, J. T.; Weaver, M. J., The frequency factor for outer-sphere electrochemical reactions. *J. Electroanal. Chem.* **1983**, 152, 1-14.
94. Robinson, D. A.; Yoo, J. J.; Castaneda, A. D.; Gu, B.; Dasari, R.; Crooks, R. M.; Stevenson, K. J., Increasing the collision rate of particle impact electroanalysis with magnetically guided Pt-decorated iron oxide nanoparticles. *ACS Nano* **2015**, 9, 7583-7595.
95. Paul, D. K.; Meng, K.; Omanovic, D.; Alvarez, J. C., Hydrogen Bonding and Proton Transfer in Aqueous Toluene Microdroplets Studied by Particle Collision Electrochemistry. *ChemElectroChem* **2018**, 5, 2528-2533.
96. Li, Y.; Deng, H.; Dick, J. E.; Bard, A. J., Analyzing benzene and cyclohexane emulsion droplet collisions on ultramicroelectrodes. *Anal. Chem.* **2015**, 87, 11013-11021.
97. Kim, B. K.; Kim, J.; Bard, A. J., Electrochemistry of a single attoliter emulsion droplet in collisions. *J. Am. Chem. Soc.* **2015**, 137, 2343-2349.
98. Deng, H.; Dick, J. E.; Kummer, S.; Kragl, U.; Strauss, S. H.; Bard, A. J., Probing ion transfer across liquid-liquid interfaces by monitoring collisions of single femtoliter oil droplets on ultramicroelectrodes. *Anal. Chem.* **2016**, 88, 7754-7761.
99. Robinson, D. A.; Edwards, M. A.; Ren, H.; White, H. S., Effects of Instrumental Filters on Electrochemical Measurement of Single-Nanoparticle Collision Dynamics. *ChemElectroChem* **2018**, 5, 3059-3067.
100. Yang, H.-J.; Kwon, H.; Kim, B. K.; Park, J. H., Electrochemical detection of single attoliter aqueous droplets in electrolyte-free organic solvent via collision events. *Electrochim. Acta* **2019**, 320, 134620-134626.
101. Weatherly, C. K. T.; Glasscott, M. W.; Dick, J. E., Voltammetric analysis of redox reactions and ion transfer in water microdroplets. *Langmuir* **2020**, 36, 8231-8239.

102. Zhang, H.; Sepunaru, L.; Sokolov, S. V.; Laborda, E.; McAuley, C. B.; Compton, R. G., Electrochemistry of single droplets of inverse (water-in-oil) emulsions. *Phys. Chem. Chem. Phys.* **2017**, *19*, 15662-15666.
103. Trojaneck, A.; Samec, Z., Study of the emulsion droplet collisions with the polarizable water/1, 2-dichloroethane interface by the open circuit potential measurements. *Electrochim. Acta* **2019**, *299*, 875-885.
104. Hoang, N. T. T.; Ho, T. L. T.; Park, J. H.; Kim, B. K., Detection and study of single water/oil nanoemulsion droplet by electrochemical collisions on an ultramicroelectrode. *Electrochim. Acta* **2017**, *245*, 128-132.
105. Danis, L.; Polcari, D.; Kwan, A.; Gateman, S. M.; Mauzeroll, J., Fabrication of carbon, gold, platinum, silver, and mercury ultramicroelectrodes with controlled geometry. *Anal. Chem.* **2015**, *87*, 2565-2569.
106. Quinn, B. M.; van't Hof, P. G.; Lemay, S. G., Time-resolved electrochemical detection of discrete adsorption events. *J. Am. Chem. Soc.* **2004**, *126*, 8360-8361.
107. Boika, A.; Thorgaard, S. N.; Bard, A. J., Monitoring the electrophoretic migration and adsorption of single insulating nanoparticles at ultramicroelectrodes. *J. Phys. Chem. B* **2013**, *117*, 4371-4380.
108. Fodsick, S. E.; Anderson, M. J.; Nettleton, E. G.; Crooks, R. M., Correlated electrochemical and optical tracking of discrete collision events. *J. Am. Chem. Soc.* **2013**, *135*, 5994-5997.
109. Kanokkanchana, K.; Saw, E. N.; Tschulik, K., Nano impact electrochemistry: effects of electronic filtering on peak height, duration and area. *ChemElectroChem* **2018**, *5*, 3000-3005.
110. Bretschneider, F.; Weille, J. D., Introduction to Electrophysiological Methods and Instrumentation. 2nd ed.; Academic Press: London, UK, **2019**; p 355.
111. Bond, A. M.; Henderson, T. L. E.; Mann, D. R.; Mann, T. F.; Thormann, W.; Zoski, C. G., A fast electron transfer rate for the oxidation of ferrocene in acetonitrile or dichloromethane at platinum disk ultramicroelectrodes. *Anal. Chem.* **1988**, *60*, 1878-1882.
112. Mirkin, M. V.; Richards, T. C.; Bard, A. J., Scanning electrochemical microscopy. 20. Steady-state measurements of the fast heterogeneous kinetics in the ferrocene/acetonitrile system. *J. Phys. Chem.* **1993**, *97*, 7672-7677.
113. Goines, S.; Dick, J. E., Electrochemistry's Potential to Reach the Ultimate Sensitivity in Measurement Science. *J. Electrochem. Soc.* **2020**, *167*, 037505.
114. Moazzenzade, T.; Huskens, J.; Lemay, S. G., Stochastic electrochemistry at ultralow concentrations: the case for digital sensors. *Analyst* **2020**, *145*, 750-758.
115. Deng, Z.; Renault, C., Detection of individual insulating entities by electrochemical blocking. *Curr. Opin. Electrochem.* **2021**, *25*, 100619.
116. Bonezzi, J.; Boika, A., Deciphering the magnitude of current steps in electrochemical blocking collision experiments and its implications. *Electrochim. Acta* **2017**, *236*, 252-259.
117. Dick, J. E.; Renault, C.; Bard, A. J., Observation of single-protein and DNA macromolecule collisions on ultramicroelectrodes. *J. Am. Chem. Soc.* **2015**, *137*, 8376-8379.
118. Suraniti, E.; Kanoufi, F.; Gosse, C.; Zhao, X.; Dimova, R.; Pouligny, B.; Sojic, N., Electrochemical detection of single microbeads manipulated by optical tweezers in the vicinity of ultramicroelectrodes. *Anal. Chem.* **2013**, *85*, 8902-8909.
119. Chung, J. H.; Jiseon, J. L.; Hwang, J.; Seol, K. H.; Kim, K. M.; Song, J.; Chang, J., Stochastic Particle Approach Electrochemistry (SPAEC): Estimating Size, Drift Velocity, and Electric Force of Insulating Particles. *Anal. Chem.* **2020**, *92*, 12226-12234.
120. Zhao, H.; Chang, J.; Boika, A.; Bard, A. J., Electrochemistry of high concentration copper chloride complexes. *Anal. Chem.* **2013**, *85*, 7696-7703.
121. Konopka, S. J.; McDuffie, B., Diffusion coefficients of ferri- and ferrocyanide ions in aqueous media, using twin-electrode thin-layer electrochemistry. *Anal. Chem.* **1970**, *42*, 1741-1746.
122. Westfall, C. S.; Levin, P. A., Bacterial cell size: multifactorial and multifaceted. *Annu. Rev. Microbiol.* **2017**, *71*, 499-517.
123. Athale, C. A.; Chaudhari, H., Population length variability and nucleoid numbers in Escherichia coli. *Bioinformatics* **2011**, *27*, 2944-2948.
124. Miller, E. S.; Woese, C. R., Description of the Erythromycin-Producing Bacterium *Arthrobacter* sp. Strain NRRL B-3381 as *Aeromicrobium erythreum* gen. nov., sp. nov. *Int. J. Syst. Evol. Microbiol.* **1991**, *41*, 363-368.
125. Wakita, J.; Kininaka, H.; Matsuyama, T.; Matsushita, M., Size Distribution of Bacterial Cells in Homogeneously Spreading Disk-like Colonies by *Bacillus subtilis*. *J. Phys. Soc. Jpn.* **2010**, *79*, 094002.
126. Albertini, A.; T., C.; Crabb, W.; Scoffone, F.; Galizzi, A., The *flaA* locus of *Bacillus subtilis* is part of a large operon coding for flagellar structures, motility functions, and an ATPase-like polypeptide. *J. Bacteriol.* **1991**, *173*, 3573-3579.
127. Larsen, S. H.; Reader, R. W.; Kort, E. N.; Tso, W. W.; Adler, J., Change in direction of flagellar rotation is the basis of the chemotactic response in *Escherichia coli*. *Nature* **1974**, *249* (74-77).

128. Ma, H.; Chen, J.-F.; Wang, H.-F.; Hu, P.-J.; Ma, W.; Long, Y.-T., Exploring dynamic interactions of single nanoparticles at interfaces for surface-confined electrochemical behavior and size measurement. *Nat. Commun.* **2020**, 11 (1), 2307.
129. Liu, R.; Wang, D., Pressure-Regulated Single-Entity Electrochemistry Inside Carbon Nanopipettes. *ACS Sens.* **2022**, 7 (4), 1138-1144.
130. Defnet, P. A.; Zhang, B., Collision, Adhesion, and Oxidation of Single Ag Nanoparticles on a Polysulfide-Modified Microelectrode. *J. Am. Chem. Soc.* **2021**, 143 (39), 16154-16162.